Multi-hazard and risk informed system for Enhanced local and regional Disaster risk management

MEDiate

Deliverable D2.2

A diagnosis and assessment of the primary types of interacting hazards related to European areas

Author(s):	Esther Hlíðar Jensen, Mohammed Sarfaraz Gani Adnan, Eleonora Perugini, Marcello Arosio, Talfan Barnie, Frederiek Sperna Weiland, Mario Martinelli, Matthew J. Roberts, Christopher J. White, Natalia Castillo, Marco Gaetani, Martina Stefani, and Tinna Þórarinsdóttir
Responsible Partner:	Icelandic Meteorological Office
Version:	3.0 [Final]
Date:	26/03/2024
Distribution level:	Public

DOCUMENT REVISION HISTORY

Date	Version	Editors	Comments
21/07/2023	1.1	EHJ, MSGA, JD, MJR, CW, TÞ	First draft
08/02/2024	1.2	EHJ, MSGA, EP, TB, MJR, CW, TÞ	Second draft
25/02/2024	1.3	EHJ, MSGA, EP, TB, MJR, CW, TÞ	Third draft
29/02/2024	2.0	EHJ, MSGA, EP, TB, MJR, CW, TÞ	Final draft for review
21/03/2024	3.0	EHJ, MSGA, EP, TB, MJR, CW, TÞ	Final, post-review version
16/04/2024	3.1	EHJ, MSGA, EP, TB, MJR, CW, TÞ	Final, post-review revised version

LIST OF PARTNERS

Participant	Name	Country
NOR	NORSAR	Norway
DEL	Deltares	Netherlands
IIASA	International Institute for Applied Systems Analysis	Austria
BRGM	Bureau de Recherches Géologiques et Minières	France
EUC	Fondazione Eucentre	Italy
IMO	Icelandic Meteorological Office	Iceland
IMT	Institut Mines-Telecom	France
UIce	University of Iceland	Iceland
R2M	R2M Solution	France
RINA-C	RINA Consulting	Italy
IUSS	Istituto Universitario di Studi Superiore Pavia	Italy
OSL	Oslo kommune	Norway
NICE	Metropole Nice Cote d'Azur	France
AUS	Austurbru	Iceland
UStr	University of Strathclyde	UK
UCL	University College London	UK
ARU	Anglia Ruskin University	UK
ECC	Essex County Council	UK

CONTENTS

LIST OF FIGURES

LIST OF TABLES

1 INTRODUCTION

The MEDiate project aims to develop a decision-support system (DSS) for disaster-risk management that provides local authorities, businesses, and citizens with a comprehensive web-based platform to assess the risks posed by natural hazards. Within the project, Work Package 2 (WP2) is designed for the *Assessment of current and future multi-hazard interactions and cascading impacts*. It diagnoses the primary forms of interacting natural hazards across Europe, drawing examples from four specific testbed locations.

Within WP2, the focus of this report, designated as deliverable 2.2 (D2.2), lies in analysing interactions between hydrological, meteorological, and climatological hazards, including mass movements. Specifically, D2.2 seeks to understand the mechanistic dependencies between interacting natural hazards, such as a storm inducing flooding leading to subsequent landslides. The report elucidates the interconnections between primary and associated hazards across various spatial and temporal scales. Furthermore, it provides projections regarding changes in hazard frequency and severity, grounded in the principal natural hazards identified within each testbed.

The findings of this report serve as input data for Work Package 3 (WP3), which is tasked with developing a people-centred risk assessment for each testbed. This assessment is then integrated into the DSS portal to enhance local and regional disaster risk management as part of Work Package 4 (WP4).

1.1 Objectives of this deliverable

This report serves as the main deliverable of Task 2.2: **Assessment of the primary interacting hazards across Europe.** It builds upon the work laid in Task 2.1, which focused on reviewing quantitative methods for assessing multi-hazard interactions and proposing a framework applicable to assessing present and future multi-hazard interactions and impacts, particularly those influenced by climate change (Kennedy *et al*., 2023).

The objectives of Task 2.2 are as follows:
- To identify the relevant interacting hazards for each testbed.
- To determine a set of intensity measures to be utilised as an input for WP3.
- To assess intensity measures of potential future interactive hazard pairs, considering the impact of climate change.

In the context of climate change, accurately assessing hazards and associated risks, particularly those stemming from infrequent multi-hazard events like floods and heatwaves, encounters two main challenges. Firstly, there is a lack of comprehensive and extensive observational data. Secondly, there is significant uncertainty regarding future local and global climatic conditions, including factors such as the distribution of extreme precipitation events and trends in urban development. These limitations result in substantial uncertainties in the outcomes and a potential tendency to underestimate the probabilities of emerging risks. Consequently, the MEDiate project emphasizes efforts to expand the existing observational database and maximize the utility of available data.

This investigation is benefited by interactions with ongoing EU initiatives (e.g., MYRIAD-EU). The analysis draws upon ensembles of climate datasets, including those from EURO-CORDEX and the latest CP-RCM runs available under H2020 EUCP (e.g., CMIP5, CMIP6). We adopt a contemporary typology, along with cutting-edge methods and research findings, to construct a plausible framework for diagnosing and classifying Europe's predominant interacting hazards and cascading impacts, both presently and in the future. This deliverable utilises a variety of datasets with varying resolutions, with a particular focus on those from the Copernicus Climate Change Service (C3S) of the Copernicus Earth Observation Programme of the European Union. Detailed descriptions of hazard-specific datasets can be found in sections 4 and 5.

1.2 The MEDiate testbeds

This investigation spans across four distinct testbed locations—Oslo (Norway), Nice (France), Essex (UK), and Múlaþing (Iceland)—across Europe. To gauge the significance and nature of multi-hazards in these testbeds, historical events within each location are considered. These events serve as examples of the types of multi-hazard interactions that necessitate modelling within the MEDiate platform under development. The framework outlined in this deliverable builds the foundation of this platform. While various hazards, including meteorological, hydrological, climatological, and geological hazards, are observed in the testbeds, the primary focus lies on the interactions among meteorological, hydrological, and climatological hazards (such as compounding events) to assess the impact of climate change. Geohazards are also examined, particularly regarding their role as triggers for interactions between landslides and climate-related hazards. A brief description of the testbeds, including an overview of multi-hazard events, is given below.

1.2.1. Oslo testbed

The study area encompasses the municipal boundaries of Oslo (Figure 1.2.1), a coastal city in Norway with a moderate population density (650,000 inhabitants and a surface area of 454 km^2). The climate profile report of Oslo (Klimaprofil Oslo og Akershus, KSS 2022) lists "extreme rainfall", "rain floods", "landslides, floods and mudslides" and "storm surge" as hazards that have probable increase based on analyses of downscaled climate models as was stated already in the IPCC AR5 report (IPCC, 2013).

The most significant rainfall floods in eastern Norway typically occur during the summer or early autumn, coinciding with precipitation covering extensive areas. Many of the most devastating floods in Central Europe are attributed to a weather pattern known as the "Vb-tief or Vb-Zug" in Van Bebber's terminology (Van Bebber, 1882). While most Vb-tief occurrences affect Central Europe, they occasionally extend into Scandinavia. The Vb-tief is associated with blocking anti-cyclones in the North Atlantic Ocean, typically near Iceland, and over northeast Europe, near Finland. Warm air masses are prevalent in the east, while depressions often form in the Norwegian Sea near the coast of Norway, directing cool maritime air masses southward. Following a prolonged period of dry weather, rivers often experience minor floods. Subsequent rainfall can trigger more substantial floods once the ground becomes saturated (Roald, 2021).

The city of Oslo is susceptible to compound flood events, including riverine floods, storm surges, extreme rainfall, erosion, and landslides, all potentially occurring concurrently under specific conditions. For instance, an extreme storm event in mid-October 1987 over southern and eastern Norway caused significant damage to the Oslo fjord due to multiple types of flooding, including coastal and riverine floods, as well as extreme winds. During that event, a 30-day period with rainfall reaching up to 240% of the normal level was succeeded by a period where the maximum daily rainfall had a recurrence interval of 10–15 years. This led to floods in eastern Norway and southern Norway with a recurrence interval of up to 100 years. These rainfall conditions, coupled with spring tides and wind conditions recurring at least every 25 years, contributed to notably extensive floods along the coast. The storm caused damage amounting approximately 650 million kroner (147 million euros present value), surpassing the total natural damage compensation recorded in the period from 1982 to 1986 (Engen, 1988).

Furthermore, studies in Norway have identified precipitation, particularly short-term and intense rainfall, as the primary trigger for soil landslides, often exacerbated by rapid snowmelt or heavy rainfall (Nadim *et al*., 2009, Devoli, *et al*., 2019). This study focuses on rainfall-induced landslides and utilises events from the NVE landslide inventory (NVE, 2023).

The Alna region of Oslo exhibits medium-to-high susceptibility to quick clay landslides due to various contributing factors like ground characteristics, topography, erosion, and flood events. Climate change has amplified the frequency and intensity of weather-related hazards, leading to increased risk of quick clay

landslides in the Alna region. Heavy summer precipitation (100–200 m³/s) saturates the ground, and high river flow rates in the Alnaelva contribute to erosion in waterways, a significant trigger for such landslides (Nesheim, *et al*., 2022; Huang, *et al*.,2023). The floods and landslides are considered as a precondition to quick clay hazard and specifically when preceded by an unusually wet summer.

Figure 1.2.1 Oslo testbed region. The figure shows the location of a rain gauge (blue dot), tidal sensor, and the gauging station (red dot) on the river Gryta. Additionally, the closest nodes (green dots) used for extracting modelled surge and river flow data from global datasets are shown.

1.2.2. Nice testbed

The Nice-Côte d´Azur Metropolis is a French inter-municipal structure, situated in the southeastern part of France, around the city of Nice. It encompasses an area of approximately 1,500 km² with a population of more than 540,000 inhabitants (Figure 1.2.2). It features a diverse landscape that includes coastal plains in the south, bordering the Mediterranean Sea, as well as steep mountainous and rural areas in the north. The Metropolis faces various environmental challenges, including the risk of natural hazards such as heatwaves, drought, earthquakes, landslides, and flooding (coastal and riverine), particularly in low-lying coastal areas. Climate change also poses a growing concern, with rising temperatures and shifting weather patterns affecting the region's ecosystems.

The Nice Metropolis is characterized by small basins where the slopes are generally steep, and this makes the area very prone to flash floods. Flash floods have very short response times that sometimes lead to dramatic consequences in terms of casualties and damages (Braud *et al*., 2016). The city of Nice is crossed by the Lower Paillons River, a typical torrential river with low water levels throughout the year but that can be affected by violent floods (794 m³/s for a return period of 100 years) in autumn and winter (Game *et al*., 2023). These are normally the maximum rainy seasons, often characterized also by extreme events e.g., Storm Alex in October 2020, known as Brigitte in central Europe and Aiden in the UK and Ireland, brought powerful winds, intense rainfall, and thunderstorms. These weather conditions led to landslides and flooding in

southeastern France, northern Italy, and central Europe from October 2 to October 7, resulting in a minimum of 15 deaths (Copernicus, 2020). Moreover, part of the river crossing the city is covered, increasing the vulnerability of the area. To the east of Nice, there is the Var Valley, one of the main freshwater resources of the Nice Metropolis. The Var River is also subject to extreme events like the 5 November 1994 flood (Ma *et al*., 2016).

This region is also affected by coastal floods. On 16 October 1979, a tsunami hit the French Riviera around Nice, killing 8 people and generating large economic losses, such as the collapse of part of the building site of a new harbour at the Nice airport. The flood extension reached 150 m inland with a 3.5 m runup and a sea level elevation of 2.5 m above mean sea level (Sahal and Lemahieu, 2011). This specific event was probably triggered by anthropogenic factors but tsunami hazards, mainly triggered by earthquakes, also exist at a regional scale and can have a high impact on the population and infrastructure (Hassoun *et al*, 2014). Further, coastal floods can be generated by surge storms like during the more recent flood event on the 3 October 2015, which again led to high economic loss and several fatalities (Vinet *et al*., 2016; Bertrand *et al*., 2022).

The province of Nice is constantly affected by landslides. Among the annals of its history, one catastrophic event stands out—the 1959 Roquebillière Landslide. Triggered by torrential rainfall, this calamitous event induced a massive debris flow, wreaking infrastructure and claiming numerous lives. More recently, several landslides were triggered during high rainfall events in 2000 and 2020.

In the available documentation of landslide events within the province, a total of 3,532 events have been recorded. These data were adopted to understand and address the susceptibility of the region to such natural phenomena. A significant portion of this data was sourced from the BDMvT (Base de Donnée Mouvements de terrain), accessible through Géorisques (BDMvT, 2024). Developed and maintained collaboratively by organizations such as BRGM, CEREMA, and RTM since 1994, this database provides insights into the spatial distribution, temporal trends, and characteristics of landslides across France. Furthermore, in pursuit of a comprehensive understanding, additional data were collected through photo-interpretation techniques (LUCAS, 2023).

As a direct consequence of global warming, the Nice Metropolis is increasingly affected by heat and drought. Recent analyses show clear summer warming and drying trends in Europe in recent decades, especially in the Mediterranean region, such as the south of France (Tauling, 2018). For example, summer 2003 was exceptionally hot and dry due to a combination of very low precipitation and extreme air temperatures. Moreover, sunshine duration was above normal and relative air humidity was below normal during the whole year (Rebetez *et al*., 2006). A decrease in annual precipitation will also contribute to an increase in winter droughts. These extreme events are liable to increase regionally due to the variation in rain patterns led by climate change as well as the occurrence of recurrent droughts and heat waves. Repeated droughts happened for instance from 2004 to 2007. One of the most recent events occurred in the summer 2015 which was characterized by pronounced drought, a heatwave and very low precipitation (Hauser *et al*., 2017)

Figure 1.2.2 Nice testbed region. The figure also shows locations of observed tide and river gauges (red dots) and the closest nodes (green dots) selected for extracting modelled surge and river flow data from the global datasets.

1.2.3. Essex testbed

Essex, situated in the east of England (UK), is a low-lying region with a surface area of 3,670 km^2 and boasts a 905 km long coastline (Figure 1.2.3). Bounded by the North Sea to the east, Suffolk to the northeast, Cambridgeshire to the north, Hertfordshire to the west, and Greater London to the southwest, Essex features the city of Chelmsford as its county town. Essex has a population of 185,000, mainly concentrated in the south of the county while the remainder is largely rural. The coastline is flat and deeply indented by estuaries.

The geographical configuration of Essex, characterized by an extensive coastline and a network of rivers and canals traversing urbanized areas, makes the region prone to combined river and coastal flooding, as evidenced by five nationally defined flood risk areas. The Essex County Council Local Flood Risk Management Strategy (2013) addressed various flood risk types, including flash flooding caused by high-intensity rainfall and groundwater flooding, occurring when water levels in the ground rise above the ground surface. Moreover, the southern North Sea is susceptible to significant storm surges, due to the narrowing of the English Channel and being relatively shallow compared to deeper basins to the north. This bathymetry funnels waves onto low-lying coastal margins. Thus, when extreme wind and wave forcing coincides with high spring tides there is the potential for extensive sea flooding (Spencer *et al*., 2015). This hazard is escalating because of climate change which is leading to a rise in the frequency of flood incidents on the south and southwest coasts of Britain, as already observed during the 20th century (Zong and Tooley, 2003). The Preliminary Flood Risk Assessment (PFRA) for Essex County Council reported approximately 1,300 local flood events over fifteen years.

Historically, the Braintree and Witham areas (Braintree District of Essex) have been susceptible to significant flooding from fluvial and surface water sources (Essex Pluvial Model Update Braintree, BMT, 2020). Additionally, south Essex faces sea-level rise and flooding in the Thames Estuary (Steed, 2023). The

benchmark storm surge event for the region occurred on 31 January–1 February 1953, which, in total, caused the deaths of over 2,000 people in UK, Belgium and the Netherlands. This is considered the most devastating natural disaster in NW Europe in the last century (Spencer *et al*., 2015). A southern North Sea event of comparable magnitude occurred between 5 and 6 December 2013 (almost 60 years later). These events produced similar surge heights but the 1953 storm was dominated by the surge component, while the 2013 event was also characterized by a large tidal component (Wadey *et al*., 2015).

The winter of 2013/2014 was not only characterised by a single storm event, but it was also exceptionally wet and stormy as a succession of deep Atlantic low-pressure systems, associated with a powerful jet stream. It was the wettest winter in the UK's observational records, and the stormiest period of weather experienced for at least 20 years (Kendon and McCarthy, 2015). The major storm-surge on 5–6 December was followed by a sequence of major storms from mid-December to early January with strong winds and heavy rain that brought multiple fluvial and coastal flooding. This co-action of wind and rain is of particular interest to increase our knowledge of multiple or compound hazards, not only because strong wind is usually accompanied by continuous rainfall, but also because climate change leads to large-scale shifts in weather patterns that directly influence the co-occurrence of these hazards (Bi *et al*., 2023).

Moreover, the winter 2013/2014 was very mild. The UK mean winter temperature was the fifth highest from 1910, with an absence of cold spells (Kendon *et al*., 2015). In general, over the last decade, Essex has been subject to major overheating events and the duration and intensity of heatwaves are expected to increase due to global surface temperature rise. In summer 2022, for example, a daily maximum temperature of 40.3°C was reached on 19 July making it the hottest July heatwave in the UK (Yule *et al*., 2023).
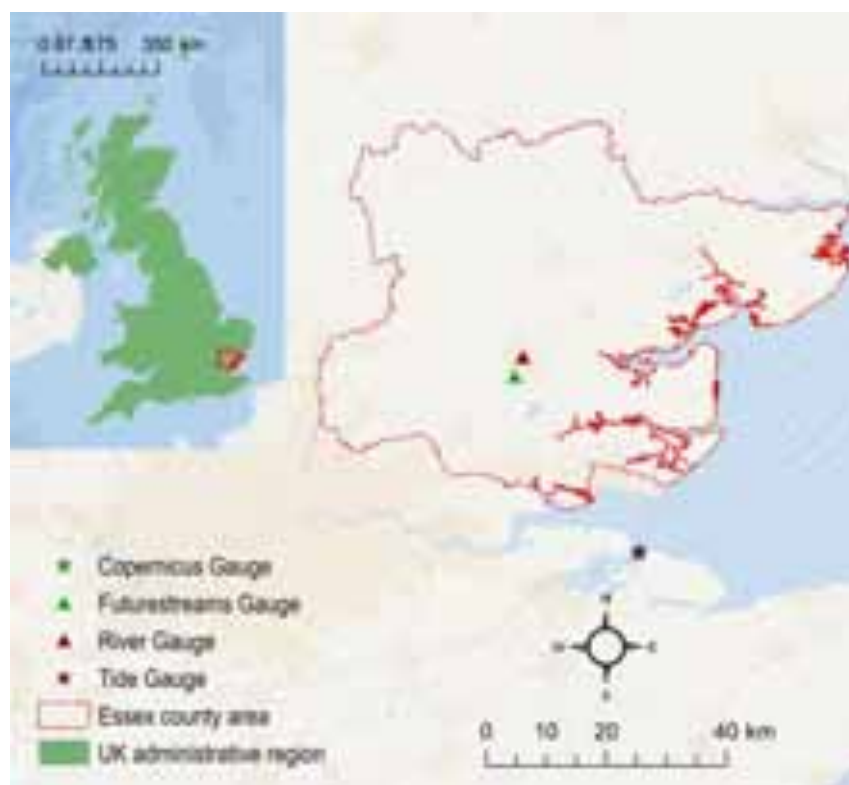
Figure 1.2.3 Essex testbed region. The figure also shows locations of observed tide and river gauges (red dots) and the closest nodes (green dots) selected for extracting modelled surge and river flow data from the global datasets.

1.2.4. Múlaþing tesbed

Austurbrú is the Association of Local Authorities of all municipalities in East Iceland (Austurland) (Austurbrú, 2024), and it operates in all administrative matters related to this region. East Iceland covers the area from Vopnafjörður in the north to Krossnes in the south and has four municipalities: Fjarðabyggð, Múlaþing, Fljótsdalshreppur and Vopnafjarðarhreppur. In this report, the testbed is Múlaþing and more precisely the town of Seyðisfjörður. The municipality covers 10.671 km^2, with a population of 5.359, but the town of Seyðisfjörður had a population of 685 as of 2019. The mountainside south of Seyðisfjörður is characterised by varied terrain including summits, large depressions, gullies, and cliffs. Standartindur on the south side rises to 1010 m above sea level and Bjólfur, on the northern side of the fjord, is 1085 m high (Figure 1.2.4 and Figure 1.2.5).

The main natural hazards in Múlaþing – Seyðisfjörður are snow avalanches and landslides, collectively called "ofanflóð" in Icelandic. In 1995, two avalanches caused a total of 34 fatalities within residential areas in the Westfjords of Iceland. This led to an increase in avalanche research and development of a methodology for hazard zoning based on the individual risk, or annual probability of death due to avalanches. This approach has then been expanded also to account for landslides and is now a "ofanflóð" hazard assessment. The method considers the estimation of avalanche frequency, the run-out distribution, and the vulnerability, which is estimated using the data from the fatal accidents in 1995 (Arnalds *et al.*, 2002). In a strict sense, the so-called "hazard" zoning is a risk zoning, but in Icelandic language the word "hazard" is used. According to this method there are defined three hazard zones, A, B and C, which are defined by the presence of acceptable risk. In hazard zone A, the acceptable local risk lies between $0.3 - 1.0 \times 10^{-4}$ (yellow risk line), in zone B it is between 1.0 and 3.0×10^{-4} (blue risk line), and in zone C, the level is 3.0×10^{-4} (red risk line). For each category, there are spatial planning rules in force and provisions to reduce or mitigate localised risk. Above the highest risk line (line C) constructions of new houses is forbidden. Notice that the red line (line C) extends into the sea to prevent infilling and reclamation of land for building purposes (Figure 1.2.5).

Figure 1.2.4 Múlaþing testbed region. The figure also shows locations of Seyðisfjörður town and data stations (green and red dots).
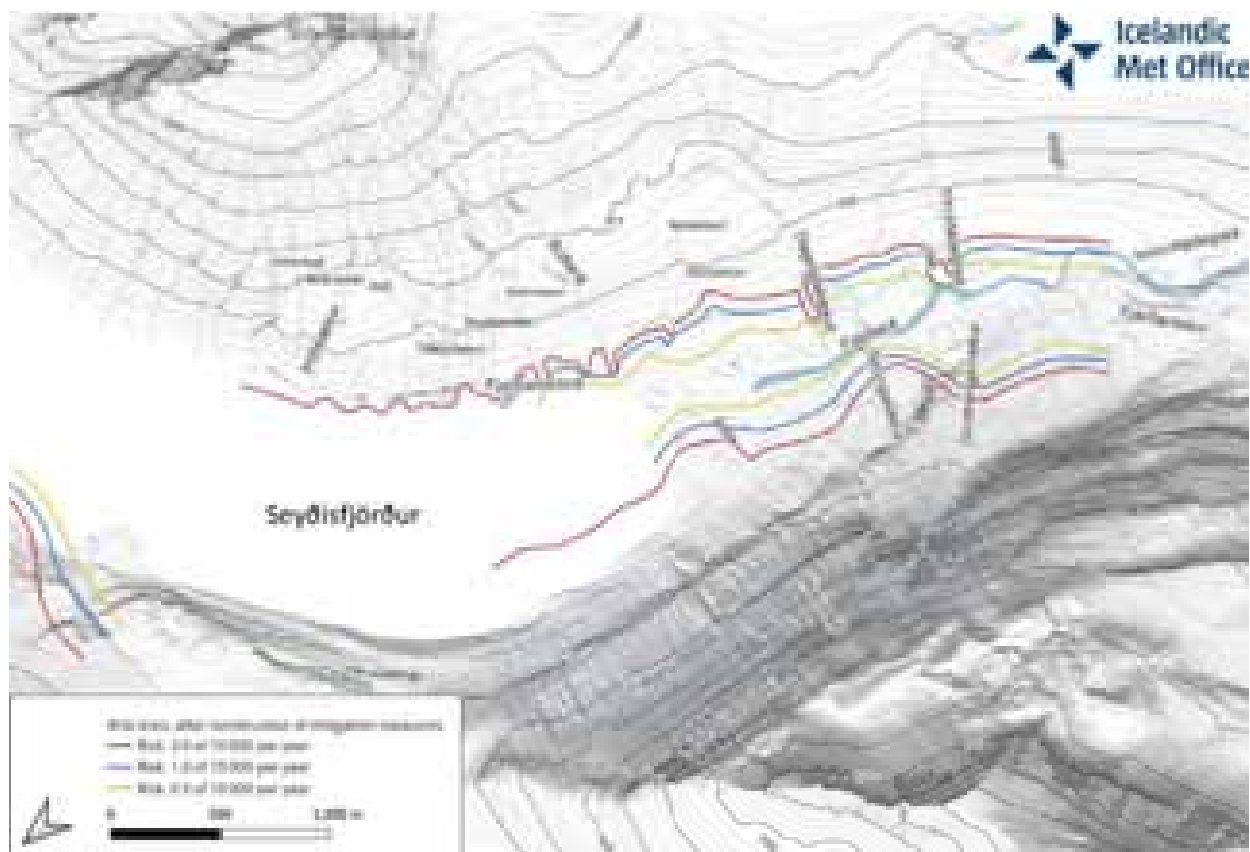
Figure 1.2.5 Hazard (risk) map in force with place names as mentioned in this section. The coloured lines define the points on which the individual risk, or probability of death due to avalanches is respectively 3.0×10^{-4} (red line), 1.0×10^{-4} (blue line) and 0.3×10^{-4} (yellow line). The extension of the zonation into the sea is intended to prevent future construction from reclaimed land.

During the week 14 – 18 December 2020 several debris flows and a 74,000 m^3 landslide occurred in Seyðisfjörður, destroying many businesses and homes but with no casualties. The event led to the total evacuation of the town for several days. The landslide hazard assessment was revised, and mitigation was planned (Gylfadóttir *et al*., 2021). The town of Seyðisfjörður has been known for its landslide hazard for several decades and especially after the fatal landslide in August 1950. The landslide inventory includes a short description of that event: "Great damages occurred and 5 people were killed, when a large debris flow hit the house Strönd. Many smaller debris flows fell this day (17 were counted) most of them on Fjarðarströnd" (Jensen and Sönser 2002, Gylfadóttir *et al*., 2019).

In Seyðisfjörður snow melt, especially during late winter and/or springtime, can lead to slush flows within a stream and, as cascading effects, debris floods, hyper concentrated floods or floods can propagate in inhabited areas. A slush flow is defined as a flowing mixture of water and snow which can entrain soil or debris on its propagation path (Hestnes, 1998). For this kind of hazard, the physical conditions of the stream or channel define the potential of occurrence of slush flows (Gylfadóttir *et al*., 2021).

The river Hádegisá runs from a plateau towards the base of valley, passing three main rock bands that interrupt the slope to form steps (Arnalds *et al*., 2002). This type of slope morphology allows snow to accumulate, and during melting, slush flows are possible. On 21 February 1904, a slush flow from Hádegisá reached the river Fjarðará at the valley bottom (nr. 4023 in IMO inventory). From historical accounts, there were reports of heavy snowfall during January 1904, followed by a rapid thaw on 21 February. Many slush

flows and snow avalanches fell at the same time in the same area due to the destabilisation of the snow during the intense thaw.

More recently, a slush flow occurred in Hádegisá (no. 55041 in the inventory of IMO) on 23 February 2019. At the time, the whole area of the Eastfjords where subjected to slush flows and 16 events were recorded. The weather conditions were similar to the ones in 1904 with rapid thawing of pre-existing snow cover. However, this slush flow did not reach the river Fjarðará, with subsequent flooding further downstream.

Many historical events of snow avalanches have been recorded in above the town of Seyðisfjörður. Among them the most fatal of all recorded snow avalanches in Iceland, the event of 18 February 1885, where 24 people we killed. In the IMO snow avalanche inventory, the following description can be found: "A large avalanche fell from Bjólfur reaching from Jókugil to further out than Hlaupgjá. Many houses were destroyed and 24 people were killed." (Arnalds *et al*., 2002).

2   SCOPE OF THE REPORT AND DEFINITIONS

The focus of this report is primarily on the interactions between hydrological, meteorological, and climatological hazards (flooding, heatwaves, cyclones and wildfires), in addition to geophysical hazards such as mass movements (landslides). These natural hazards can interact in ways that impact areas beyond their immediate surroundings. Floods can cause landslides, storms can bring heavy rain, which can lead to flooding and the triggering of landslides. These hazards can occur over both time and space. They can be hard to predict, rapidly changing, and difficult to mitigate. As the planet warms, natural hazards are becoming increasingly frequent and severe (IPCC, 2022), and communities are not used to such rapid changes. This can lead to communities becoming more vulnerable to natural hazards.

The project uses Participatory Action Research (PAR) to involve municipalities in the testbeds (Komendantova *et al*., 2023). The PAR work formed part of WP1 in the MEDiate project, and the authors of this report took part directly in the assessment and analysis of the survey results. Each testbed leader selected three multi-hazard pairs that represented vulnerabilities for the region in question. Stakeholder needs from each testbed were communicated to WP2. Hazard pairs in this report were defined according to the needs of each testbed.

2.1   Definitions

Definitions for WP2 were covered extensively in the deliverable of Task 2.1 (Kennedy *et al.,* 2023). However, some terms need to be defined more precisely for this report as they feature widely in the treatment of hazard interactions, driving mechanisms, and the sequencing of hazard occurrence. The definitions below are refined versions of the nomenclature of Kennedy *et al.* (2023). They are also part of the UNDRR classification system for hazards (UNDRR, 2020).

Compound hazard is often used as an alternative or is near synonymous to the term multi-hazard and therefore these terms are adopted in this report as having the same definition.

Hazard driver: In the IPCC AR6 report (IPCC, 2022), climate change is defined as a significant hazard driver that can impact multiple hazard types and contribute to their interactions. Changes in temperature, precipitation patterns, sea levels, and weather events associated with climate change can intensify or alter the occurrence of various hazards. For example, rising temperatures can lead to more frequent and severe heatwaves, while increased rainfall can elevate the risk of flooding and landslides. Hazard drivers are factors or conditions that

contribute to the occurrence and severity of hazards. When it comes to interacting hazards, hazard drivers play a crucial role in shaping the interactions and interdependencies between different types of hazards.

Intensity measures: Overall, intensity measures provide a quantitative basis for understanding and assessing the severity of various natural or human-induced phenomena, enabling better risk management, mitigation strategies, and decision-making processes. In wind engineering intensity measure describes the strength of wind loads on structures, in meteorology, it quantifies the severity of weather phenomena such as rainfall, snowfall, windstorms, or hurricanes. In the context of statistics or probability theory, intensity measure refers to quantities that characterize the severity or strength of an event or phenomenon.

Multivariate events: Multivariate events refer to natural hazard events that involve the simultaneous occurrence or interaction of multiple hazards. These events can have complex and interconnected dynamics, resulting in increased risks and impacts. Multivariate events can occur in spatial or temporal proximity. For example, a hurricane can bring together strong winds, heavy rainfall, and a storm surge, leading to a multivariate event with compounding effects. Multivariate events can also be preconditioned if the occurrence or severity of one hazard is influenced by prior conditions or factors.

Preconditioned events: Preconditioned events involve natural hazard events that are influenced or modified by prior conditions or factors. These conditions can increase the likelihood or severity of the hazard event. Preconditioning factors can be spatial or temporal in nature. For example, an area that has experienced prolonged drought is more susceptible to wildfires, or an area with already saturated soil is more prone to flooding. Preconditioned events can also involve multivariate aspects, where multiple factors interact to increase the risk or impact of a hazard event.

Secondary hazard: The indirect consequences or effects that arise because of the primary hazards. Secondary hazards can be equally, if not more, damaging and can include effects such as landslides triggered by earthquakes or a storm-surge because of an extreme cyclone or hurricane.

Spatially compounding events: Natural hazards that occur in close spatial proximity to each other. These events may be different hazards or related phenomena happening in the same geographic area. Spatial co-occurrence events can include preconditioned or multivariate aspects. For instance, wildfires can lead to increased landslide risks in the surrounding area due to the loss of vegetation cover, creating a spatial co-occurrence of two hazards.

Temporally compounding events: Natural hazards that happen in close temporal proximity to each other. These events can be separate hazards or related phenomena happening within a relatively short timeframe. Temporal co-occurrence events can exhibit preconditioned or multivariate characteristics. For example, a strong earthquake followed by aftershocks over a short interval constitutes a temporally compounding event, where the subsequent seismic hazards are caused by the initial mainshock.

Climate change is expected to be a significant hazard driver that can impact multiple hazard types and contribute to their interactions. Changes in temperature, precipitation patterns, sea levels, and weather events associated with climate change can intensify or alter the occurrence of various hazards. For example, rising temperatures can lead to more frequent and severe heatwaves, while increased rainfall can elevate the risk of flooding and landslides. Table 2.1.1 shows the selected climate impact drivers listed in the IPCC AR6 report for Europe.

Table 2.1.1 Climate impact drivers listed in the IPCC AR6 for North (NEU) and West Central Europe (WCE). Dec–Jan refers to change in mean precipitation in winter.

Geographical and geological characteristics of an area can act as hazard drivers and shape the interactions between hazards. Features such as steep slopes, proximity to rivers, or presence of susceptible soils can influence the occurrence of landslides, and subsequent cascading hazards like liquefaction. Hydrological and environmental conditions are crucial hazard drivers that influence interactions between hazards. Factors like rainfall intensity, soil saturation, river flow rates, or coastal processes can affect the occurrence and severity of flooding, erosion, and related hazards. Changes in these factors can influence the timing and synchronization of hazard events and potentially amplify their impacts.

3   METHODS AND OVERVIEW OF HAZARD INTERACTION TYPES

This section is structured into five sections describing the methodologies used to define the interacting hazards in four testbed regions (section 3.1), selecting the appropriate measures to analyse joint probability, hazard pairing for possible future events, and four categories of multi-hazard events (section 3.2–3.5).

To identify relevant types of hazard interactions across the four testbeds, this project employs the Participatory Action Research (PAR) approach (Komendantova *et al.,* 2023), involving stakeholders from each testbed. In the PAR process, participants from each testbed selected the most pertinent hazards from a predefined list for their respective areas. In the initial PAR cycle, primary hazards within the testbed regions were identified (Figure 3.1.1).
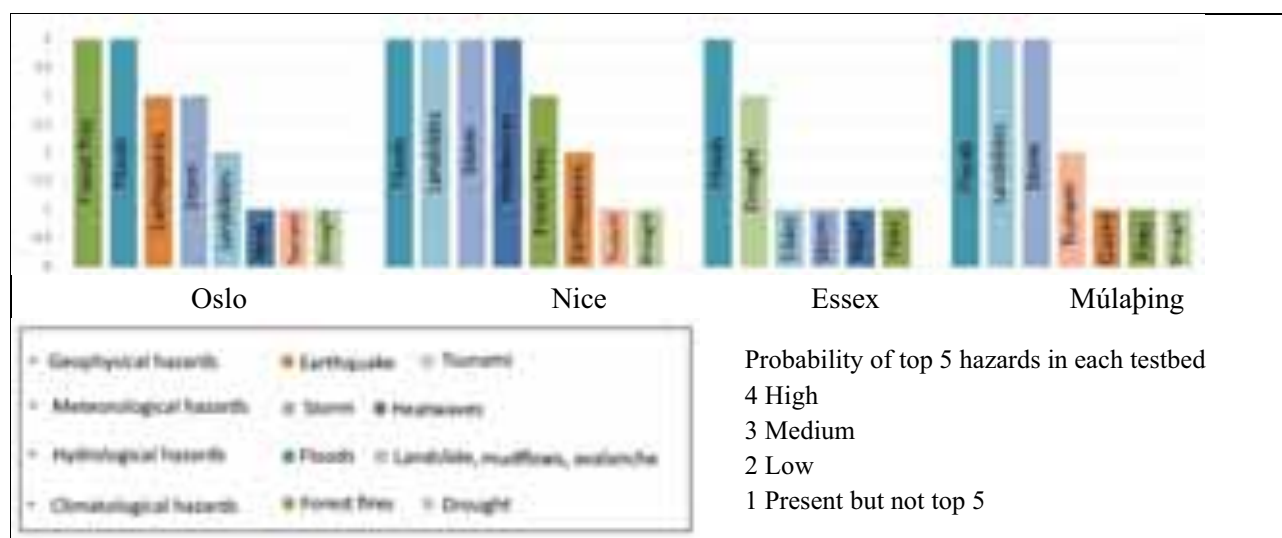
Figure 2.1.1 Hazards priorities in testbeds from the PAR process.

It is evident from Figure 3.1.1 that the first PAR process primarily focused on single-hazard events. To identify relevant interacting hazards, in line with the primary objectives of this deliverable, a PAR workshop was convened in June 2023. During this workshop, the concept of interacting hazards—where hazards combine, trigger other hazards, or lead to cascading impacts—was deliberated (see Figure 3.1.2). The primary natural hazards (Figure 3.1.1) identified during the previous PAR workshop served as a foundational basis for analysing and comprehending the interactions among these hazards. Additionally, the workshop introduced a typology of interacting hazards, encompassing preconditioned and triggering, multivariate, spatially compounding, and temporally compounding events (Figure 3.1.2). These four categories of multi-hazard events were selected to offer diverse perspectives for understanding and analysing the intricate nature of natural hazards and their interactions. These typologies align with the categorisation framework proposed and employed in various recent studies (Zscheischler *et al.*, 2020; Lee *et al.*, 2024). These categories underscore the interconnectedness, dependencies, and compounded risks arising from the simultaneous occurrence, proximity, or antecedent conditions associated with hazard events.

Following the introduction of the multi-hazard typology, discussions were held with stakeholders to identify suitable multi-hazard events within their respective testbed regions. An evaluation of potential interactions among various individual hazards was undertaken (Figure 3.1.2). Subsequently, stakeholders identified three pairs of interacting hazards in each of the four testbed regions, prioritised accordingly (see Table 3.1.1). A variation in the order of hazards can be observed between Figure 3.1.1 and Table 3.1.1, underscoring the fact that while some hazards may have less individual impact, their interactions with other hazards could result in potentially significant effects.
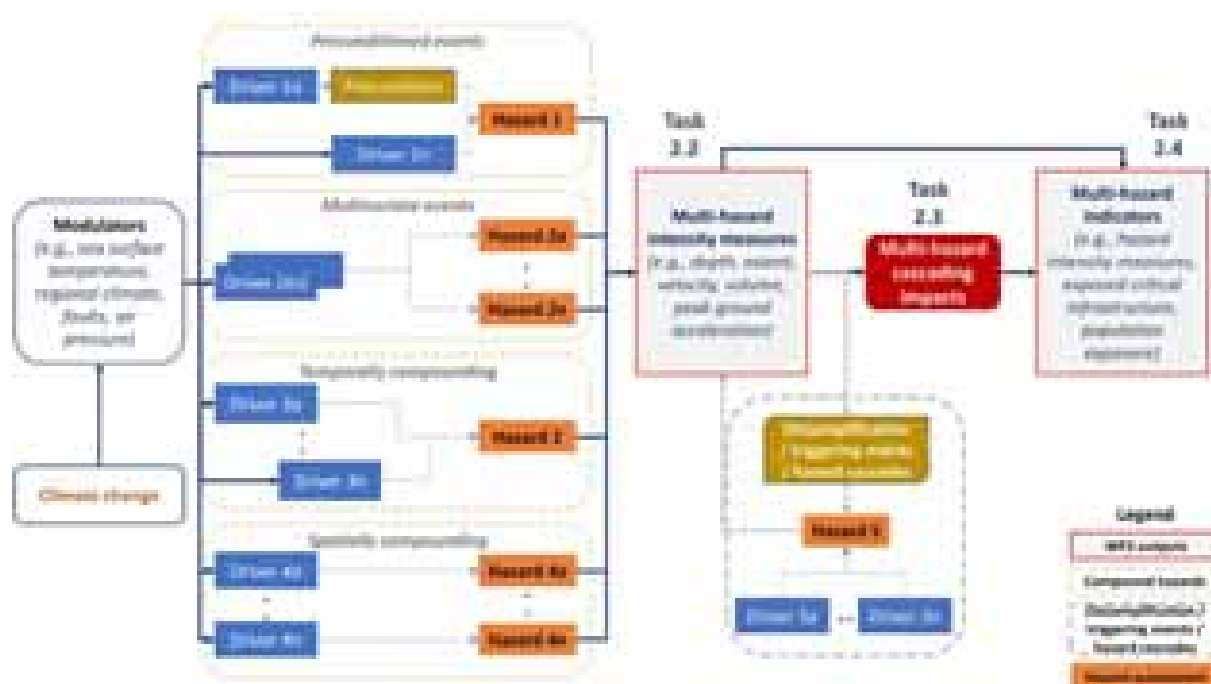
Figure 2.1.2 Multi-hazard interaction diagram, showing the interconnectedness and dependencies between hazard drivers. The diagram also shows the connections between tasks within WP2 (Kennedy *et al.*, 2023).

Table 2.1.1 Identified multi-hazards of importance to each testbed.

Testbed	Multi-hazard interactions	Typology
Oslo	1. Compound flood (coastal and riverine)	Multivariate
	2. Flood and quick clay	Preconditioned and triggering
	3. Flood and landslide	Triggering
Nice	1. Compound flood (coastal and riverine)	Multivariate
	2. Flood and landslide	Triggering
	3. Extreme heat and drought	Temporally compounding
Essex	1. Extreme wind and rainfall	Spatially compounding
	2. Compound flood (coastal and riverine)	Multivariate
	3. Extreme heat and rainfall	Spatially compounding
Múlaþing	1. Heavy rain and landslide	Preconditioned and triggering
	2. Snow melt and flood	Preconditioned and triggering
	3. Heavy snowfall and avalanche	Preconditioned and triggering

3.1 Preconditioned and triggering events

In this report the triggering relationship between hazards is when one hazard causes another hazard to occur. The definition also suggest that the hazard can trigger zero, one or more secondary hazards (D2.1 report, Kennedy *et al*., 2023). The triggering hazards considered here are of meteorological and climatological nature. Figure 2.1.1 shows the method for evaluating the triggering hazard on a hillslope scale. The diagram allows for a focused assessment of hazards that can affect local conditions.
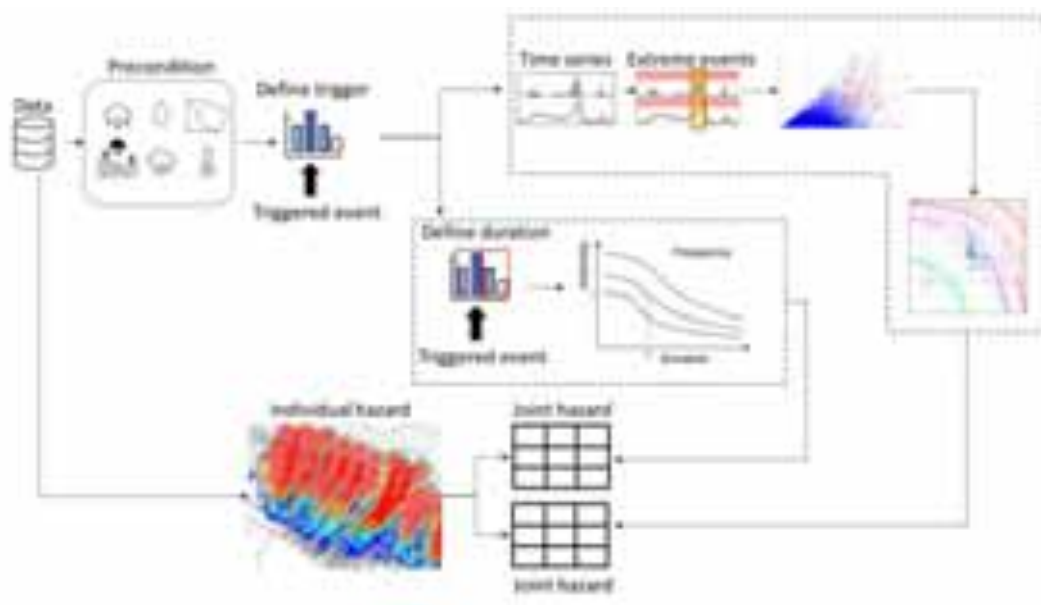
Figure 3.1.1 Conceptual framework for estimating intensity measure of preconditioned and triggered events.

In the case studies discussed later in the report (section 5), we are dealing with precipitation as a trigger for landslides, snow avalanches and floods. We also analyse snow melt as a trigger for floods and the trigger is a

combined hazard of extreme rainfall and temperature increase where the precondition is snow. Figure 3.1.1 shows the workflow of preparing the data to define the trigger and calculate the probability of the triggering event in connection to the relevant hazards.

Selecting a triggering event involves finding a peak in the timeseries. To link timeseries and triggered events it is necessary to define what a time series event is. Timeseries are measured in different ways and with different time resolutions. In some cases, where measurements are sparse or not available, modelled data are used. Convenient time resolutions are hourly or daily values based on the nature of the data. The time resolution of both datasets, triggering and triggered affects the accuracy of selecting the "correct" time series event. When the time resolution of data decreases, the size of the event needed to trigger a hazardous event becomes more inaccurate.

Methods for joining triggered events to the selected trigger (e.g., landslides to rainfall) may vary based on the geographical scale of the data. Joining landslide hazard to rainfall events on a regional scale requires a different approach than for a hillslope scale. The method described here looks at triggering events on a hillslope scale. The regional scale approach is described below.

Several methods are available to separate time series into events. The threshold-based method is simple, but more complex methods e.g., ARMA (Auto Regressive Moving-Average) and TDS (Time-Domain Statistics), which are statistical methods, DTW (Dynamic Time Warping) and wavelet transform, which are machine learning methods could be used. Selecting the correct peak causing a hazard event can be challenging especially in large datasets where possible changes in the conditions have occurred from first events to the last.

Extreme Value Analysis (EVA) is a statistical discipline used to predict the occurrence of rare events by assessing their frequency from the most extreme values of a dataset, either observed or simulated. These extreme values are found in the tails of a probability distribution. Conducting an EVA enables the estimation of magnitudes associated with occurrences over periods that may extend far beyond the duration covered by the available time series data. Two main methods for finding the return levels exist: the Block Maxima approach and the Peak Over Threshold (POT) approach (Coles, 2001). To estimate the probability of various rainfall intensities and durations frequencies (IDF), we need a statistical model that accurately represents extreme rainfall events.

Block Maxima

The Block Maxima approach consists of dividing a timeseries into non-overlapping periods of equal size and retaining only the maximum values within each period. When dealing with meteorological and hydrological data, it is common to use the maximum hourly or daily measurements values from each year. A new timeseries that includes only the maxima is thus generated and referred to as an Annual Maxima Series (AMS). Under extreme value conditions, the AMS follows a General Extreme Value (GEV) family of distributions of the form given in equation (1):

$$G(z) = exp\left\{-\left[1 + \xi\left(\frac{z-\mu}{\sigma}\right)\right]^{-1/\xi}\right\} \qquad (1)$$

where z is the extreme value and μ, σ and ξ are the three parameters of the GEV model $G(z)$, defining location, scale, and shape parameters, respectively. This three-parameter distribution unites the three possible extreme value distributions, namely type I (Gumbel), type II (Fréchet), and type III (Weibull). The choice of distribution type depends on the extreme value characteristics of the parent dataset. This can be established by the shape factor ξ. Once the GEV distribution has been fitted to the AMS, the return level r associated with the return period (RP) $1/p$ can be estimated.

The Block Maxima approach is a simple method to implement as the data pre-processing requires only the creation of AMS by taking the yearly maxima at the time frequency considered. However, the main weakness is the omission of many possibly significant events because they do not represent an annual maximum value, even though they could be larger than maxima from other years. Also, there is a small potential for including dependent events if the yearly maximum spans a change of year e.g., maximum of 48 hours precipitation passes the New Year.

Peak-over-Threshold

Another approach for EVA is the Peak-over-Threshold method (POT). In this case, all independent values from a timeseries that exceed a defined threshold are extracted and fitted to GPDs. The GPD has the following form, equation (2):

$$H(z) = 1 - \left[1 + \xi\left(\frac{z - \mu}{\sigma}\right)^{-1/\xi}\right] \qquad (2)$$

where x is the threshold excess, μ is the threshold, σ the scale parameter and ξ the shape parameter.

Most of the main issues encountered by the Block Maxima model from a physical point of view are solved by the POT method as the extreme values extracted from the time-series are not limited by their year of occurrence. However, the user must instead ensure independency of values and define a suitable threshold. In general, values in meteorological timeseries are dependent but, by declustering the data with a suitable minimum time window, the remaining values can be assumed approximately independent. The primary difficulty in configuring the POT model is finding a threshold that is sufficiently high to maintain the integrity of the Generalized Pareto Distribution (GPD) while also being low enough to extract an adequate amount of data from the original time series.

Event detection: Events are delineated by establishing a minimum measured value and then determining the gap between them by selecting the minimum number of zeroes. When events have been separated it is possible to analyse e.g., the duration, intensity, and volume of rainfall for specific periods, thus obtaining a clearer picture of rainfall patterns. Rainfall events can also be separated from snowfall events by filtering out events that have a defined temperature over a certain limit. Using R Studio, the code presented by loreabad6 (2024) on the Stack Overflow page was applied and adjusted to this purpose.

The Antecedent Precipitation Index (API): Antecedent Precipitation (AP) denotes the rainfall preceding a specific time, typically measured on the antecedent day (AD) within a designated area or basin. The API articulates this concept through a calculated aggregate of daily precipitation values, incorporating a weighted summation (Cordery, I., 1970; Xie and Yang, 2013; Ladson, 2016; Li *et al.*, 2021).

$$API_d = P_d + kP_{d-1} + k^2P_{d-2} + \cdots \ or \qquad (3)$$

$$API_d = \sum_{i=0}^{\infty} k^i P_{d-i} \qquad (4)$$

Where API_d is the Antecedent Precipitation Index for day d, k is an empirical decay factor less that one and P_d is rainfall for day d.

********************************   ********************************

API has been used to supplement relative soil moisture data (Zhao *et al.*, 2011). Some studies suggest normalised API (Heggen 2001; Ghosh *et al.*, 2021) and the decay constant k has been analysed (Li, *et al.*, 2021). The decay constant value is traditionally an empirical single value, often between 0.80 and 0.98 (Lindsay *et al.*, 1975). When analysed in context with landslides, the API has been known to add less weight to rainfall intensity contributions further back in time, as reported by Crozier *et al.* (1980) and Crozier (1986).

A combined method of defining extreme rain events: This method uses the multivariate part of the code described in section 3.3. Daily API can be joined with predefined rolling blocks of 24-, 48- and 72-hour rainfall intensity. This can be done after the flagged events have been linked to landslide events and duration of rainfall triggering events had been confirmed. The combined values are then selected with the POT method (mainly to select the predefined blocks) and a running window of 3–7 days. The resulting "joint events" are linked to "triggered events" to estimate the "hit" score.

Usually, hazard event inventories (here so-called triggered events) only have some of the events accurately timed. They may be assumed to be dated correctly but the time during the day is often not known. Therefore, when connecting a hazard event to a time series event it is not enough to look forward since the triggered event might have occurred around mid-day, but it might be recorded happening in the early morning (00:00 if time is not known) and therefore would be flagged the event number before. If the hazard event inventory is likely to have inaccurately dated events a window of 5–10 days (1–5 days before and 5 days after) might be needed to link the most likely triggering events depending on the duration of the rainfall event triggering the hazard event. As an example, predefined blocks of rain are dated based on their peak. When using a three-day block, the window must look back two days (in case the triggering event had shorter duration than 72 hours). Tsunetaka (2021) provides a thorough description of using IDF curves with estimated return periods of landslide-triggering rainfall events by standardizing the rainfall period.

The result is a list of extreme events. The threshold defined in the POT method filters out the most likely events. When the threshold is set at a low level, numerous extreme events are identified, but the effectiveness of the "hit" score diminishes due to the lower ratio of triggered events to extreme events. When the threshold is raised, the "hit" score is expected to increase, but there is a risk of overlooking triggered events resulting from less intense yet prolonged events.

The extreme events with missing hazard events might have natural explanations and are therefore not necessary failures. This is where the precondition comes in. The time of the year can explain why joint extreme events (high rainfall intensity and high antecedent rainfall) do not trigger a landslide. Even though the temperature during the rainfall events is above the freezing point the earth might be frozen. Also, a simple explanation might be a hillside that suffered a landslide erosion the year before (or even a decade before depending on the supply of loose material) might not respond to the same extreme events for some time. The analysis of extreme measured or simulated precipitation must consider uncertainties in measurement accuracy and unavoidable simplifications in meteorological models. Massad *et al*. (2020) list ten pertinent influences when considering extreme runoff at a catchment scale. One of these is the difference between daily and 24-hour data. It must be noted that difference between hourly and daily data can vary. With only one data point per day, daily time series tend to smooth out intraday variations and emphasize longer-term trends and patterns. Differences between daily precipitation from midnight to midnight and precipitation accumulated over any 24-hour window exist. As an example, for Iceland, results showed a that the 24-hour accumulated precipitation events were 13% higher when comparing the 50 highest daily accumulated values in a selection of 12 stations. While comparing results from the daily precipitation with a 5-year return period to the 24-hour precipitation with a 5-year return period, median differences in all grid points covering the country is 14% (Massad *et al.*, 2020).

Trigger-Driven Joint Extremes

The identification of the joint extreme events follows a procedure similar to that described for the multivariate events (section 3.3, below). A preliminary identification of the extreme events for both triggering timeseries (first timeseries hazard-1) and triggered timeseries (second timeseries hazard-2) is performed using either the threshold–excess method without separating dependent peaks or POT analysis. Then, for any independent extreme triggering event, the eventually linked triggered event is identified. The identification is performed considering a search window that extends from the time of the triggering event for a desired period (usually 3–7 days) (Figure 3.1.2). The length of the search window, as well as the thresholds used for the identification of the extreme events, can be defined based on Kendall's coefficient. Moreover, the length of the window cannot exceed the distance between two consecutive extreme triggering events to ensure their independence. If at least one extreme event of the second timeseries (hazard-2) is found inside the search window, the analysed triggering event is considered to trigger the found event. If more than one event is found inside the search window, only the maximum value is considered. The extreme triggering events that do not trigger any events of the second timeseries are not considered in the following probabilistic analysis.

The RPs for the joint peaks are then calculated with copula Stan, explained below (equations 1–9) for datasets with acceptable Kendall's rank correlation coefficients and thresholds as well as number of extreme events. Climate data preparation can be handled the same way, but often the time resolution of climate projected data is more than an hour (e.g., daily). Depending on the dataset, the relevant method for dividing the events must be chosen.
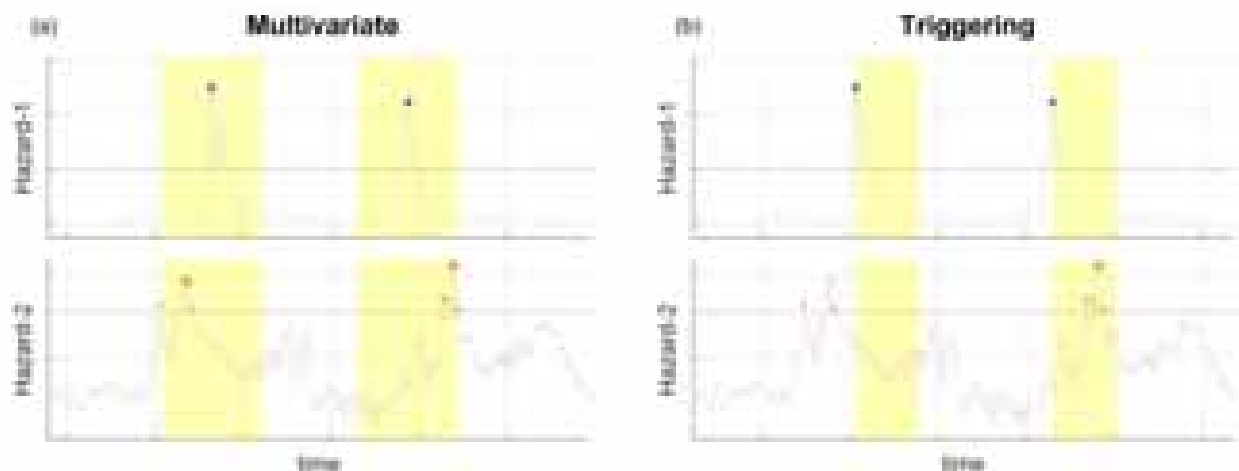
Figure 3.1.2 Examples of search windows for Triggering (a) and Multivariate (b) analysis. Blue asterisks are extreme events for Hazard-1 timeseries, red points are extreme events for Hazard-2 series, and red circles are the maximum extreme events for Hazard-2 timeseries inside the search window.

Rainfall-induced hazard assessment at a regional scale

In this subsection, the regional-scale landslide hazard assessment, including the effect of rainfall intensity, is discussed.

Spatial probability

The *landslide inventory* records the date and location of each event on a map. The *landslide susceptibility map* (Fell *et al.*, 2008a, 2008b) is generated using the landslide inventory and various (pre-)conditioning factors such as elevation, slope, aspect, and lithology. This map illustrates the distribution of the Landslide Susceptibility Index (LSI), which is an index ranging from 0 (no landslide susceptibility) to 1 (the most

susceptible to landslides in the area). These maps are typically valuable for land use planning, disaster risk reduction, and emergency management purposes, as they help identify areas where landslides are most likely to occur and where preventative measures should be prioritized. Many approaches exist to build a susceptibility map; an example is illustrated in Gautam *et al.* (2021), where different methods have been employed to derive susceptibility maps. The susceptibility map can be created using either slope units or pixels. Here, a pixel-based study is performed.

Since the LSI index (0−1) is only a comparative measure of the landslide susceptibility within the area, the LSI index cannot be directly treated as the landslide spatial probability. The spatial probability is determined using the relationship between the landslide ratio (LR) and LSI. The LR is the ratio between the number of landslides $[N_L(SC)]$ and the total number of pixels for each susceptibility class ($N_{pixels}(SC)$). The assumption is that all pixels that have the same LSI have the same landslide spatial probability, as stated in equation (5).

$$LR(SC) = \frac{N_L(SC)}{N_{pixels}(SC)} \qquad (5)$$

The spatial probability is calculated by plotting the relationship between the LR and the various value intervals and converting the various susceptibility indices to spatial probability. Typically, LR increases with LSI. An application is illustrated in Wu and Chen (2013).

Rainfall events triggering landslides and rainfall threshold.
From the exact date of each landslide event in the landslide inventory, it is possible to determine the rainfall intensity that triggered it. In cases where actual rainfall gauge measurements are lacking, ERA5 data (Hersbach *et al.*, 2023) can be utilized to estimate rainfall intensity at any point on the map, albeit at a coarse resolution of approximately 31 km. Within each cell, rainfall intensity data over time are available. These data are processed over the period covered by the landslide database to establish a proxy for rainfall intensity, termed the effective accumulated intensity (e.g., Wu and Yeh, 2020). Different measures exist to compute this proxy, for instance, computing the accumulated rainfall for the preceding *n* days, or by computing a weighted average over *n* days. To refine the proxy, different proxies may be combined, such as an effective accumulated intensity combined with a daily rainfall intensity.

Rainfall intensity values can be discretized to simplify subsequent calculations. By analyzing rainfall data, it is possible to compute the density function and (joint) cumulative distribution of rainfall intensity, i.e., describing the correlation between rainfall intensity and its probability of occurrence. For instance, a rainfall intensity corresponding to the 95th percentile means that only 5% of rainfall events in the observed database period exceeded that intensity. With information on the date and intensity of rainfall events in the database, it becomes feasible to construct a database containing rainfall events with associated intensities. These events may be distinguished into two groups: events with and without landslides.

A rainfall threshold (R_T) may be used to distinguish the two groups, i.e., separating rainfall events which trigger landslides from those which do not. The process of determining the rainfall threshold (R_T) involves varying a percentile threshold in the (joint) cumulative distribution to identify the corresponding rainfall intensity value. The R_T value is optimized, to improve its capability of distinguishing between the two groups, by ensuring that indexes such as the True Positive Rate (TPR), True Negative Rate (TNR), and Youden's Index are close to 1 (see Wu and Yeh, 2020). TPR is the ratio between the number of rainfall events which triggered a landslide and the number of rainfall events above the threshold ($n_{R;slide}/n_{R \geq R_T}$). TNR is the ratio between the number of rainfall events without a landslide and the number of rainfall events below the threshold ($n_{R;no\ slide}/n_{R < R_T}$).

As noted by Zhang *et al.* (2023), in cases where unbalanced rainfall-induced landslide datasets are prevalent, characterized by a notably higher number of non-landslide observations compared to landslide observations (a common scenario in many regions worldwide), one approach is to initially identify rainfall thresholds based on non-triggering events. Then, as more information on landslide occurrences becomes available, the analysis can include methods that consider triggering events. This allows for the refinement and enhancement of the previously identified thresholds.

Rainfall-dependent probability of a landslide

The probability of occurrence of a landslide within a pixel can be expressed based on conditional landslide intensity given rainfall intensity as follows, in equations (6) and (7):

$$P(L) = P(L|R \geq R_T) \cdot P(R \geq R_T) + P(L|R < R_T) \cdot P(R < R_T) \qquad (6)$$

$$P(L) = P(L|R \geq R_T) \cdot P(R \geq R_T) + P(L|R < R_T) \cdot (1 - P(R \geq R_T)) \qquad (7)$$

This equation uses a single threshold (R_T) to divide the rainfall events. Multiple thresholds may be used to further discretize the rainfall events.

For a value of the rainfall threshold, the relation between LR and LSI can be conditioned on the rainfall intensity, using only landslide events where $R \geq R_T$ and when $R < R_T$, respectively: $LR(LSI|R \geq R_T)$ and $LR(LSI|R < R_T)$. In each pixel that belongs to a specific rainfall cell, the number of rainfall events above and below the threshold are counted, respectively $n_{R \geq R_T}$ and $n_{R < R_T}$, using data of the corresponding rainfall cell. Finally, the conditional probabilities may be approximated in each pixel as (equations (8) and (9)):

$$P(L|R \geq R_T) \approx \frac{LR(LSI|R \geq R_T)}{n_{R \geq R_T}} \qquad (8)$$

$$P(L|R < R_T) \approx \frac{LR(LSI|R < R_T)}{n_{R < R_T}} \qquad (9)$$

The probability of exceedance of the rainfall threshold $P(R \geq R_T)$ can be computed, for each pixel, for the current and future climate. The corresponding landslide probability $P(L)$ will be then computed using equation (9).

3.2   Multivariate events

The following methodology outlines the procedure employed to estimate multi-hazard intensity for multivariate events. The analysis adopts a bivariate hazard assessment approach, in line with several existing studies (Latif, *et al.*, 2020; Ghanbari *et al.*, 2021; Bateni, *et al.*, 2022). Such approach is useful in estimating joint probability of multiple co-occurring hazards, enabling understanding of their complex interactions. The approach involves the following steps:

- Selecting pairs of extreme events for bivariate analysis;
- Quantifying the joint return period of the selected extreme events; and
- Defining scenarios of multivariate events and deriving associated hazard maps.

Figure 3.1.2 illustrates a graphical representation of the method. While this report focuses on two hazards (hazard pairs), a similar approach can be applied to three (hazard triples) or more hazards (hazard multiples).

****************************   ****************************

The process may yield various joint extreme events, their Joint Return Periods (JRP), scenarios of joint extreme events, and associated hazard maps. As this study does not aim to establish numerical hazard models, hazard maps related to different JRP scenarios are obtained from an existing database. Nevertheless, the methodology is adaptable to incorporate numerical modelling within the framework of multivariate events. The hazard maps depict the spatial distribution of multivariate event intensities, serving as input for impact and risk analysis in WP3 of MEDiate project.
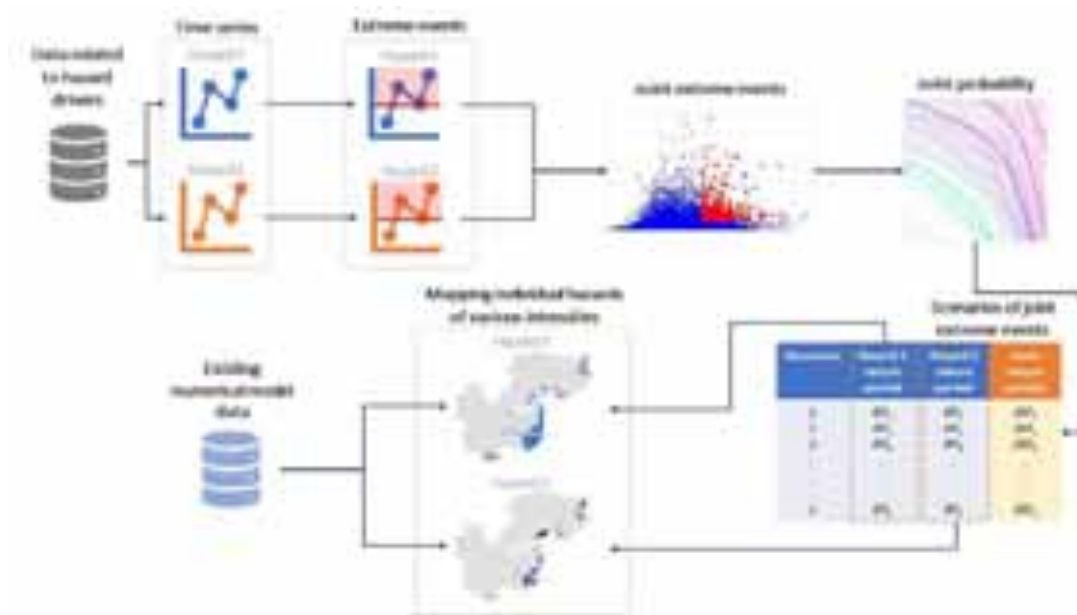
Figure 3.2.1 Conceptual framework for analysing multivariate events.

Identifying joint extreme events

The bivariate analysis requires the identification of appropriate time series data for hazard drivers (i.e., hazard 1 and hazard 2). In multivariate events, multiple hazards coincide within the same geographical region (Zscheischler *et al*., 2020). Therefore, data selection should be guided by the type of measurements, temporal scale of the data, and the spatial proximity of the two datasets. The chosen data should have long and overlapping time series (e.g., at least 30 years of data). For each driver, the data undergo cleaning to remove spikes or other problems, resampling to the same temporal resolution (e.g., hourly, daily, weekly), and consideration only of the overlapping period. Subsequently, the maximum values are estimated for each hazard driver.

The identification of extreme events employs the threshold-excess method, a statistical approach commonly used to analyse extreme values. Additionally, this method facilitates the detection of multiple events per year (Zheng *et al*., 2014; Ghanbari *et al*., 2019; Ghanbari *et al*., 2021). Quantile regression analysis is utilised to establish the relationship between time and maximum values within a specified timeframe and define the threshold (μ) for each hazard. The threshold must be sufficiently high to be deemed extreme and low enough to provide enough data for bivariate analysis (Ming *et al*., 2022). The threshold to determine joint extreme events is determined based on Kendall's rank correlation coefficient (τ), which assesses the correlation between random variables. A higher correlation values indicates a stronger dependency between two hazards in the specified time window (Figure 3.1.2). Values above the threshold are classified as extreme events for the respective driver. Depending on the driver's nature, a POT analysis may be necessary to select a single value for each event and to ensure independent events. Generally, it is assumed that exceedances should be at least 3–7 days apart but the specific length of this window is evaluated case by case based on the phenomenon

under study. According to the Pickands-Balkema-De Haan theorem (Balkema and Haan, 1974; Pickands, 1975), the data of each hazard driver are expected to be well-approximated by the Generalized Pareto Distribution (GPD) characterised by location (μ), scale (σ), and shape parameters (ξ), where the location parameter equals the threshold (Park and Kim, 2016).

After identifying extreme events for each individual hazard, compound events are selected. The combined hazard layout is considered, referring to the probability of exceedances of two hazard drivers over their respective thresholds, simultaneously or in close succession (Salvadori *et al.*, 2016). To define compound events, a temporal window around each hazard is considered. The length of this window (usually 3–7 days) is evaluated based on the specific phenomenon and Kendall's coefficient. Given the occurrence of an extreme event for hazard 1, if at least one extreme event for hazard 2 is found inside the search window, the two events regarded to be co-occurring. Only the maximum values of each driver inside the window are considered for subsequent analysis (Figure 3.1.2). It is important to note that when using this procedure, the time lag between two related events is not constant.

The process for identifying joint extreme events has been implemented in MATLAB (MathWorks®), and the outputs consist of time series data for each driver, showcasing joint extreme events and their respective thresholds.

Estimating joint probability from identified extreme events.

Once we have identified the joint extreme events, we need to estimate their Marginal Return Periods (MRPs) and JRP. The MRP, in days or years, for a hazard driver d, is given by equation (10).

$$MRP(d) = \frac{\lambda_d}{P_{mex}(d)} \qquad (10)$$

where $MRP(d)$ is the MRP as a function of driver value d, λ_d is the mean interval between successive extreme events in days or years for driver d, and $P_{mex}(d)$ is the marginal exceedance probability function, which gives the probability of the driver exceeding a given value d. This is simply one minus the marginal cumulative distribution function, $P_m(d)$, as shown in equation (11)

$$P_{mex}(d) = 1 - P_m(d) \qquad (11)$$

where $P_m(d)$ is the cumulative distribution function for driver d. As stated in the previous section, extreme events chosen by threshold can be expected to be distributed by the generalised pareto distribution, so $P_m(d)$ is given by equation (12)

$$P_m(d|\mu_d, \sigma_d, \xi_d) = \begin{cases} 1 - \left[1 + \xi_d \left(\frac{d - \mu_d}{\sigma_d}\right)\right]^{-\frac{1}{\xi_d}}, & \xi_d \neq 0 \\ 1 - \exp\left(-\frac{d - \mu_d}{\sigma_d}\right), & \xi_d = 0 \end{cases} \qquad (12)$$

where μ_d, σ_d, ξ_d are the location, scale and shape parameters for the distribution for driver d, respectively.

The JRP, in days or years, is calculated in a similar fashion to the MRP. The JRP for two drivers, $d1$ and $d2$, is given by equation (13):

$$JRP(d1, d2) = \frac{\lambda_j \lambda}{P_{jexex_j}(d1,d2)} \qquad (13)$$

*************************************   *************************************

where $JRP(d1, d2)$ is the JRP as a function of values of the two drivers $d1$ and $d2$, λ_j is the mean interval between successive joint extreme events and P_{jex} is the joint exceedance probability function, that gives the probability of two drivers exceeding values $d1$ and $d2$, respectively. P_{jex} is given by equation (14):

$$P_{jex}(d1, d2) = 1 - P_m(d1) - P_m(d2) + P_j(d1, d2) \quad (14)$$

where $P_m(d1)$ and $P_m(d2)$ are the cumulative distribution functions for the generalised pareto distributions of drivers $d1$ and $d2$ respectively, as given before in equation (12). $P_j(d1, d2)$ is the joint cumulative probability function for both drivers (i.e. the probability of an extreme event with values below $d1$ and $d2$ for both drivers). Based on Sklar's theorem, any joint distribution can be described in terms of its marginal distributions and a function known as a copula that accounts for any correlation (Sklar, 1973). Here we have chosen to use the extreme value Gumbel copula (Gudendorf and Segers, 2010), because, as noted by Xi *et al.* (2023), paired hazards such as surge and rainfall have been found to be particularly correlated in the tails (e.g., Gori *et al.*, 2022), and the Gumbel copula, allowing any upper tail dependency, is frequently used to quantify this kind of tail dependency (e.g., Ismael et al 2018 for bivariate datasets relating to floods). It also has the advantage of being an Archimedean copula and is thus easy to implement, both for calculating probability densities and cumulative probabilities as well as generating random samples for posterior probabilistic checks. The function $P_j(d1, d2)$ is given by equation (15) for the Gumbel copula:

$$P_j(d1, d2) = exp\left\{-\left[(-\log(P_m(d1)))^\theta + (-\log(P_m(d2)))^\theta\right]^{1/\theta}\right\} \quad (15)$$

where θ is the Gumbel copula parameter that specifies the correlation, taking values from 1 to ∞.

The MRPs and JRP for a pair of driver values are thus a function of the model parameters $\mu_1, \sigma_1, \xi_1, \mu_2, \sigma_2, \xi_2$ and θ, i.e., the location, shape and scale parameters of the two marginal generalised pareto distributions and the copula parameter. The location parameters are fixed by the thresholding procedure, so we have a five-dimensional parameter space for our model, consisting of $\sigma_1, \xi_1, \sigma_2, \xi_2, \theta$. We adopt a Bayesian approach to infer the posterior distribution over this parameter space and as a consequence, the posterior distribution over MRP and JRP also. The advantage of this Bayesian approach is that once we have inferred the posterior distribution over the parameter space it is trivial to infer the posterior distribution over any values derived from the parameters like MRP and JRP and to investigate the probabilistic relationships between them. We start by assigning uniform priors over the permitted ranges of our model parameters (equations 16 to 20)

$$\sigma_1 \sim uniform(0, \infty) \quad (16)$$

$$\sigma_2 \sim uniform(0, \infty) \quad (17)$$

$$\xi_1 \sim uniform(-\sigma_1/(d1_{max} - \mu_1), \infty) \quad (18)$$

$$\xi_2 \sim uniform(-\sigma_2/(d2_{max} - \mu_2), \infty) \quad (19)$$

$$\theta \sim uniform(1, \infty) \quad (20)$$

where we use the operator $\sim$ to indicate *is distributed as*, $uniform(min, max)$ to indicate a uniform probability distribution between values min and max, and $d1_{max}$ and $d2_{max}$ are the maximum extreme values of the two drivers, respectively. We then introduce our data in the form of the likelihood, equation (21):

$$(d1, d2) \sim gumbel\{GPD(\mu_1, \sigma_1, \xi_1), GPD(\mu_2, \sigma_2, \xi_2)\} * gpd(\mu_1, \sigma_1, \xi_1) * gpd(\mu_2, \sigma_2, \xi_2) \qquad (21)$$

where $(d1, d2)$ are a pair of extreme values for drivers $d1$ and $d2$, $gumbel(u, v)$ denotes the probability density function of the Gumbel copula for a point (u, v), and $gpd(\mu, \sigma, \xi)$ and $GPD(\mu, \sigma, \xi)$ are the probability density function and cumulative probability function for the generalised pareto distribution, respectively.

We implemented this model in the Bayesian probabilistic programming language Stan (Carpenter et al. 2017). We used the Stan language implementations of the Generalized Pareto Distribution of Aki Vehtari (Vehtari, A., 2017) except for the inverse cumulative distribution function / quantile function / ppf which we implemented based on (Zaiontz, 2020). For the Gumbel copula pdf we used Ben Goodrich's Stan implementation (Goodrich 2017), while the cdf was based on (Nelson, 2006). For random draws from the Gumbel copula for posterior predictive checks we implemented in Stan the procedure outlined in Nelson (2006) and Genest and Rivest (1993). Stan uses the Hamiltonian Monte Carlo method with the No U-Turn Sampler (NUTS) to approximate probability distributions. Some diagnostic tests should be carried out to assess the goodness of the analysis and then, for each event, the posterior distributions over the return period can be computed.

To check that the Hamiltonian Monte Carlo simulation is adequately sampling the density distribution, certain criteria must be met (Stan Development Team, 2024). Among them, the potential scale reduction factor $\hat{R}$ can be used, and it is considered good practice to ensure values are below 1.05, the closer to 1.0 the better. The chains of successive samples from the posterior, drawn with the Hamiltonian Monte Carlo procedure, should also be checked for autocorrelation, which reduces the accuracy of the parameter estimates for a given chain length. This is measured by the Effective Sample Size. Additionally, it is also possible to check for divergences, which occur when the posterior distribution is too tightly curved for Hamiltonian Monte Carlo to sample properly.

To check how well the marginal GPD fits the data, we use Bayesian Quantile-Quantile plots that compare empirical quantiles with those calculated from the distribution. Every sample in the chains gives us a single value of the scale and shape parameters for both distributions, which can be used to calculate quantiles. Thus, we get one Quantile-Quantile curve for each sample, and the posterior distribution defines a distribution over Quantile-Quantile curves. A perfect fit would be indicated by the curves lying along the 1:1 relationship. The whole model can also be tested using Posterior Predictive Checks (PPCs) that compare the distribution of simulated observations with the original observations.

Mapping individual hazards of varying intensities

Each sample joint probability corresponds to a pair of extreme events (hazard-1 and hazard-2) with different intensities. By considering various combinations of intensities for hazard-1 and hazard-2, multiple scenarios of multivariate events can be generated. For instance, in the context of compound coastal and riverine flood events, scenarios may involve high-surge and low-flow events, represented by return periods of surge and river flow. For each scenario, it is possible to calculate the posterior distributions over the JRP and the marginal RPs. The associated values for each marginal RP of individual hazard drivers are known. Ideally, numerical models should be employed to determine the intensity distribution of compound hazards. In each scenario, the values of the drivers, along with their associated RPs, can serve as input for the numerical model. The output consists of hazard intensity maps that will be utilised for impact analyses, when combined by exposure and

vulnerability models. In the absence of available numerical hazard modelling options within the project, this initiative links the RPs of individual hazards within a scenario to pre-computed hazard maps with the same RPs. These hazard maps facilitate the estimation of risk for multivariate events as part of the DSS.

3.3   Spatially compounding events

Spatially compounding events (SCE) occur "when multiple connected locations are affected by the same or different hazards within a limited time frame, thereby causing an impact" (Zscheischler *et al*., 2020). This study aims to quantify spatially compounding events based on pairs of two hazards. The methodology comprises three steps:

1. identifying joint extreme events;
2. quantifying the joint return periods of the extreme events identified; and
3. mapping individual hazards of various intensities.

Figure 3.3.1 presents a generalised framework for estimating probabilities and mapping SCEs. The framework can be applied to analyse SCEs in both baseline and future climate change scenarios. The framework helps to understand the pattern of changes in the frequencies of joint extreme events, indicated by JRP, for various combinations (scenarios) of exceedance probabilities (i.e., RPs) of individual hazards. The maps of individual hazards for various RPs are generated, corresponding to different scenarios.

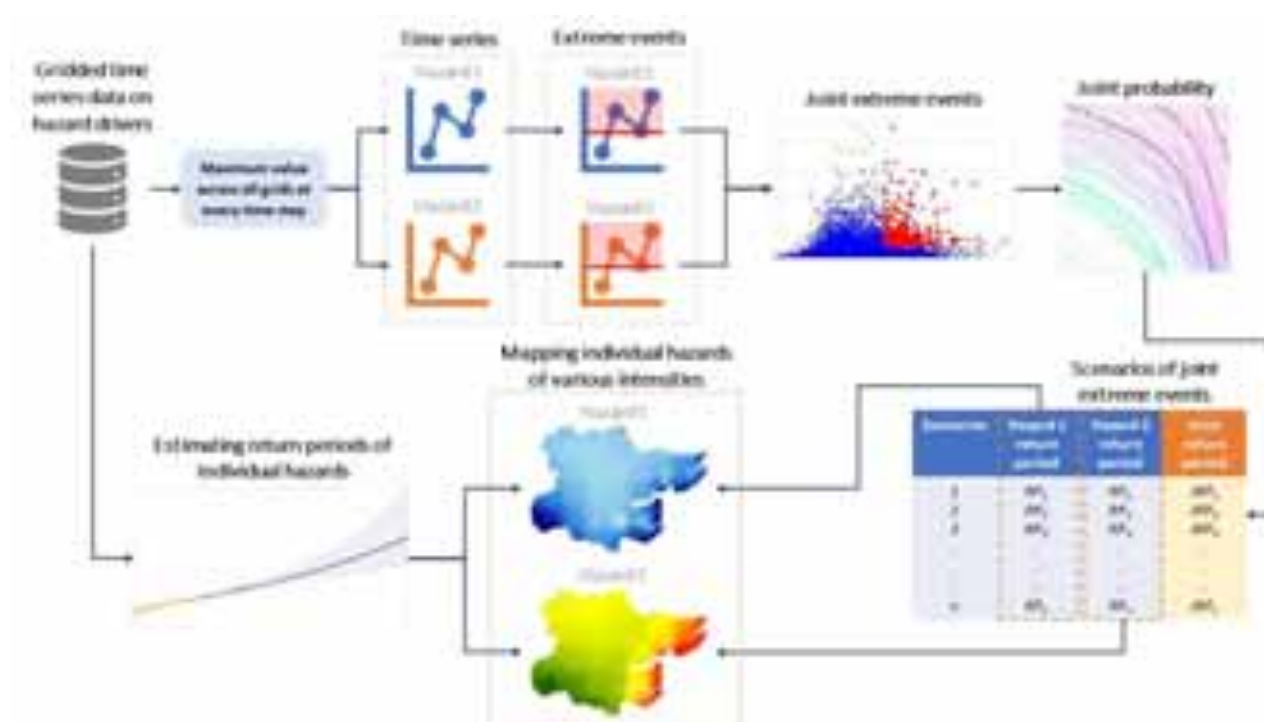Figure 3.3.1 Framework for analysing spatially compounding events.

Identifying joint extreme events

The identification of joint extreme SCEs relies on gridded time series data of hazard drivers. This process hypothesises that SCE occur when multiple hazards impact the same or different locations within specified boundary conditions and timeframes. At each time step (e.g., hourly, daily, weekly), the maximum values of

two hazard intensity measures are determined across all grids within the study area. This yields two time series datasets for hazard 1 and hazard 2. Subsequently, after preparing the two time series datasets, joint extreme events are identified using the methodology outlined in section 3.2.

Estimating joint probability from selected extreme events

Joint extreme events, identified in the previous step, are included as input data for estimating JRPs of SCEs. Again, a copula-based approach is followed. The detailed methodology for estimating JRP is described in section 3.2. After estimating JRPs, different scenarios of SCEs are generated, based on various combinations of individual hazard intensities based on the RPs. In compliance with those scenarios, the spatial distribution of individual hazards is evaluated.

Mapping individual hazards of various intensities

To assess the severity of spatially compounded multi-hazard events, maps depicting individual hazard indicators with varying RPs are generated. Extreme value analysis is performed at each grid cell using the L-moment method to fit a GEV distribution (Coles, 2001; Gilleland and Katz, 2016), using the equation (1). The return period (RP) for single hazards is estimated by following formula (22):

$$RP = \frac{1}{1 - G(z)} \qquad (22)$$

3.4 Temporally compounding events

Temporally Compounding Events (TCE) are a succession of hazards that affect a given geographical region, leading to or amplifying an impact when compared to a single hazard (Zscheischler *et al*., 2020). Climate extremes in the same location and extreme multivariate climate anomalies that are not essentially extreme in the contributing variables are part of TCE (Liu *et al*., 2016; Tilloy *et al*., 2019; Zscheischler *et al*., 2020). This study aims to quantify TCE based on pairs of two hazards. The methodology comprises the following steps:

- identifying hazard-1 and hazard-2 events;
- calculating the compound co-occurrence of the two hazards; and
- mapping the individual hazards (hazard-1 and hazard-2) and the resulting compound events.

Figure 3.4.1 presents a generalized framework for estimating frequency and mapping TCE. The framework can be applied to analyse TCE in both baseline and future climate change scenarios. The framework helps to understand the pattern of changes in the frequencies of compound extreme events.
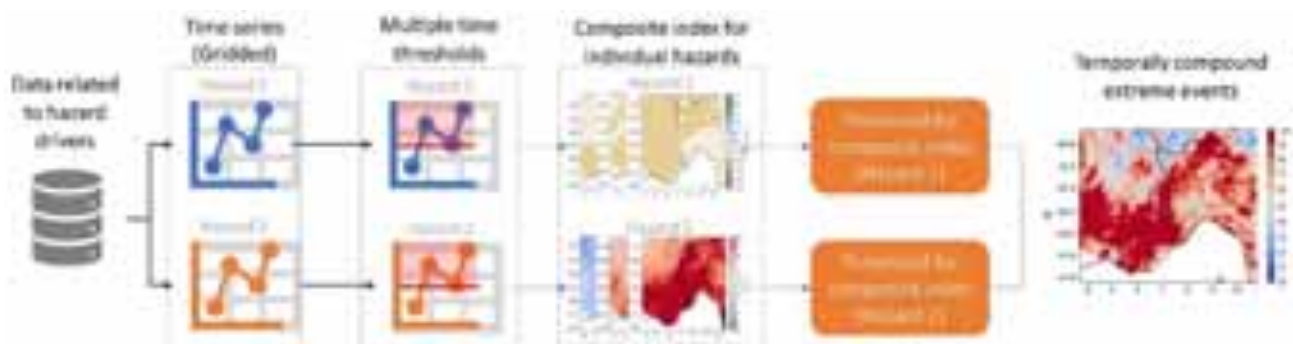

Figure 3.4.1 Framework for estimating frequency of temporally compounding events.

Identifying individual hazard events

The present analysis first identifies hazard-1 and hazard-2 events individually, adopting specific composite indices, based on standardised indicators or percentiles. It is noteworthy that for TCEs, multiple time thresholds must be applied to compute the composite index. For instance, if the 90th percentile of daily temperatures persists for three consecutive days, such occurrences can be termed as heatwave events. The identification of these events can be done initially on a daily basis and subsequently by utilizing a monthly standardised index. Currently, a variety of indices with different temporal scales are available to identify events, depending on the specific requirements of the study or the sector under consideration. For instance, in the case of extreme heat and drought events, a heatwave event can be defined at the monthly scale when monthly standardized Heat Wave Index exceeds a threshold, while drought events can be investigated by using the canonical thresholds of a 3-month Standardised Precipitation Index (SPI).

Compound co-occurrence

The combined hazard events (COH1H2) are categorized on a monthly basis provided that both individual hazards occur within the specified monthly timeframe. COH1H2 occurrences are identified spatially at the grid point level within a domain encompassing the analysed area during historical and future periods. This information is stored in matrices for each year within the analysed time slices. It is important to note that the timescale for hazard co-occurrence varies in relation to the type of hazard in question; for instance, the onset of a drought requires weeks of unusually dry weather conditions.

Mapping hazard

The data regarding individual and temporally compounding events are summarised through the mapping of individual (hazard-1 and hazard-2) and composite (COH1H2) indicators across various time slices within the domain. Initially, information pertaining to hazard-1 and hazard-2 months is presented individually. Subsequently, the frequency of COH1H2 occurrence is provided at the seasonal scale, i.e., the fraction of COH1H2 months out of the months analysed.

4 MULTI-HAZARD EVENTS IN FOUR TESTBED REGIONS

The methods outlined in section 3 are employed to analyse 12 pairs of multi-hazard events across four testbed regions—Oslo, Nice, Essex, and Múlaþing—as listed in Table 2.1.2. This section delineates the attributes of multi-hazard events in the four testbed regions, and it provides a concise summary of the analytical outcomes.

4.1 Oslo testbed: summary of multi-hazard event analysis

In Oslo, among the identified pairs of multi-hazard events, compound coastal and riverine flood events emerge as one of the most frequently occurring hazards, inflicting detrimental effects on populations and assets. Through the analysis of time series data on surge and river flow, we identify 20 compound flood events in the baseline scenario (1979–2005), a number projected to increase to 27 in the future (2024–2050) (Table 4.1.1). A comparison of flood inundation maps between baseline and future scenarios reveals an anticipated increase in both depth and extent in the future. Notably, the probable extent of inundation during riverine flooding is significantly larger than that of coastal flooding. Areas near the coastal region are more susceptible to both riverine and coastal flooding compared to inland areas. A comprehensive description of this multi-hazard event is presented in Section 5.1.

Table 4.1.1 Summary of three categories of multi-hazard events analysed in Oslo.

Multi-hazard pairs	Indicators	Multi-hazard type	Hazard indicators	Threshold (percentile)		Number of joint extreme events	
				Baseline	Future	Baseline	Future
Compound coastal and riverine flood events	Surge and river flow	Multi-variate	Weekly average surge height (m)	90th	90th	20	27
			Weekly average river flow (m^3/s)	90th	90th		
Flood and landslide	Observed rainfall triggered riverine floods	Triggering	1-day daily precipitation (mm)	95th	-	123	-
			Daily average river flow (m^3/s)	95th	-		
			5-days daily precipitation (mm)	95th	-	225	-
			Daily average river flow (m^3/s s)	95th	-		
	Baseline and future rainfall triggered riverine floods	Triggering	1-day daily precipitation (mm)	85th	95th	14	15
			Weekly average river flow (m^3/s)	95th	90th		
	Baseline and future rainfall triggered riverine floods	Triggering	5-day daily precipitation (mm)	85th	95th	18	28
			Weekly average river flow (m^3/s)	97th	85th		
Flood and quick clay	Preconditioned baseline and future rainfall triggered riverine floods	Preconditioned and triggering	5-day daily precipitation (mm)	90th	-	49	-
			Weekly average river flow (m^3/s)	90th	-		
	Preconditioned baseline and future rainfall triggered riverine floods	Preconditioned and triggering	5-day daily precipitation (mm)	75th	90th	4*	15
			Weekly average river flow (m^3/s)	85th	85th		

*Time series overlapping of baseline data is limiting

In this report, the focus has been on debris landslides registered in the NVE database, nevertheless rockfall was also included as is it can be an indicator of erosion cause by extreme rainfall. These landslides are categorized by specific codes: 111 (rockfall), 140 (unspecified), 142 (debris flow) and 144 (debris avalanche). The inventory database includes 22 landslides in the Oslo region for the period studied in this report, 12 of them occurred during summer or autumn (Table A1.1 in Appendix). Joint extreme events were defined using recorded rainfall at SN18700 station and discharge at Gryta station (Figure 1.2.1). Gryta Station was selected due to the availability of a long timeseries and uncontrolled discharge. The Gryta river is thought to be representative of natural response and therefore descriptive of possible erosion in small streams in the area.

Extreme events of 1- and 5-day precipitation from SN188700 was used and extreme rainfall events treated as a trigger for extreme events of discharge in Gryta. The method was described in section 3.1 (Trigger-Driven Joint Extremes). Landslide events were linked to selected extreme events to estimate the effect of the method (Figure A1.6 in Appendix A1).

Rainfall data was projected by multiplying the estimated increase in precipitation. This method is expected to have significant effects on the statistics. This assumption means that every 36 years the same weather pattern repeats but with estimated percental increase from climate reanalyses (KSS, 2024), providing loss of natural variability and false trends. However, using this method makes the link to the point location more precise and since this project does not have the scope to make statistical analysis on the data series and the effect of different climate data models on point locations, this was considered an acceptable approach.

The precondition for quick clay landslides was defined above as an increased likelihood of events expected after a wet summer. The area where the analysis focuses on is the Alna region in Oslo (Figure 4.1.1). Measurements have been made at the Alna River at Kvernebyen since 2019. The Alna River is controlled and therefore not likely to respond naturally to precipitation events.
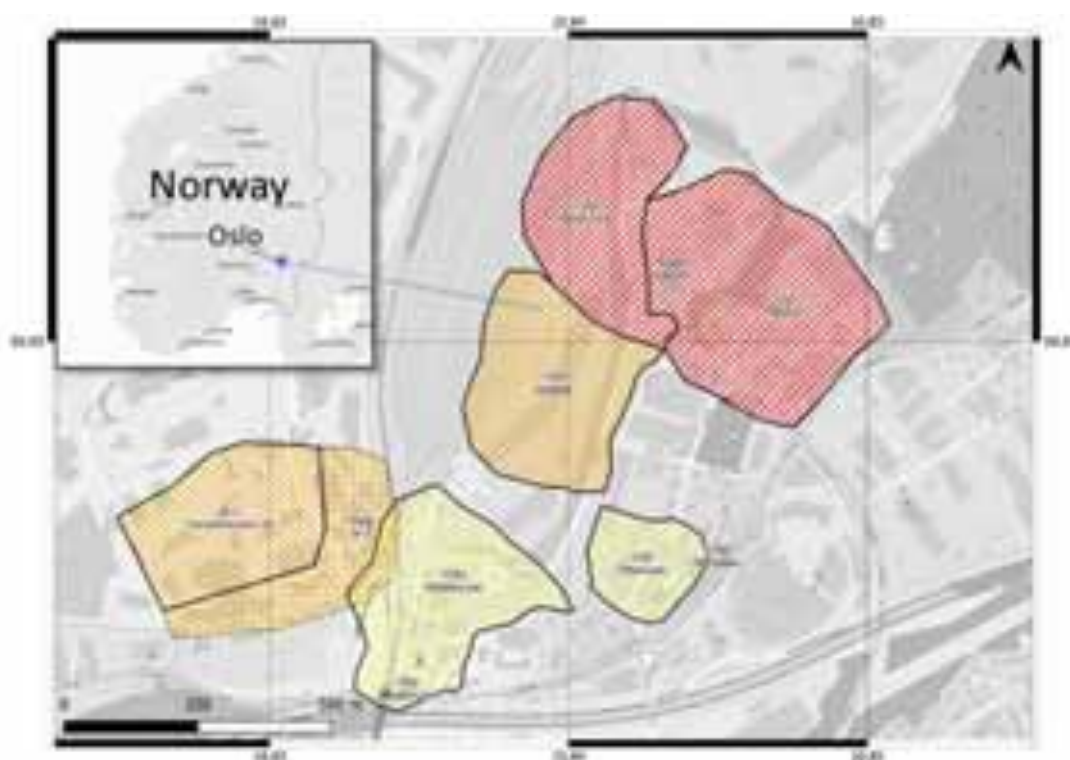
Figure 4.1.1 Quick clay hazard in the Alna region of Oslo showing that the area is subjected to moderate-to-high risk. The colours refer to severity of the hazard, yellow being the least severe (low) and red the most severe (high) (NVE, 2024).

The same approach was used to define the extreme events as for the landslide and floods hazard pair, except that for the analysis of flood and quick clay extreme summer precipitation a 75th percentile threshold was used. The dataset was filtered so that only years with summer rain (Figure 4.1.2) above the threshold were joint with the discharge data (Figure A1.8 in Appendix A1).

The results from the joint extreme analyses were not realistic for the baseline since the overlapping of the baseline discharge data and the filtered rainfall was only one year. However, the future scenario of extreme precipitation and discharge, where extreme summers have been filtered out, shows that when looking at a RP of 50 years for single hazard the JRP is more than 200 years (Figure A1.9 in Appendix A1).
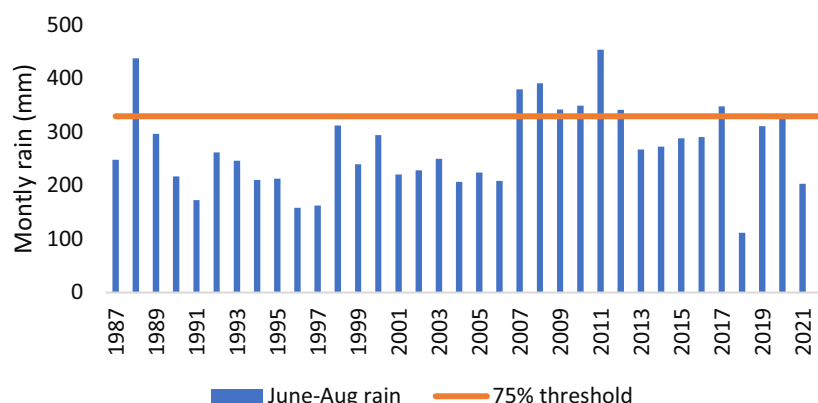
Figure 4.1.2 Summer rain with a 75% threshold serving as a precondition to quick clay hazard.

4.2   Nice testbed: summary of multi-hazard event analysis

Through the PAR process under the MEDiate project, three pairs of multi-hazard events are identified in Nice. The multi-hazard events include: (1) compound coastal and riverine flood, (2) flood and landslide, and (3) extreme heat and drought events. Notably, these three pairs correspond to three categories of multi-hazard events: multivariate, triggering, and temporally compounding types. The methodologies to analyse the interactions of these multi-hazard events are explained in section 3.

Compound coastal and riverine flood events
By analysing time series of surge and river flow, we identify 17 compound flood events in the baseline scenario (1979–2005). For the future scenario (2024–2050), the number of events is found to be 14 (Table 4.2.1). The results indicate that while the joint probability of co-occurring surge and river flow could be lower in the future, their intensities would be higher (Figure A2.4 in the appendix). A comparison of coastal and riverine flood inundation maps reveals that the probable extent of inundation during riverine flooding is significantly larger than that of coastal flooding. Particularly, areas adjacent to the confluence of the Var River and the Mediterranean Sea are prone to both coastal and riverine flood inundations (Figure 4.2.1).

Table 4.2.1 An overview of compound coastal and riverine events identified in Nice.

Multi-hazard pairs	Multi-hazard type	Hazard indicators	Threshold (percentile)		Number of joint extreme events	
			Baseline	Future	Baseline	Future
Compound coastal and riverine flood events	Multivariate	Weekly average surge height (m)	95th	90th	17	14
		Weekly average river flow (m³/s)	85th	90th		

Figure 4.2.1 Spatial distribution of coastal and riverine flood prone areas in Nice for a 50-year event.

Flood and landslide

Throughout this project, the available landslide inventory (accessible at https://infoterre.brgm.fr/) comprises 1476 events spanning from as early as 1900 to 2020. These events are categorized into five groups: rockfalls (334 events), debris (34), collapse (29), erosion (38), and slides (1042). Many of these events consist of slides and debris, which were primarily utilized to establish the rainfall-induced landslide hazard, as other events might not be directly triggered by rainfall (e.g., rock falls). It was observed that the available database is not complete, as these events are predominantly situated along main roads and within municipalities, and it does not include events in remote mountain areas. For this reason, the landslide susceptibility map was calculated focusing only on the area along main roads, utilizing a constant buffer around them.

In the figure below (**Error! Reference source not found.**), the landslide susceptibility map derived using several pre-conditioning factors (proximity to rivers, DEM, slope, aspect, lithology, and land cover) and the landslide database, employing the Random Forest method (Breiman, 2001). The black dots represent the landslide events in the database.

The susceptibility map reveals that a significant portion of the area falls within the medium to high susceptibility classes, underlining the significance of the hazard.
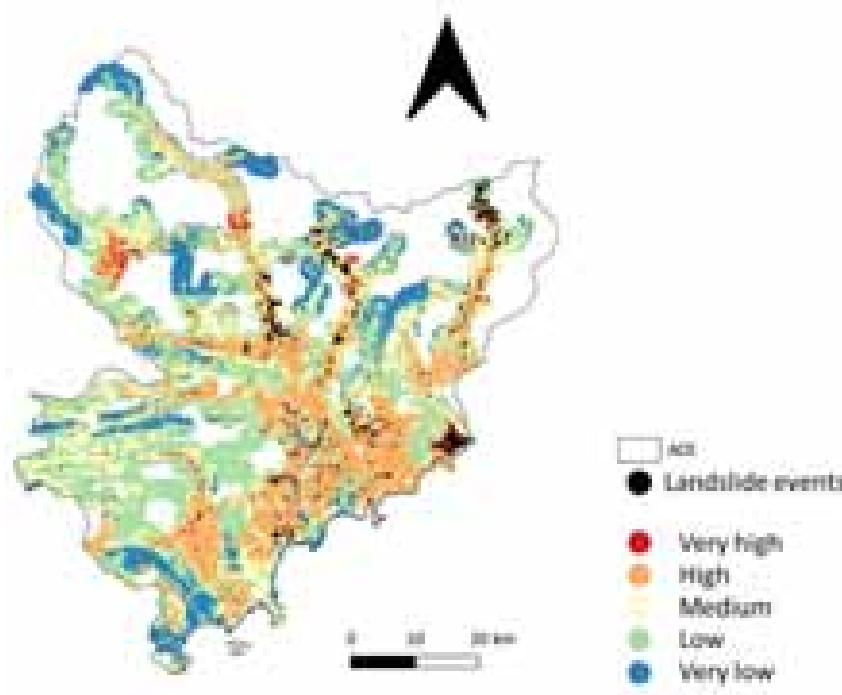
Figure 4.2.2 Susceptibility map for the wider area of Nice.

Climate change impact on rainfall

The landslide rainfall trigger threshold was derived from the maximum intensity and duration of an event during the five days preceding a landslide. The best approximation of this quantity available from the Copernicus Climate Datastore (CDS) (Berg *et al*., 2021) is the future change in the highest 5-day rainfall amounts. If, in the future, maximum 5-day rainfall amounts increase, landslide occurrence will likely also increase, i.e., the threshold will be exceeded more often.

The projected changes available from the CDS are calculated from an ensemble of eight EURO-CORDEX regional climate models, that have been bias-corrected and down-scaled to 5 kilometers using the EFAS-Meteo reference dataset (Ntegeka *et al*., 2013), following a quantile mapping approach (Figure 4.2.3). The current analysis focuses on the far future time-horizon (2071–2100) and the moderate (RCP4.5) and extreme (RCP8.5) climate scenario for Nice (Figure 4.2.4).
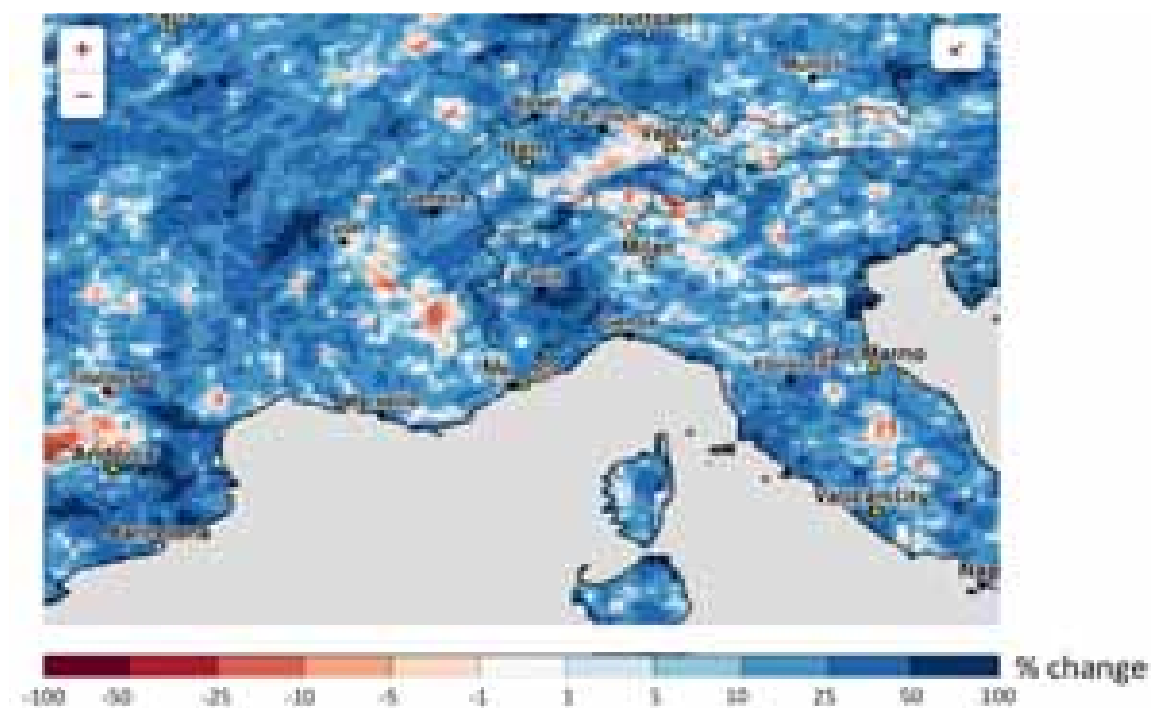
Figure 4.2.3 Projected change (%) in highest five-day rainfall amounts for 2071 – 2100 for RCP8.5. Source: CDS.
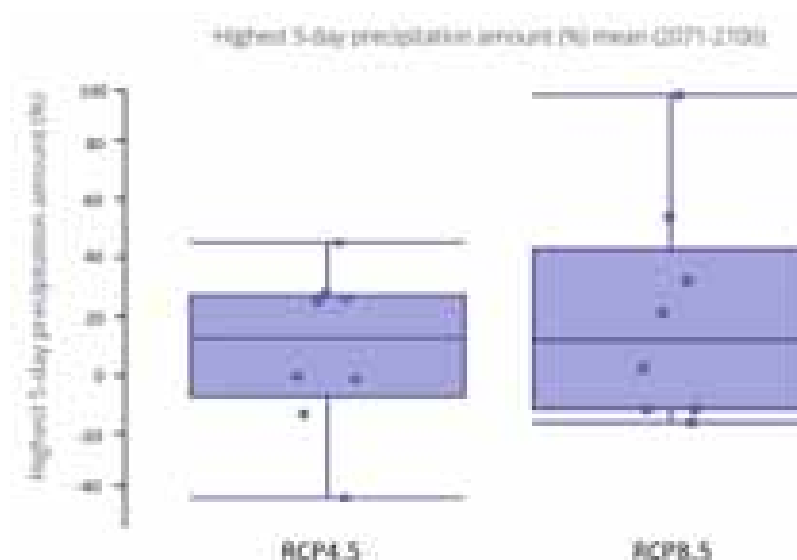
Figure 4.2.4 Projected change (%) in highest five-day rainfall amounts for Nice for 2071 – 2100 for RCP4.5 (left) and RCP8.5 (right). Source: CDS.

According to the projections from RCP4.5, changes in 5-day precipitation amounts will vary approximately between -40% and +40%. Looking at the most extreme scenario (RCP8.5), most models predict an increase in the highest 5-day precipitation amounts (Figure 4.2.4). The 25 to 75% range of the projections indicate changes between -10% and + 45%. The median change for both scenarios is ~+ 10%, providing an indication that also the precipitation threshold will be exceeded more often in the future.

4.3   Essex testbed: summary of multi-hazard event analysis

In Essex, three pairs of multi-hazard events encompass both multivariate and spatially compounding categories of multi-hazard events. Section 3 elaborates on the methodology used to quantify interactions between different types of multi-hazard pairs. Table 4.3.1 provides an overview of these multi-hazard pairs, including their intensity measures, the thresholds used for identification, and the number of events identified for both baseline and future climate change scenarios. The analysis reveals that the minimum threshold limit for each hazard indicator varies based on the multi-hazard category and the timeframe (i.e., baseline and future) for analysis. Results suggest that the occurrence rates of spatially compounding events such as extreme wind and rainfall are likely to increase in the future. Figure 4.3.1 compares the spatial distribution of 50-year wind, temperature, and rainfall intensities in Essex between the baseline and future scenarios, indicating a general increase in hazard intensities in the future.

Table 4.3.1 Summary of three categories of multi-hazard events analysed in Essex.

Multi-hazard pairs	Multi-hazard type	Hazard indicators	Threshold (percentile)		Number of joint extreme events	
			Baseline	Future	Baseline	Future
Extreme wind and rainfall events	Spatially compounding	Daily maximum wind speed of gust at 10m (m/s)	97th	97th	46	115
		Daily precipitation (mm)	90th	85th		
Compound coastal and riverine flood events	Multivariate	Weekly average surge height (m)	85th	85th	42	23
		Weekly average river flow (m³/s)	85th	95th		
Extreme heat and rainfall events	Spatially compounding	Daily maximum temperature (°C)	95th	90th	24	43
		Daily precipitation (mm)	95th	97th		
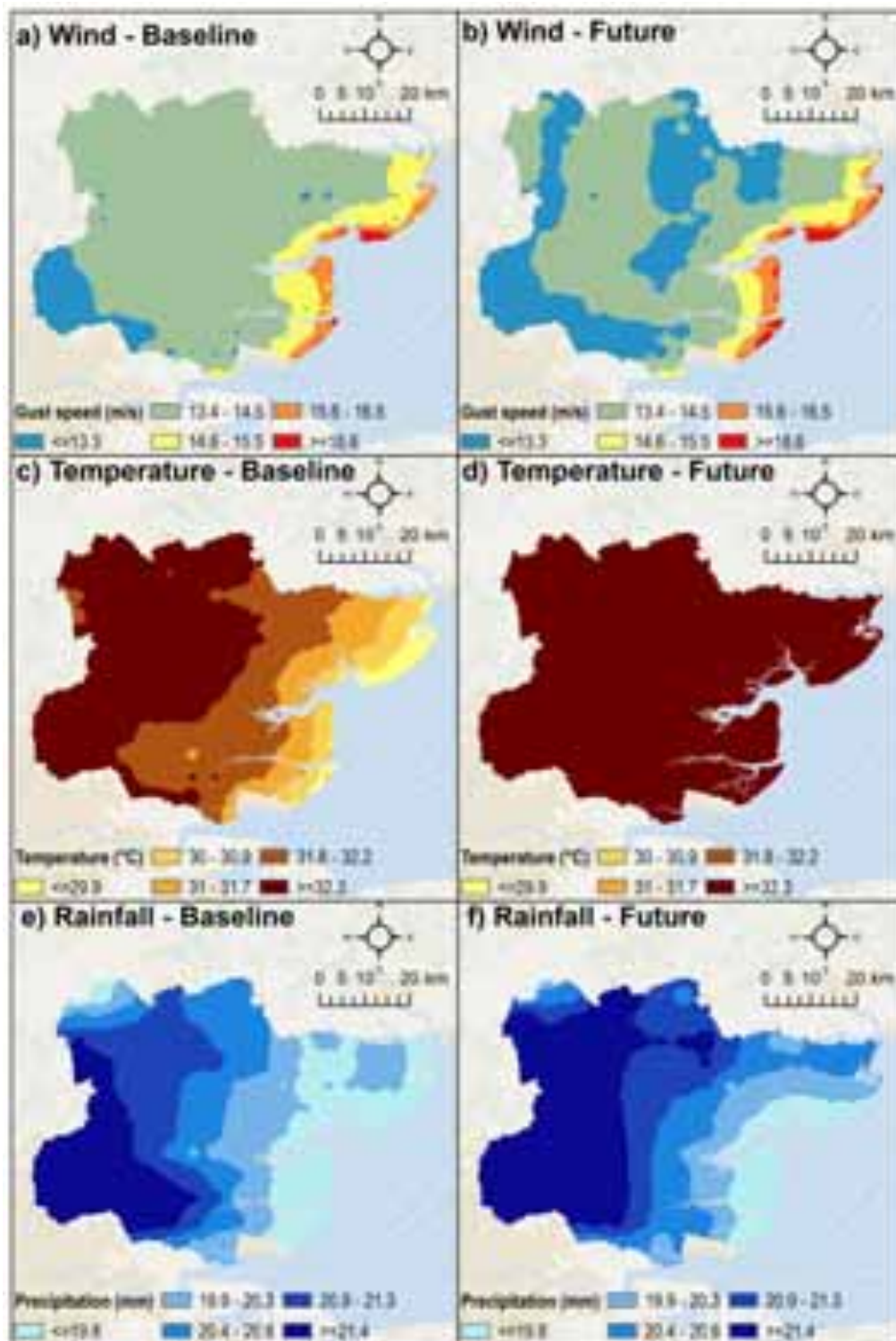
Figure 4.3.1 Spatially compounding multi-hazard indicators in Essex. This figure compares the spatial distribution of 100-year wind, temperature, and rainfall intensities between the baseline and future scenarios.

Regarding multivariate events, the number of compound coastal and riverine flood events is estimated to be lower under the future scenario compared to the baseline scenario. However, global flood hazard maps (Ward *et al*., 2020) used in this study indicate that both flood depth and extent are likely to increase in the future. Figure 4.3.2 presents a comparison of 100-year coastal and riverine flood inundation depth and extent in the

coastal districts of Essex between the baseline (1980) and future (2050) scenarios. Generally, these districts are prone to coastal flooding compared to riverine flooding, which may experience an increase in the highest depth for a 100-year event from 3.84m in the baseline scenario to 4.22m in the future. Similarly, the highest riverine flood inundation depth of 0.13m for a 100-year event is projected to increase to 0.16m in the future. Notably, the PAR process indicates that Essex County frequently experiences extreme wind and rainfall events. Therefore, the MEDiate project further explored the results of extreme wind and rainfall events, as detailed in Section 5.3.
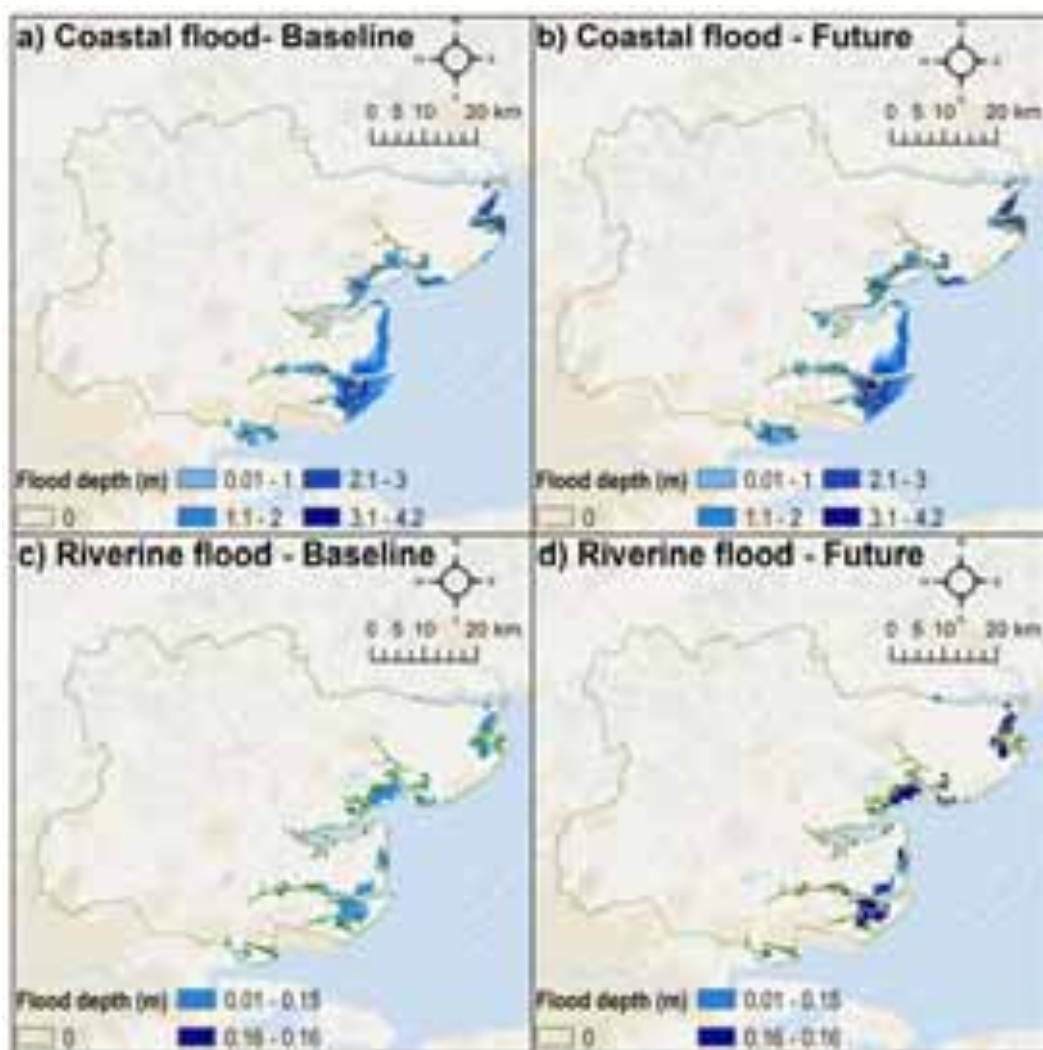
Figure 4.3.2 Multivariate events in the coastal districts of the Essex County. This figure compares the spatial distribution of 100-year coastal and riverine flood events between the baseline and future scenarios.

4.4 Múlaþing testbed: summary of multi-hazard event analysis

In Múlaþing, the three pairs of multi-hazard events, include triggered events and, preconditioned and triggered events. Section 3 provides detailed insight into the methodology employed to measure the interactions among various types of multi-hazard pairs. Table 4.4.1 provides an overview of the hazard indicators used, while

************************ ************************

Table 4.4.2 lists the multi-hazard pairs, the thresholds used for identification, and the number of events identified for both baseline and future climate change scenarios. The analysis reveals that the minimum threshold limit for each hazard indicator varies based on the multi-hazard category and the timeframe, i.e., historical (baseline) and future, for analysis.

The precipitation timeseries used in this part of the analysis is the ICRA atmospheric reanalysis project for Iceland, (Nawri *et al*., 2017) downscaled data from 1979 to 2017. More detailed discussion about the dataset is provided in section 5.4.1 but point data were extracted from the dataset, the process is described in Massad *et al*. (2020). The snow avalanche inventory database of Iceland also includes landslides. The temperature data used is station data from the IMO weather database. Precipitation was projected by multiplying daily precipitation by the estimated increase in precipitation for the next decade (Massad *et al*., 2023).

Melting in connection to extreme precipitation was analysed. Melting is not a direct output of the model used for the ICRA, but a combination of the rate of graupel (soft snow pellets) and snowfall, the sublimation rate, and the snow-water equivalent.

Table 4.4.1 Datasets used in the Múlaþing/Seyðisfjörður example.

Indicators	Dataset	Timeframe	Temporal resolution	Spatial resolution
Snow-avalanche and Landslide inventory	IMO database	Year 965 to present	Decades up to exact time of occurrence	1 km to 1 cm
Precipitation	ICRA	1 September 1979–2017	Reanalysis: hourly data converted to daily	2.5 km × 2.5 km
Snowmelt	ICRA	1 September 1979–2017	Reanalysis: hourly data converted to daily	2.5 km × 2.5 km
Projected precipitation	ICRA - projected	2020–2100	Daily data	2.5 km × 2.5 km
Temperature data	Station 620 IMO database	1938–	Daily	Point location
Projected Temperature data	Station 620 IMO database	2020–2100	Daily	Point location

Table 4.4.2 Summary of the categories of multi-hazard events analysed in Múlaþing/Seyðisfjörður.

Multi-hazard pairs	Hazard indicators	Multi-hazard type	Multi-hazard variables	Threshold (percentile)		Number of joint extreme events	
				Baseline	Future	Baseline	Future
Heavy rain and landslide	Rainfall intensity Antecedent precipitation	Multivariate - triggering	1d rain/sNAPI	90th	90th	54	184
				90th	85th		
			2d rain/sNAPI	99th	-	20	-
				90th	-		
			3d rain/sNAPI	99th	-	18	-
				90th	-		
			5d rain/sNAPI	90th	90th	46	71
				85th	90th		
Snow melt and flood	Rainfall intensity Snowmelt	Precondi-tioned - triggering	1d rain/Melt	95th	-	14	-
				95th	-		
			2d rain/Melt	95th	-	10	-
				95th	-		
			3d rain/Melt	95th	-	7	-
				95th	-		
Heavy snowfall and avalanche	Snowfall Antecedent precipitation	Multivariate-preconditioned - triggering	Snow/API	98th	90th	105	104

For hazard pair 1 "heavy rain and landslide" the rolling sum of 1,2,3 and 5 days rain were analysed against scaled and normalised API (sNAPI) to define the possible critical conditions for landslides to be triggered. Only the 1- and 5-days rolling sums of rainfall were then analysed with the projected rainfall to estimate the effect of climate change (Table 4.4.2). The results for these extreme events are discussed in detail in section 5.4.

For the second hazard pair "snow melt and flood" the hazard evaluation is based on the Hazard Assessments from 2002 and 2019 carried out by the Icelandic Meteorological Office (Arnalds *et al.*, 2002; Gylfadóttir *et al.*, 2019). Figure A4.3 in Appendix A4 shows the connection between selected extreme hazards and slush flow events. No slush flow is recorded during the selected extreme pairs or landslides registered in connection with snowmelt. This could have the simple explanation that slush flows generally occur very locally under very special preconditioned circumstances that have not been met in these cases. Also, the timing of the melt extreme might have to be defined differently to be able to connect them to the landslide / flood events. The joint extreme pairs show a better correlation between 1-day rainfall and snowmelt than for 2-day or 3-day rainfall.

For the category "heavy snowfall and avalanche" the inventory of IMO was analysed to find correlations between heavy precipitation and snow avalanche occurrence around Seyðisfjörður. New snow can act as additional loading on the existing snow layer and a lack of cohesion in the newly fallen snow can cause avalanches. Avalanches can occur immediately or up to a few days after the snow fall (EAWS, 2022). Figure A4.5 in Appendix A4 shows the connection between selected extreme hazards and snow avalanche events. The recorded avalanche events were defined as dry avalanches and the correlation between intensive snowfall and antecedent precipitation (snow) is good. Each year has limited datapoints due to the seasonal effect of the data (Figure A4.6).

********************************   ********************************

5   RESULTS FOR THE SELECTED MULTI-HAZARD PAIRS

Among the 12 pairs of multi-hazard events identified across four testbed regions, four hazard pairs are selected for thorough investigations, with the objective of contributing to the development of the DSS that the MEDiate project intends to deliver. Additionally, these selected four hazard pairs align with the four categories of multi-hazard events expounded in Section 3. The following are the four hazard pairs along with their corresponding multi-hazard type:

1. Oslo – Compound coastal and riverine flood events (Multivariate).
2. Nice – Extreme heat and drought events (Temporally compounding).
3. Essex – Extreme wind and rainfall events (Spatially compounding).
4. Múlaþing – Heavy rain and landslide events (Preconditioned and triggering).

5.1   Oslo testbed: compound coastal and riverine flood events

This section illustrates the application of a proposed methodology for multivariate events by analysing compound coastal and riverine flood events in Oslo. Surge height (m) and river flow (m^3/s) are selected as intensity measures for coastal and riverine floods, respectively.

5.1.1 Data

This study employs a diverse set of data related to surge height, river flow, and flood inundation resulting from coastal and riverine flooding. Table 5.1.1 provides an overview of the data, including their timeframe, temporal resolution, spatial resolution, and sources. To identify joint extreme events, involving surge and river flow, various global databases are employed, considering the availability of information for both baseline and future scenarios. Specifically, reanalysis data is used for the baseline scenario, and modelled projected data is utilized for the future scenario. The "Global sea level change time series from 1950 to 2050 derived from reanalysis and high resolution CMIP6 climate projections" from Copernicus (Muis, 2023) is used for surge height, while the Futurestreams dataset, provided by Utrecht University, is used for the river flow. Both datasets provide results from several global climate models, therefore we selected the same model for surge and river flow. These global datasets cover extensive geographical areas. The selection of appropriate grid nodes is based on their proximity to real-world observed gauges of the same quantities.

Table 5.1.1 illustrates the location of the selected observed gauges (red points) and the closer grid nodes of the two datasets (green points). In terms of observed surge and river flow data, Oslo municipality features only one tidal station, as indicated by the Norwegian Hydrographic Service. However, there are several river gauges managed by NVE Sildre. Among these river gauges, we focus on the Gryta gauge due to its proximity (~10 km apart) to the tidal station. The selection of tidal and river gauges in proximity is crucial for analysing compound flood events (Ghanbari *et al*., 2021). The Gryta station is situated in a small inflow of the Maridalsvannet Lake, hence the discharge is not very high. It is, however, representative of the catchment basin's behaviour and quick response to rainfall.

Table 5.1.1 Different types of data used to analyse compound flood events in Oslo.

Indicator	Dataset	Timeframe	Temporal resolution	Spatial resolution	Source

| Surge height | Copernicus dataset: Global sea level change time series from 1950 to 2050 derived from reanalysis and high resolution CMIP6 climate projections | ERA5 reanalysis: 1979 to 2018

Climate projections future: 2015 to 2050 | Reanalysis: 10-minute, hourly and daily maximum

Climate projections historical and future: 10-minute, annual | Coastal grid points: 0.1°

Ocean grid points: 0.25°, 0.5°, and 1° within 100 km, 500 km, and >500 km of the coastline, respectively | Muis *et al*., (2022) https://api.seha vniva.no/tidea pi_no.html |
|---|---|---|---|---|---|
| River flow | Futurestreams dataset | E2O reanalysis: 1976 – 2005 Future: 2006–2099 | Weekly averaged data | 10 km × 10 km | Wanders, *et. al.* (2021) https://sildre.n ve.no/ |
| Riverine flood inundation | Aqueduct Floods Hazard Maps | Base year: 1980 Projected year: 2030, 2050, 2080 | Return periods: 1, 2, 5, 10, 25, 50, 100, 250, 500, and 1000 years. | 5′ × 5′ | Ward *et al*. (2020) |
| Coastal flood inundation | The Norwegian Water Resources and Energy Directorate – NVE flood maps | Base year: 2017 Future year: 2100 | Return periods: 20, 200, and 1000 years. | Vector data | The Norwegian Water Resources and Energy Directorate – NVE |

To investigate the spatial distribution of riverine and coastal flood hazard intensities, we use two datasets. For riverine flood inundation maps, Aqueduct flood maps are utilised due to the availability of coastal and riverine flood inundation data for various RPs under historical (baseline) and future climate change scenarios. The analysis of potential future compound flood events considers the RCP 8.5 climate change scenario and mid-to-end-of-century projections. Regarding coastal flood inundation in Oslo, NVE flood maps from the Norwegian Water Resources and Energy Directorate are employed (NVE, 2023). Coastal flood inundation extent is provided for baseline (year 2017) and future (year 2100) climate change scenarios, considering return periods of 20, 200, and 1000 years. However, since the coastal flood maps are in vector format, they are converted into a gridded dataset using the methodology outlined by Cohen *et al*. (2018). The European Digital Elevation Model (EU-DEM) at a 25m spatial resolution is used for this conversion process, transforming the flood extent into water depth.

*************************************   **

5.1.2. Joint extreme events

Following the methodology outlined in section 3.2, we identify joint extreme events by analyzing time series of surge and river flow data at both baseline and future scenarios. Joint extreme events are recognized when values exceed the threshold for surge height and river flow. These thresholds are determined based on Kendall's rank correlation coefficient (τ). To identify optimal thresholds (i.e., percentile) for surge height and river flow in the context of compound flood events in Oslo, a sensitivity analysis has been performed by testing various combinations of thresholds (Appendix Tables A1.2-A1.3).

For the baseline period (1979–2005) and future scenario (2024–2050), Figure 5.1.1 presents different threshold combinations for the two drivers along with their corresponding τ values. In the baseline scenario, we choose the 90th percentile as the threshold, resulting in the highest τ value of 0.44. The surge height and river flow threshold values are 0.73 m and 1.59 m³/s, respectively. A total of 20 compound flood events have been identified from 1979 to 2005. Figure 5.1.2a illustrates these joint extreme events at the baseline scenario.

In the future scenario, we also select the 90th percentile for surge height and river flow as thresholds, yielding a τ value of 0.02 (Figure 5.1.1). The surge height and river flow threshold values are 0.67 m and 1.95 m³/s, respectively. While three other threshold combinations result in higher τ values, they yield very few joint extreme events (see table in Appendix A1.3). A relatively lower τ value could be attributed to the availability of coarser temporal resolution data, which could cause an impact on the extreme events detected. However, the τ that we selected agree with existing studies, carrying out similar analyses. For instance, Ming *et al*. (2022) found a *flow/surge* Kendell's coefficient equal to 0.0216 while Ghanbari *et al*. (2021) Kendell's coefficient for *flow/sea level*, ranged from -0.03 to 0.30. As explained in section 3.2, the optimal percentiles for the threshold and the length of the search window are determined through the evaluation of τ values *and* the number of extreme pairs to allow the bivariate analysis. A total of 27 compound flood events are identified over the projection period of 2024–2050.
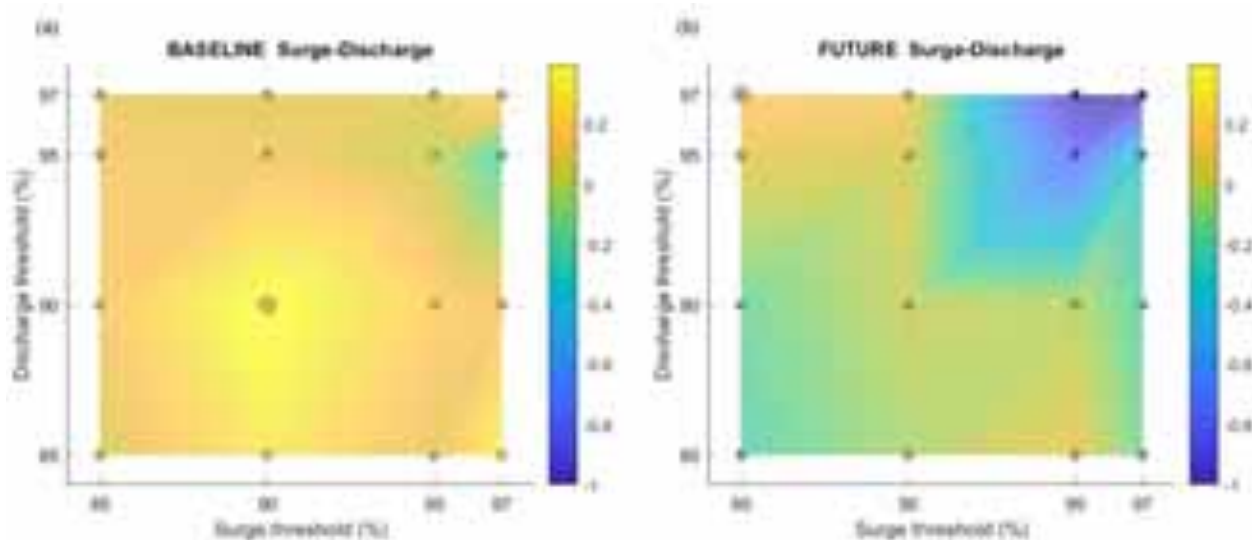

Figure 5.1.1 Various combinations of thresholds for surge height and river flow along with the resulting Kendall's rank correlation coefficients (τ). The red circle highlights the thresholds selected for joint probability analyses. (a) Baseline condition; (b) Future climate change scenario.
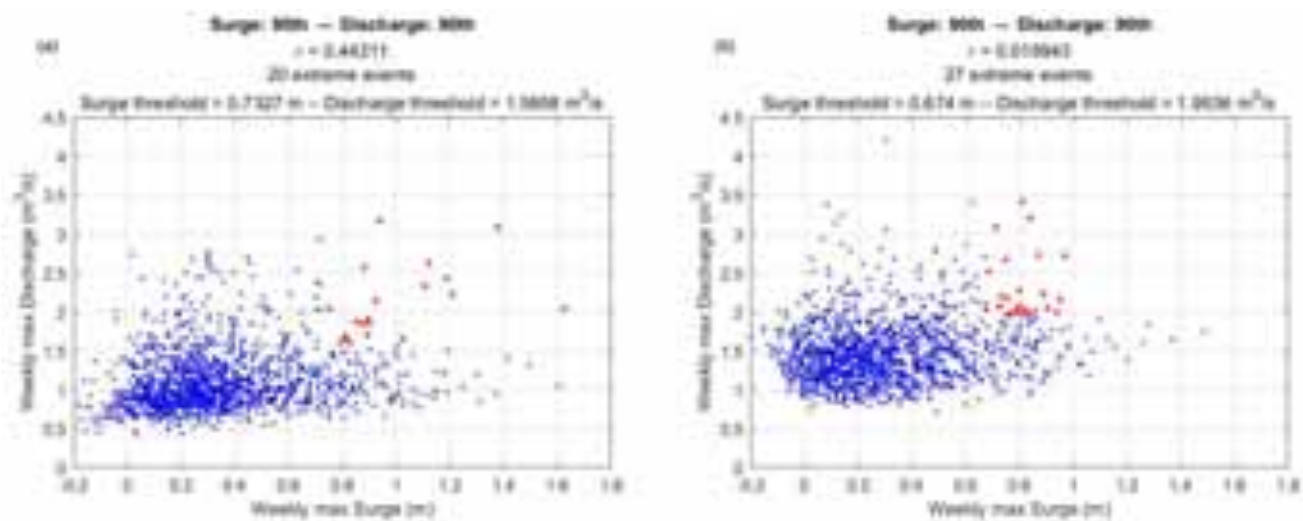
Figure 5.1.2 Joint extreme events. Scatter plot of all pairs of weekly sea surge level and river flow (blue) and pairs of extreme compound events (red). (a) Baseline scenario; (b) Future climate change scenario.

5.1.3. Joint probability of compound flood events

After identifying joint extreme events in Oslo under both baseline and future scenarios, the analysis focuses on the probability of concurrent coastal and riverine flood events by estimating their JRPs. As detailed in section 3.2, a Stan model is utilised, featuring a GPD for the marginal distribution of the single variable, and uniform priors. The joint extreme events identified in Figure 5.1.2 serve as input data for JRP estimation.

Initially, the marginal cumulative distribution function of flow and surge is computed by fitting selected extreme data to a GPD. The Stan language implementations of the GPD, following Vehtari (2017), are used, with exceptions for the inverse cumulative distribution function, quantile function, and pdf curves, which are implemented based on Zaiontz (2020). Subsequently, utilising a Gumbel copula, the joint distribution function is estimated. For the Gumbel copula probability density function, the implementation by Goodrich (2017) is employed, while the cumulative distribution function is coded for this study.

A model diagnostic is performed by running four chains for 5,000 samples each. The diagnostic indicates no divergences, and the chains exhibit good mixing with minimal autocorrelation. Both the effective sample size and $\hat{R}$, confirm that the model adequately samples the posterior. For random draws from the Gumbel copula for posterior predictive checks, the procedure outlined in Nelsen (2006) and Genest and Rivest (1993) is implemented in Stan. The goodness of the GPD fitting is checked with the Bayesian Quantile-Quantile plot. While the model fits smaller extreme values well, it struggles with the largest ones. However, Posterior Predictive Checks yield satisfactory results. Finally, the corner plot illustrates the correlation between the scale and shape parameters for the GPD. No unusual patterns are detected, but the θ parameters of the Gumbel copula are close to 1, indicating weak correlation between surge and flow data. Model diagnostic results are provided in Appendix A1 (see Figures A1.1-A1.5).

For the baseline scenario, the JRPs estimated for surges and flows are shown in Figure 5.1.3. The figure shows that when only the surge component is considered, the maximum RP is approximately 57 years among the 20 extreme events. The maximum RP for river flow is estimated to be around 22 years. However, for the combined hazard scenario, the maximum JRP is approximately 63 years, a combination of a 57-year surge and a 3-year river flow event. Generally, relatively low-intensity compound flood events are found to be frequent, and this pattern is projected to continue in the future.
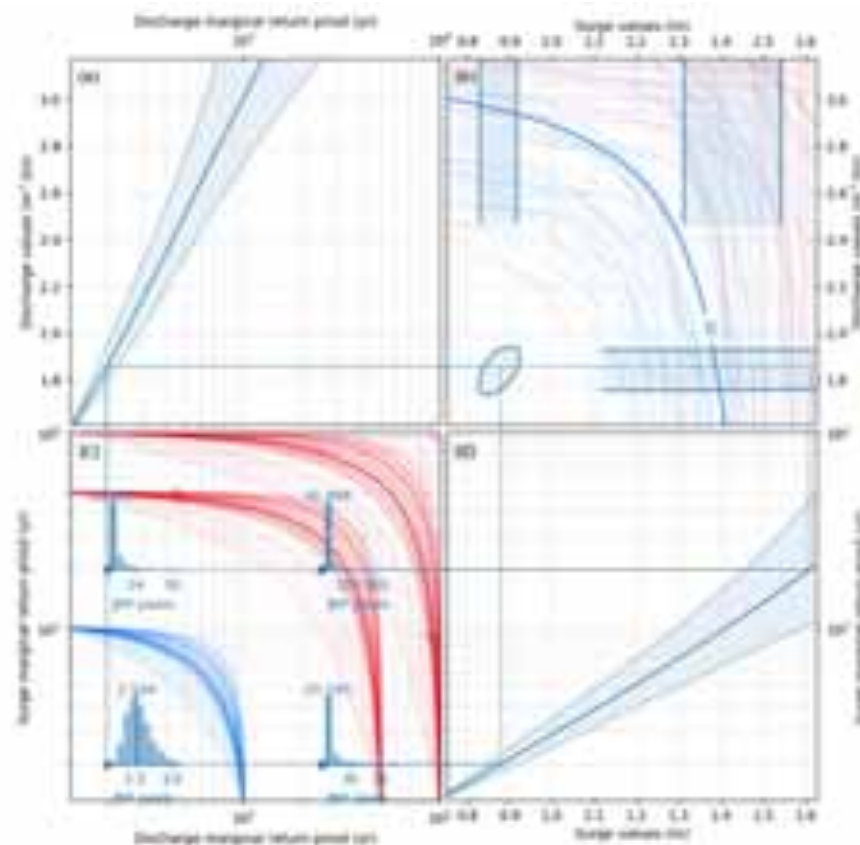
Figure 5.1.3 Plots of the 20th, 50th and 80th posterior marginal probabilities across return periods for river flow (a) and surge (d) under baseline conditions. The distribution of Joint Return Periods (JRPs) across surge and flow values is depicted in panel (b). JRPs for four random joint extreme events are displayed in panel (c). The contour lines in panels (b) and (c) represent the JRP in years. The bold lines of the contour (red and blue) indicate the median JRP, while the remaining lines represent random draws from the posterior distribution, providing an understanding of the variability.

In Figure 5.1.3, and all similar figures with return-period-based probabilities, each data point is visualised as a distribution. This means that there is a MRP for each individual driver value and a JRP for each combination of driver values. We represent the variation in JRP as a contoured surface over driver values in the upper right frame (Figure 5.1.3). To the left and below this frame, we plot the MRP as a function of driver value, so the MRP for any point in the top right plot can be read easily. This naturally defines a panel in the lower left with axes of MRP, which is where we plot the JRP again, but this time as a function of driver MRP, again visualised using contours.

However, the addition of the data to our model specifies a distribution across the five-dimensional parameter space, rather than a single best fit point, and therefore a distribution over MRP for each driver value and a distribution over JRP for each pair of driver values. This has several consequences. Firstly, we have a distribution over JRP contours, which is difficult to visualise – here we have opted to simply plot the contours of the 50th percentile JRP surface (in bold) as well as the contours for some randomly selected samples from the parameter space (fainter) to give an idea of the variability. This is less of a problem for the 1D MRP plots where we simply show the 20, 50 and 80th percentile curves. Secondly, it means that there is no one-to-one relationship between driver MRP and value. If we select an extreme event using two MRP values in the lower left plot it will define a distribution over driver values in the top right plot and vice versa. The corresponding distribution over bivariate driver MRP or value for a point defined in the opposite panel is shown as blue

contour enclosing x% of the probability mass. The distribution of JRP for a given point is plotted over the contour plot as a histogram.

Among the 27 extreme events identified in the future scenario, the most extreme surge and river flow events are estimated to be 1-in-112-year and 1-in-20-year events, respectively. The highest JRP is found to be 285 years, a combination of a 112-year surge and a 7-year river flow (see Figure 5.1.4). The overall JRP for the future scenario appears to be higher than the baseline scenario. This indicates that low-probability and high-intensity compound flood events are likely to become more prominent compared to the baseline scenario. Figure 5.1.5 provides a comparative picture of JRPs between the baseline and future scenarios.
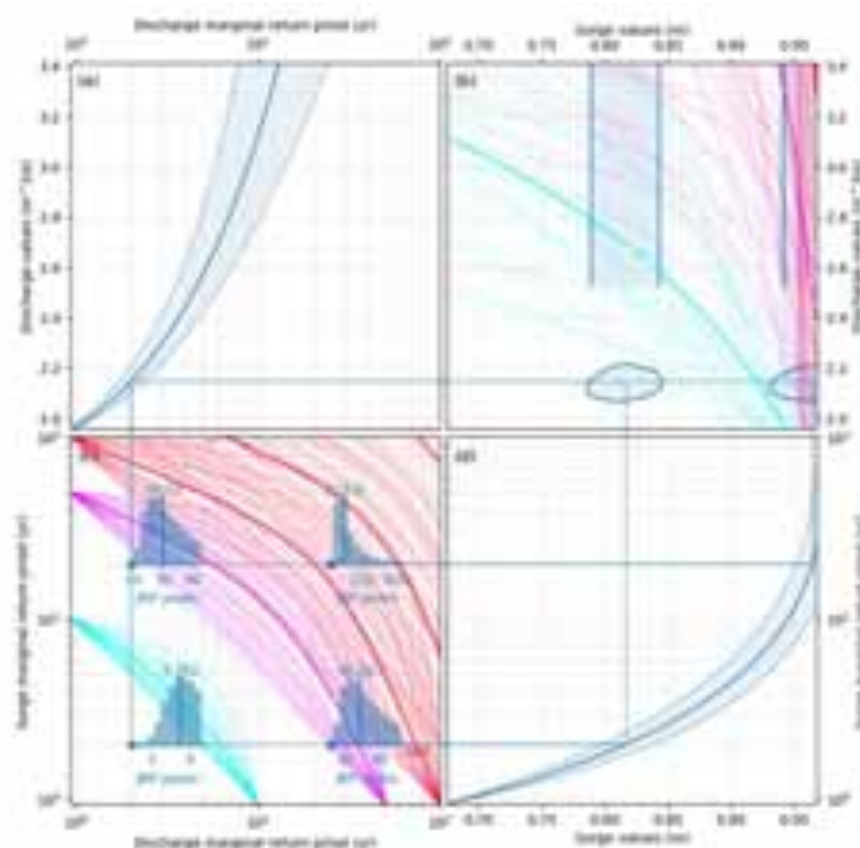
Figure 5.1.4 Plots of the 20th, 50th and 80th posterior marginal probabilities across return periods for river flow (a) and surge (d) under future climate change conditions. The distribution of Joint Return Periods (JRPs) across surge and flow values is depicted in panel (b). JRPs for four random joint extreme events are displayed in panel (c). The contour lines in panels (b) and (c) represent the JRP in years. The bold lines of the contour (red and blue) indicate the median JRP, while the remaining lines represent random draws from the posterior distribution, providing an understanding of the variability.

Figure 5.1.5 (a) JRPs estimated for different joint extreme events identified at baseline and future scenarios; (b) surface plot comparing JRPs between baseline and future scenarios.

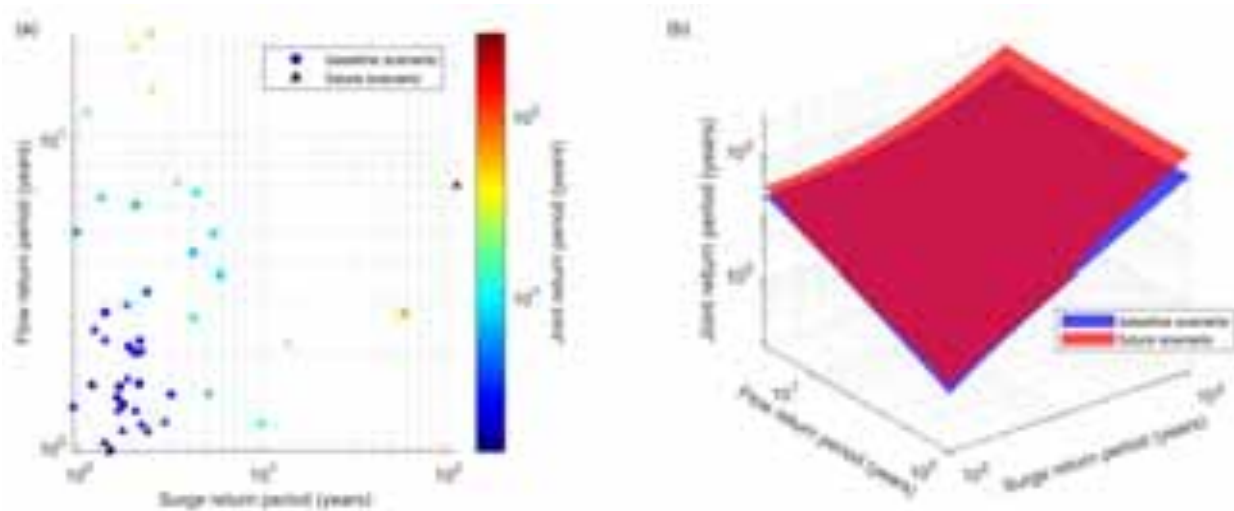The outcomes of joint probability analyses offer insights into various scenarios of compound flood events. For instance, Table 5.1.2 presents four random scenarios of compound flood events in Oslo under both baseline and future climate change conditions, as also highlighted in Figure 5.1.3 and Figure 5.1.4. While the probabilities of potential future events are relatively low, their intensities, especially for surge events, surpass those observed under baseline conditions.

Table 5.1.2 Sample compound flood scenarios in Oslo derived from joint probability analyses.

Scenarios	Surge return period (year)	River flow return period (year)	Joint return period (year)	
			Baseline	Future
1. Low surge and low flow	2	2	2.5	3.8
2. High surge and low flow	20	2	20.5	29.7
3. Low surge and high flow	2	25	25.5	36.6
4. High surge and high flow	20	25	41.5	113.9

5.1.4. Spatial distribution of coastal and riverine flood events

The identified compound flood events can be incorporated into a hydrodynamic flood model to analyse the spatial distribution of such occurrences. However, the scope of the MEDiate project does not encompass the establishment of hydrodynamic flood models. To gain insights into flood inundation extents, we utilize the Aqueduct Floods Hazard Maps and NVE flood maps (see Table 5.1.1). Figure 5.1.6 and Figure 5.1.7 depict the spatial extent and depth of riverine and coastal flood events with different return periods, respectively. These flood maps facilitate the quantification of exposure and risk to populations and assets resulting from various types of flooding.

It is evident that the probable extent of inundation during riverine flooding is substantially larger than that of coastal flooding. We also compare the depth and extent of these two types of flooding for baseline and future scenarios. The results indicate a significant increase in the depth of

inundation in the future, while no significant changes in the extent of inundation are observed. Areas near the coastal region are more susceptible to both riverine and coastal flooding compared to inland areas. These results validate the outcomes of joint extreme event analysis, which identifies several compound flood events in both baseline and future scenarios.
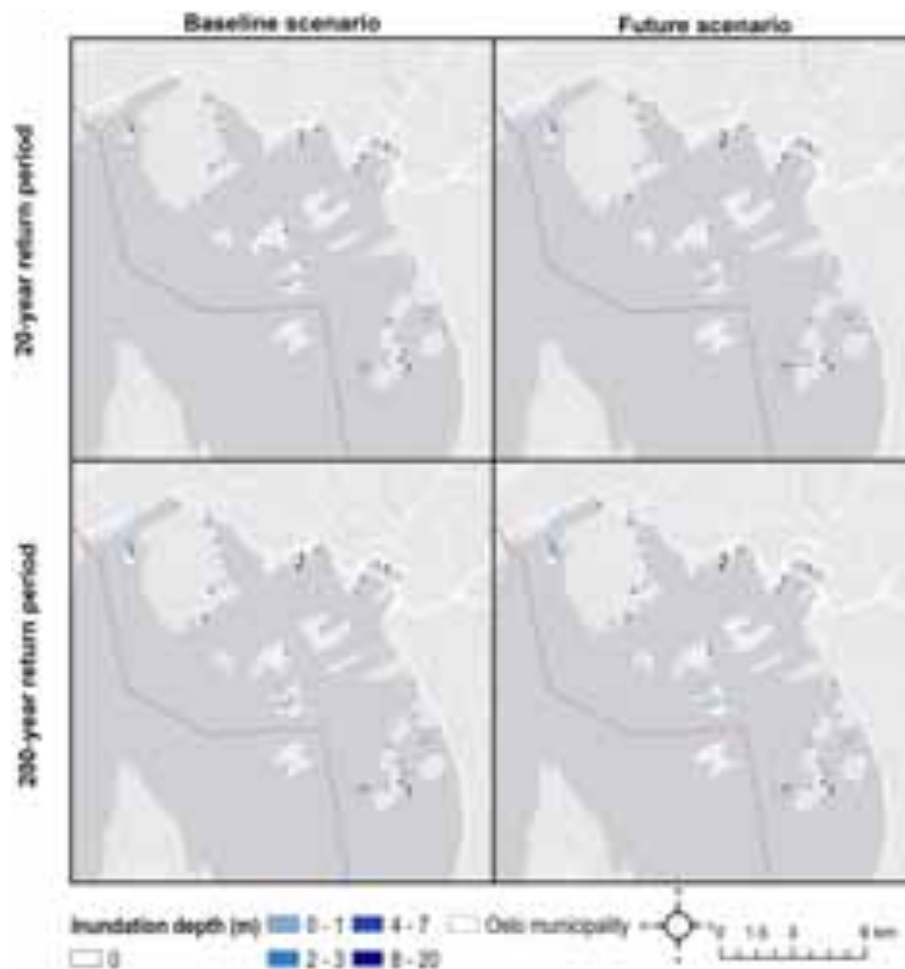

Figure 5.1.6 Spatial distribution of coastal flood prone areas in Oslo at baseline and future scenarios. These figures only show flood depth and extent along the coastline in Oslo municipality.
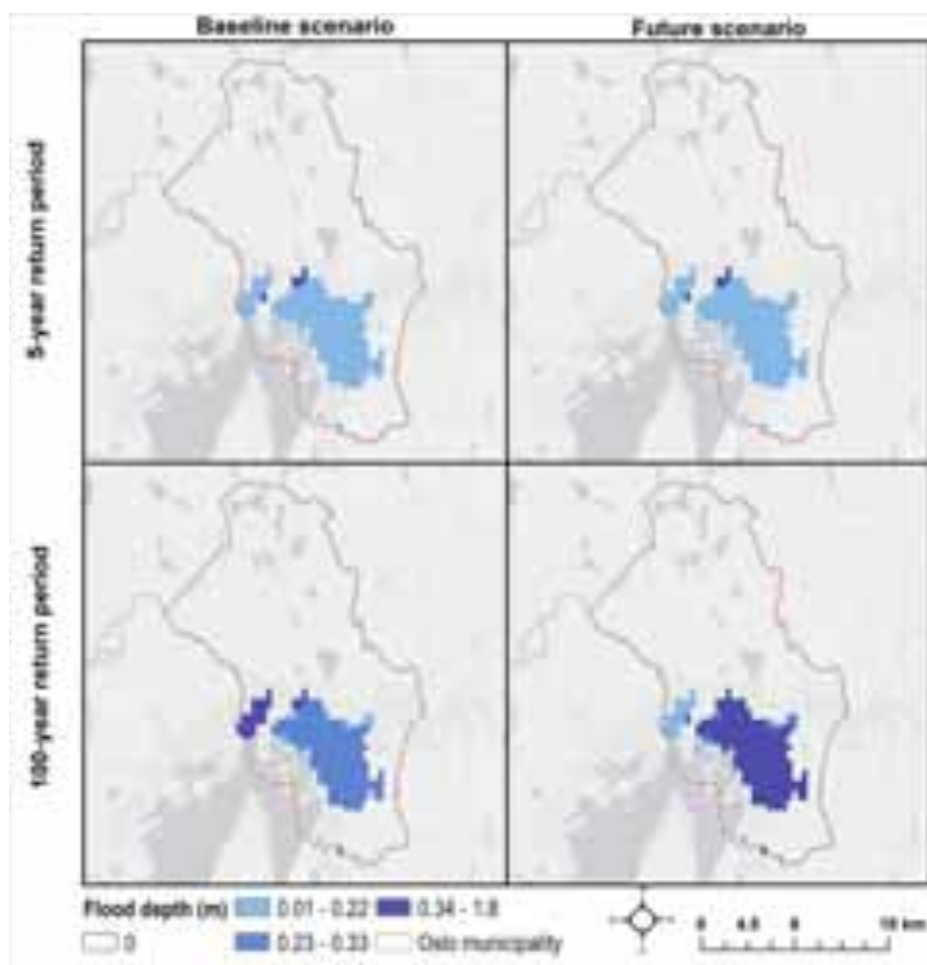
Figure 5.1.7 Spatial distribution of riverine flood prone areas in Oslo at baseline and future scenarios.

5.2   Nice testbed: Extreme heat and drought

This section demonstrates the execution of a proposed approach for spatially compounding events (section 3.3.) by investigating extreme heat and drought. This is achieved by identifying the compound co-occurrence of heat waves and droughts, employing standardized Heat Wave Index and Standardized Precipitation Index.

5.2.1. Data

This testbed employs a diverse set of data related to daily ground-based temperature and precipitation measurements. Table 5.2.1 provides an overview of the data, including their timeframe, temporal resolution, spatial resolution, and sources. For all indicators, an open database is used due to the availability of information for both baseline and future scenarios. The present analysis uses climate simulations for the European domain performed by Regional Climate Models (RCMs), made available by the EURO-CORDEX climate modelling initiative. A multi-model approach is required to provide an estimation of the uncertainty associated with the individual model sensitivity to the increasing radiative forcing driven by increasing green-house gas concentrations. RCMs dynamically downscale global climate simulations run within the Climate Model Intercomparison Project phase 5 (CMIP5; Taylor et al., 2012) to a spatial scale of 0.11º (~12.5 km). In this research, the simulations are run for the historical period (1850–2005), and future projections (2006–2100) are run in low (RCP 2.6), medium (RCP 4.5) and high (RCP 8.5) emission scenarios. For this analysis, climate simulations run with the RCM CSC-REMO2009 (REMO hereafter) are used. REMO was created originally at the Max-Planck-Institute for Meteorology (MPI), and it is currently maintained at the Climate Service Center Germany (GERICS).

REMO downscales historical climate simulations and future climate projections run with the global climate model MPI-ESM-LR (MPI hereafter). Specifically, REMO outputs analysed in this study are the downscaling of one MPI historical simulation for the period 1971–2005, and one MPI climate projection in the RCP 8.5 scenario for the period 2006–2100. REMO data are also biased corrected, using the EFAS-Meteo data set as a reference (Ntegeka *et al.*, 2013), re-gridded to a spatial resolution of 5km and daily means are analysed.

Table 5.2.1 Regional climate models simulation and data used to compute the heat wave and drought indices.

RCM	Forcing GCM	Realizations	RCP	Time frame	Spatial resolution	Variables
CSC-REMO2009	MPI-ESM-LR	r1i1p1 r2i1p1	8.5	1971–2100 in a daily basis	5 km	2-m temperature Precipitation

This dataset served as input for the detailed analysis explained below, summarized in the following three steps: (1) identification of heat wave events at grid-point level, based on a monthly standardized HW index; (2) identification of drought events at grid point level, based on a 3-month Standardized Precipitation Index (SPI3); (3) identification of compound co-occurrence of heat waves and drought (COHWD) at grid point level and at the monthly time scale.

Heat waves were identified during the summer season (June to August), for every year during the period 1971–2100. Here, a heat wave is defined as a hot spell of at least 3 consecutive hot days defined as days with maximum temperature above the 90th percentile. The 90th percentile was computed following a similar approach as Fischer and Schär (2010): for each day of summer, the percentile was calculated during the whole period (1971–2100) using a 15-day moving window. Subsequently the number of hot days belonging to a heat

wave (i.e. isolated hot days were not considered) for each summer month was computed, and a monthly standardized heat wave index (HWI) was defined. Monthly heatwave (HW) events were identified as the months exceeding 1 in the HWI.

Drought was defined using the SPI, calculated using the nonparametric approach by Hao *et al*. (2014), where a marginal probability distribution of precipitation is computed using the empirical Gringorten plotting position, as shown in Equation 1 (Hao et al. (2014; Hao and AghaKouchak, 2014; Gringorten, 1963). The empirical probability of precipitation (P_p) is then standardized as SPI= $\varphi^{-1}(P_p)$, with φ being the standard normal distribution (Hao *et al*., 2014). Specifically, monthly drought events (D) were defined as summer months showing a SPI3 value below -1.

After monthly HW and D events were identified, the compound occurrence of heatwaves and droughts (COHWD) was determined for each summer month and at each grid point according to the following criterion (23):

$$COHWD = \begin{cases} 1, when\ HWI\ \geq\ 1\ and\ SPI3\ \leq\ -1 \\ 0, otherwise \end{cases} \qquad (23)$$

The frequency of occurrence of COHWDs is finally computed, considering three summer months within 30-year time slices, as the number of COHWDs out of 3x30 months. The 30-year time slices identified are: 1976–2005, to account for the historical period (Hist); 2041–2070, to account for the near future (NF); 2071–2100, to account for the far future (FF). Time slices are defined on 30 years in agreement with the WMO definition of climate normal, i.e. the minimum time span for the definition of a climatology.

5.2.2 Heatwaves

Figure 5.2.1 shows the number of hot days within a heatwave simulated by CSC-REMO2009 simulations. During the historical period (Figure 5.2.1a, d, g) most of the domain is affected by up to 1 hot day per month. Under the high emission scenario, the number of hot days increases in the NF to 1-2 along the French Mediterranean coast and up to 2-3 in the whole domain in June (Figure 5.2.1b, e, h). Towards the end of the century (Figure 5.2.1c, f, i), while the number of hot days increases to 6-7 along the French Mediterranean coast in June, the whole domain is affected by at least 6 days in July and August, with more than 10 days in the southern part.
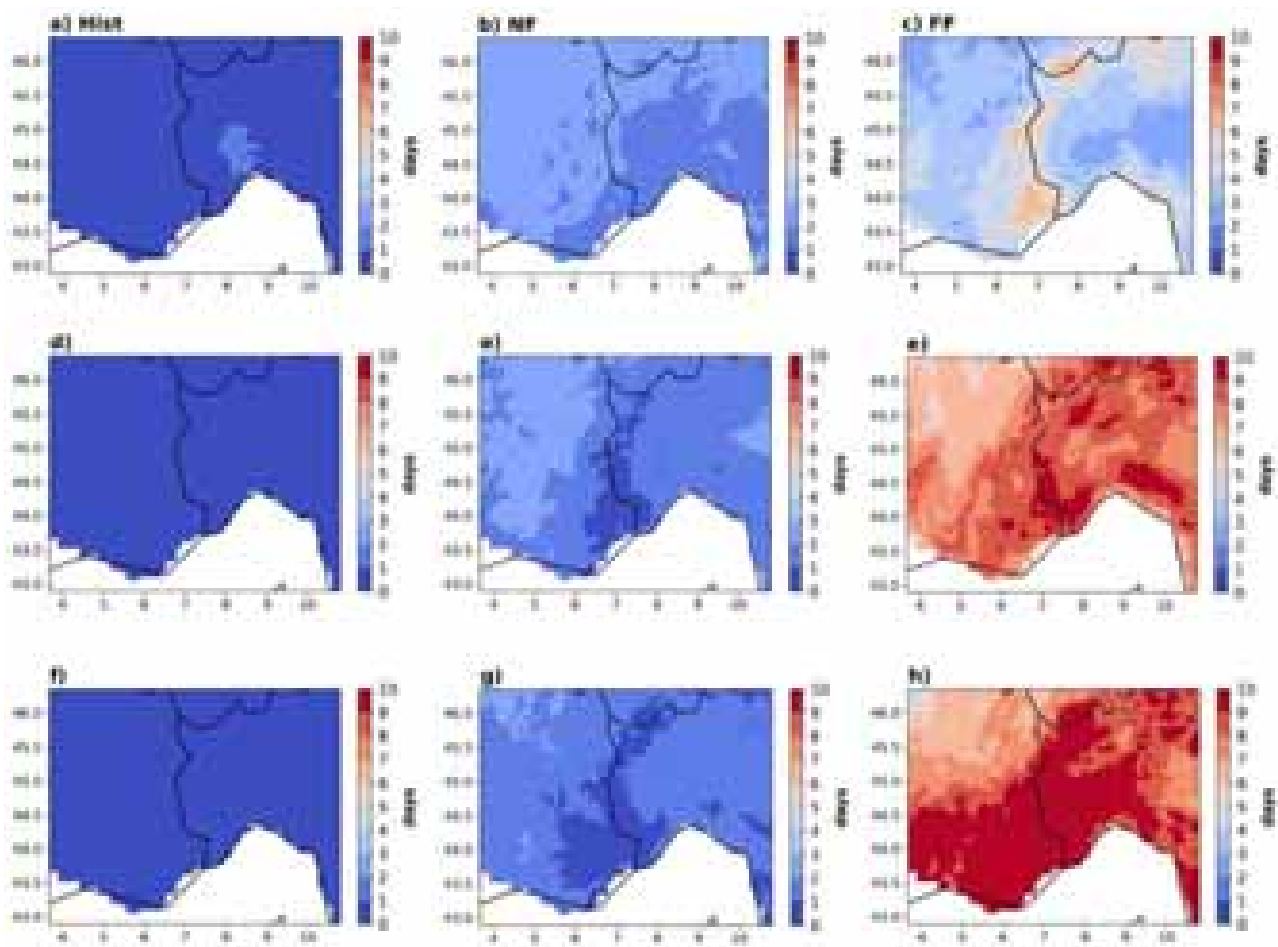
Figure 5.2.1 Number of hot days in a heatwave in (a-c) June, (d-f) July and (f-h) August, during (left) the Historical period (Hist: 1976–2005), (middle) Near Future (NF: 2041–2070) and (right) Far Future (FF: 2071–2100) periods.

5.2.3 Droughts

The climatology of the SPI in the three sub periods is presented in Figure 5.2.2. During historical time (Figure 5.2.2a, d, g) southern France shows slightly wet conditions. In the NF, the domain is characterised by overall wet conditions, with only limited areas experiencing dry conditions (Figure 5.2.2b, e, h). Towards the end of the century (Figure 5.2.2c-i), and especially in August in France (Figure 5.2.2i), the whole domain will experience SPI3 values between -0.5 and -1, indicating widespread dry conditions.

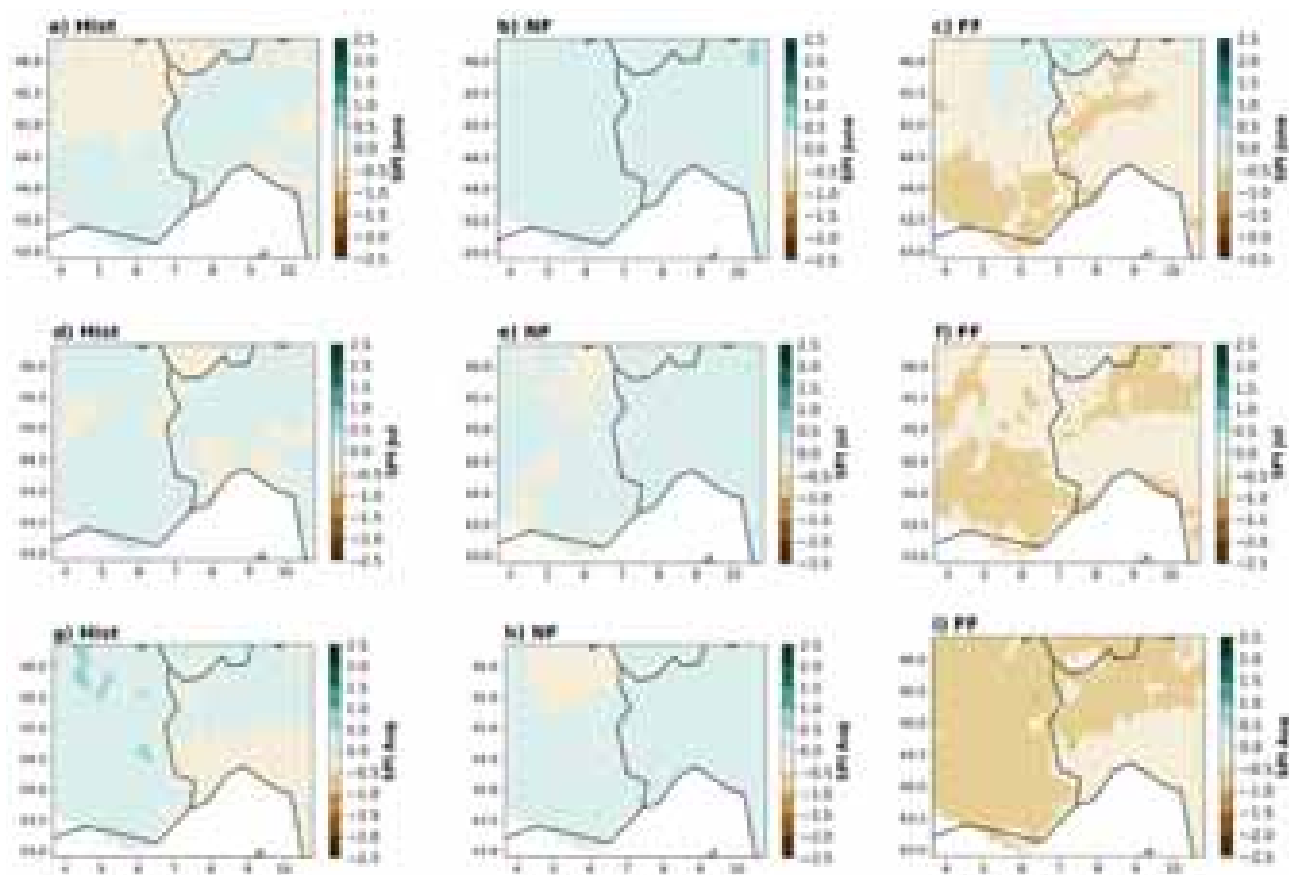*****************************   *****************************

Figure 5.2.2 Mean SPI3 in (a-c) June, (d-f) July and (f-h) August, during (left) the historical (Hist: 1976–2005), (middle) near future (NF: 2041–2070) and (right) far future (FF: 2071–2100) periods.

5.2.4 Compound Occurrence of Heat Wave and Drought

The frequency of COHWDs during each time slice is shown in Figure 5.2.3. In the historical analysis (Figure 5.2.3a), only a restricted region in France demonstrates approximately a 4% frequency of COHWD events. This means that ~4 summer months are characterised by hot and dry conditions during this period. During NF (Figure 5.2.3b), the frequency increases up to 5% (~6 summer months) along the French Mediterranean coast, with peaks above 10% in the Rhone Valley, i.e. around 9 summer months characterised by extreme conditions. During FF (Figure 5.2.3c), southern France is characterized by COHWD frequency exceeding 10% frequency, corresponding to a widespread area experiencing at least 9 hot and dry summer months.
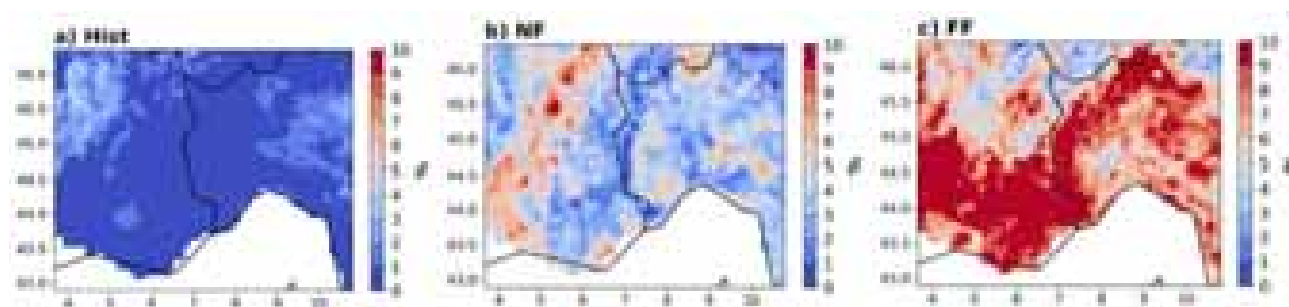

Figure 5.2.3 Frequency of occurrence of COHWDs (%) in summer during (a) the historical (Hist: 1976–2005), (b) near future (NF: 2041–2070) and (c) far future (FF: 2071–2100) periods.

5.3   Essex testbed: Extreme wind and rainfall

The hazard pair involves analysing joint extreme wind and rainfall events, which are defined as spatially compounding multi-hazard events. Daily maximum wind speed of gust at 10m (m s^{-1}) and daily precipitation (mm) are selected as indicators for wind and rainfall, respectively.

5.3.1. Data

In the analysis of extreme wind and precipitation events, this study utilizes the UK Climate Projection 2018 datasets. Table 5.3.1 presents a comprehensive overview of the data, encompassing details such as the timeframe, temporal resolution, spatial resolution, and sources. The baseline scenario for these indicators incorporates data from 1981 to 2000, while the future scenario comprises data from 2061 to 2080. The extraction of wind and precipitation data is conducted based on the Essex County boundary (Figure 1.2.3). Figure A3.1 in Appendix shows the spatial distribution of the grid and the cells considered for the analysis.

Table 5.3.1 Different types of data used to analyse extreme wind and precipitation events in Essex.

Indicators	Dataset	Timeframe	Temporal resolution	Spatial resolution	Source
Maximum wind speed of gust at 10m (ms^{-1})	UK Climate Projection 2018 (UKCP18) data	The projections cover the UK and three time-slices (1981–2000, 2021–2040 and 2061–2080), for a high emissions scenario, RCP8.5.	Daily	5km	Met Office Hadley Centre (2019)
Precipitation (mm)					

5.3.2. Joint extreme events

Following the methodology outlined in Section 3.3, we identify joint extreme events by considering both baseline and future scenarios. Following the harvesting of gridded wind gust speed and precipitation data from the UKCIP18 daily dataset, we pre-processed data to organise the timeseries data for estimating JRP. Daily maximum values of the two hazard intensity measures (wind speed and precipitation) across all grids within the study area are determined, resulting in the creation of two time series datasets.

The joint extreme wind and rainfall events occurs when gust speed and precipitation surpass the thresholds. Like multivariate events, these thresholds are established based on Kendall's rank correlation coefficient (τ). To pinpoint optimal thresholds (i.e., percentiles) for gust speed and precipitation in the context of spatially compounding events, various combinations of thresholds are tested (Appendix Tables A3.1-A3.2) Figure 5.3.1 illustrates different threshold combinations for the two drivers along with their corresponding τ values for baseline and future scenarios. Additionally, the selected thresholds are marked.

*******************************   *******************************
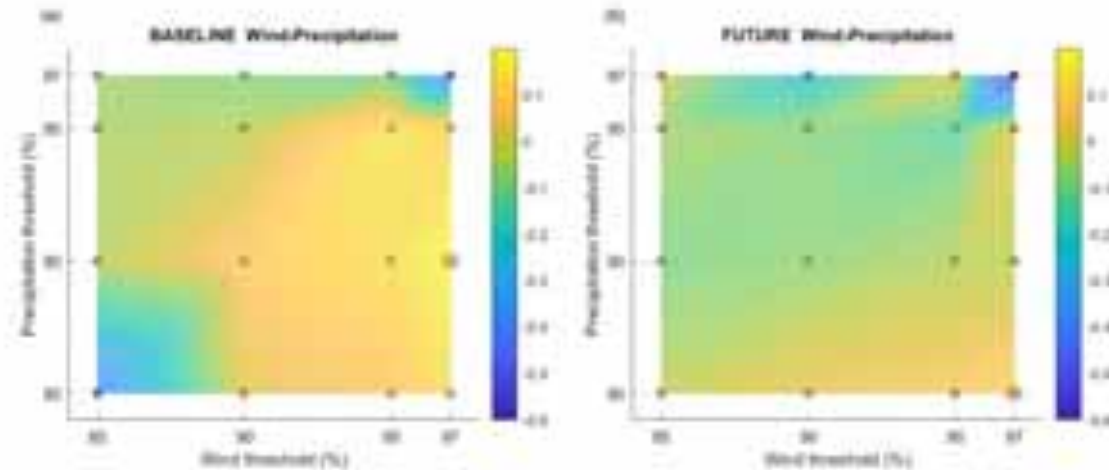
Figure 5.3.1 Various combinations of thresholds for daily maximum wind gust speed and precipitation along with the resulting Kendall's rank correlation coefficients (τ). The red circle highlights the thresholds selected for joint probability analyses. (a) Baseline condition; (b) Future climate change scenario.

In the baseline scenario (1981–2000), we opt for the 97th percentile for daily maximum wind gust speed and the 90th percentile for daily precipitation as the thresholds, yielding the highest τ value of 0.19. The threshold gust speed and precipitation values are 17.74m s^{-1} and 15.56 mm, respectively. A total of 46 joint extreme events are identified from 1981 to 2000, as illustrated in Figure 5.3.2a.

In the future scenario (2061–2080), we choose the 97th percentile for daily maximum wind gust speed and the 85th percentile for daily precipitation as the thresholds, resulting in the highest τ value of 0.09. The threshold gust speed and precipitation values are 18.07m s^{-1} and 11.46 mm, respectively. Over the 20-year projection period, 115 joint extreme events are identified (Figure 5.3.2b).
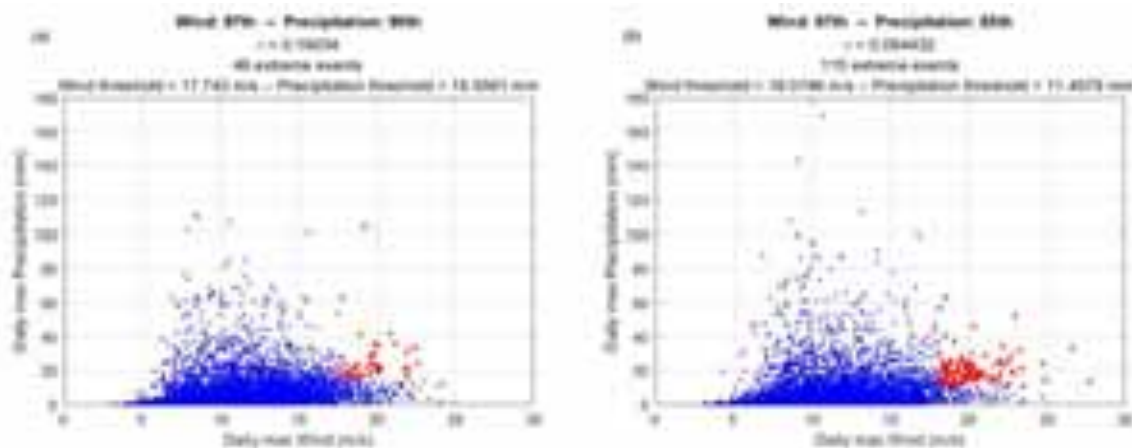
Figure 5.3.2 Joint extreme events. Scatter plot of all pairs of daily maximum wind gust speed and daily precipitation (blue) and pairs of joint extreme events (red). (a) Baseline condition; (b) Future climate change scenario.

5.3.3. Joint probability of extreme wind and precipitation events

Following the identification of joint extreme events, we used a Stan model with a Gumbel copula, GPD for the marginal distribution of the single variable with uniform priors, similar to the approach for multivariate events (see Section 3.2). The model incorporates input data from the joint extreme events identified in the previous section. The diagnostic results of the model are summarized in Appendix A3 (see Figure A3.2-A3.6).

For the baseline scenario, Figure 5.3.3 illustrates the JRP estimated for daily maximum wind gust speed and precipitation. Among the 46 joint events identified, the maximum daily gust speed is approximately associated with a 41-year RP. The maximum RP for precipitation is estimated to be around 134 years. Notably, the maximum JRP is approximately 163 years, representing a combination of a 1-year extreme wind and a 134-year precipitation event. Generally, relatively low-intensity joint extreme events are found to be frequent, and this pattern is projected to persist in the future.
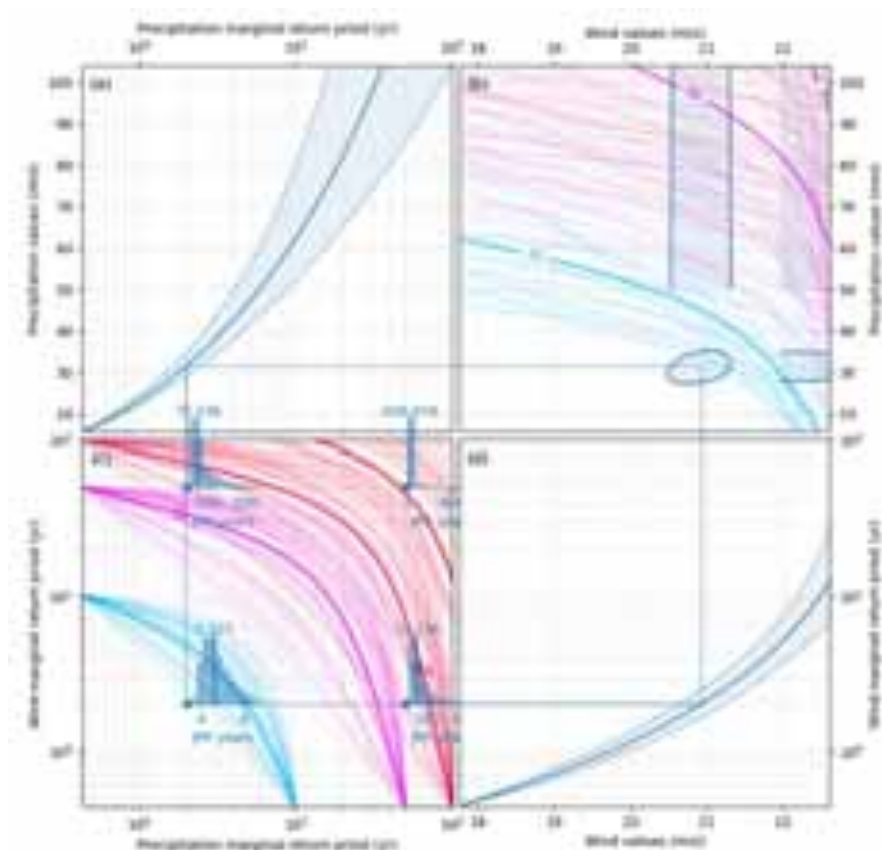

Figure 5.3.3 Plots of the 20th, 50th and 80th posterior marginal probabilities across return periods for daily precipitation (a) and daily maximum wind gust speed (d) under baseline conditions. The distribution of Joint Return Periods (JRPs) across surge and flow values is depicted in panel (b). JRPs for four random joint extreme events are displayed in panel (c). The contour lines in panels (b) and (c) represent the JRP in years. The bold lines of the contour indicate the median JRP, while the remaining lines represent random draws from the posterior distribution, providing an understanding of the variability.

In the future scenario (2061–2080), the number of joint extreme events is projected to increase to 115. Among these events, the highest RPs for daily maximum gust speed and daily precipitation are estimated to be 406 years and 77 years, respectively. The highest JRP is found to be 462 years, representing a combination of a 406-year daily maximum gust speed and a 1-year precipitation event (see Figure 5.3.4). While the most extreme precipitation event is associated with the highest intensity and lowest probability event in the baseline years, extreme wind is projected to have a more significant influence on future joint extreme events. Figure 5.3.5 provides a comparative visualization of JRPs between the baseline and future scenarios. Compared to baseline scenario, JRPs for the future scenario appears to be higher for relative less intensity events, while lower for high-intensity events (Figure 5.3.5 (b)). This indicates that that low-probability and high-intensity joint extreme wind and rainfall events are likely to become more prominent in the future.

**************************** ****************************
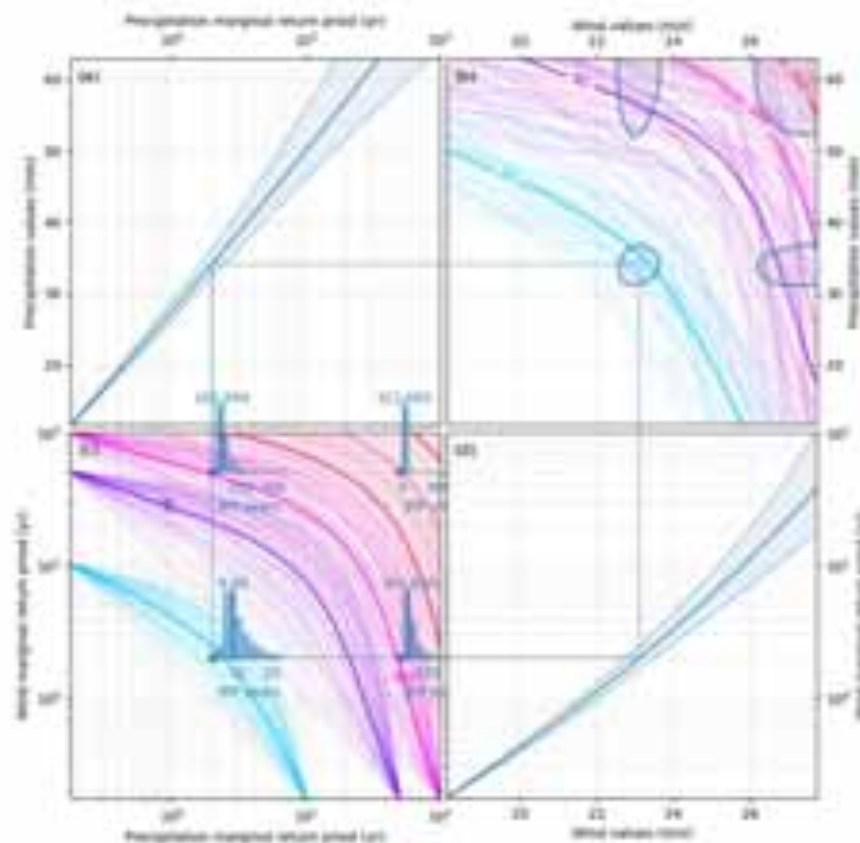
Figure 5.3.4 Plots of the 20th, 50th and 80th posterior marginal probabilities across return periods for daily precipitation (a) and daily maximum wind gust speed (d) under future climate change conditions. The distribution of Joint Return Periods (JRPs) across surge and flow values is depicted in panel (b). JRPs for four random joint extreme events are displayed in panel (c). The contour lines in panels (b) and (c) represent the JRP in years. The bold lines of the contour indicate the median JRP, while the remaining lines represent random draws from the posterior distribution, providing an understanding of the variability.

Figure 5.3.5 (a) JRPs estimated for different joint extreme events identified at baseline and future scenarios, (b) surface plot comparing JRPs between baseline and future scenarios.

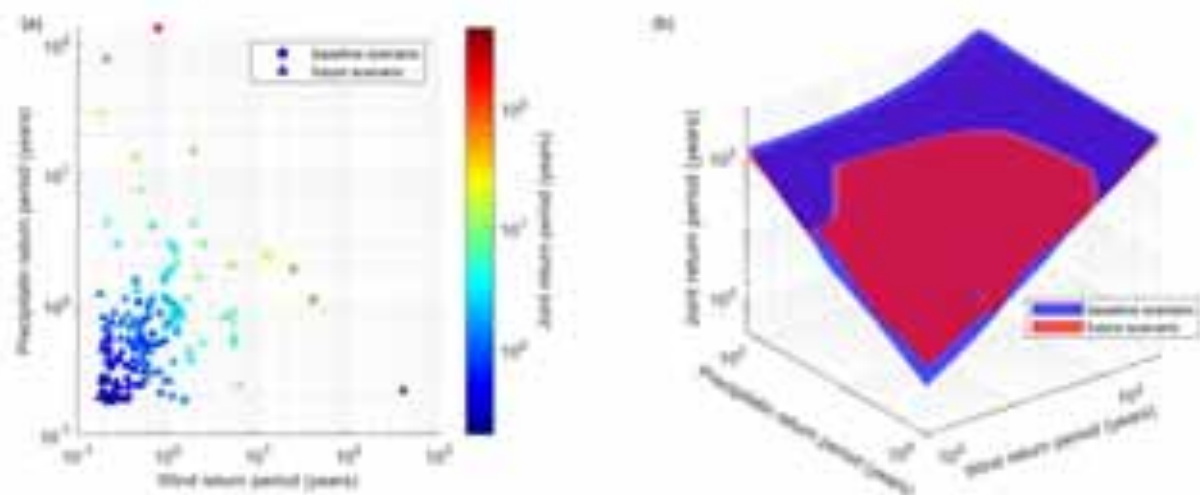The results of joint probability analyses provide valuable insights into different scenarios of joint extreme wind and precipitation events. As illustrated in Table 5.3.2 and highlighted in Figure 5.3.3 and Figure 5.3.4, four random scenarios of these joint extreme events in Essex are presented under both baseline and future climate change conditions. Although the probabilities of potential future events are relatively low, their intensities, particularly for wind events, exceed those observed under baseline conditions.

Table 5.3.2 Sample scenarios for joint extreme wind and precipitation events in Essex derived from joint probability analyses.

Scenarios	Return period of daily maximum wind gust speed (year)	Return period of daily precipitation (year)	Joint return period (year)	
			Baseline	Future
1. Low gust speed and low precipitation	2	2	5.2	8.9
2. High gust speed and low precipitation	50	2	72.7	103.9
3. Low gust speed and high precipitation	2	50	72.7	103.9
4. High gust speed and high precipitation	50	50	209.9	311.7

5.3.4. Spatial distribution of extreme wind and rainfall events

Following the methodology outlined in Section 3.3, we create RP maps for daily maximum wind gust speed and daily precipitation to assess the spatial distribution of extreme wind and rainfall events in Essex. Figure 5.3.6 present extreme wind maps for three different RPs (2-year, 200-year, and 500-year) in both baseline (1981–2000) and future (2061–2080) scenarios. Overall, the intensity of maximum daily gust speed is predicted to increase in the future. For example, the maximum gust speed of 19.2ms^{-1} in the baseline scenario is projected to rise to 20.5ms^{-1} for a 200-year event. Highly impacted areas are mostly concentrated along the coastline.

*******************************   *******************************
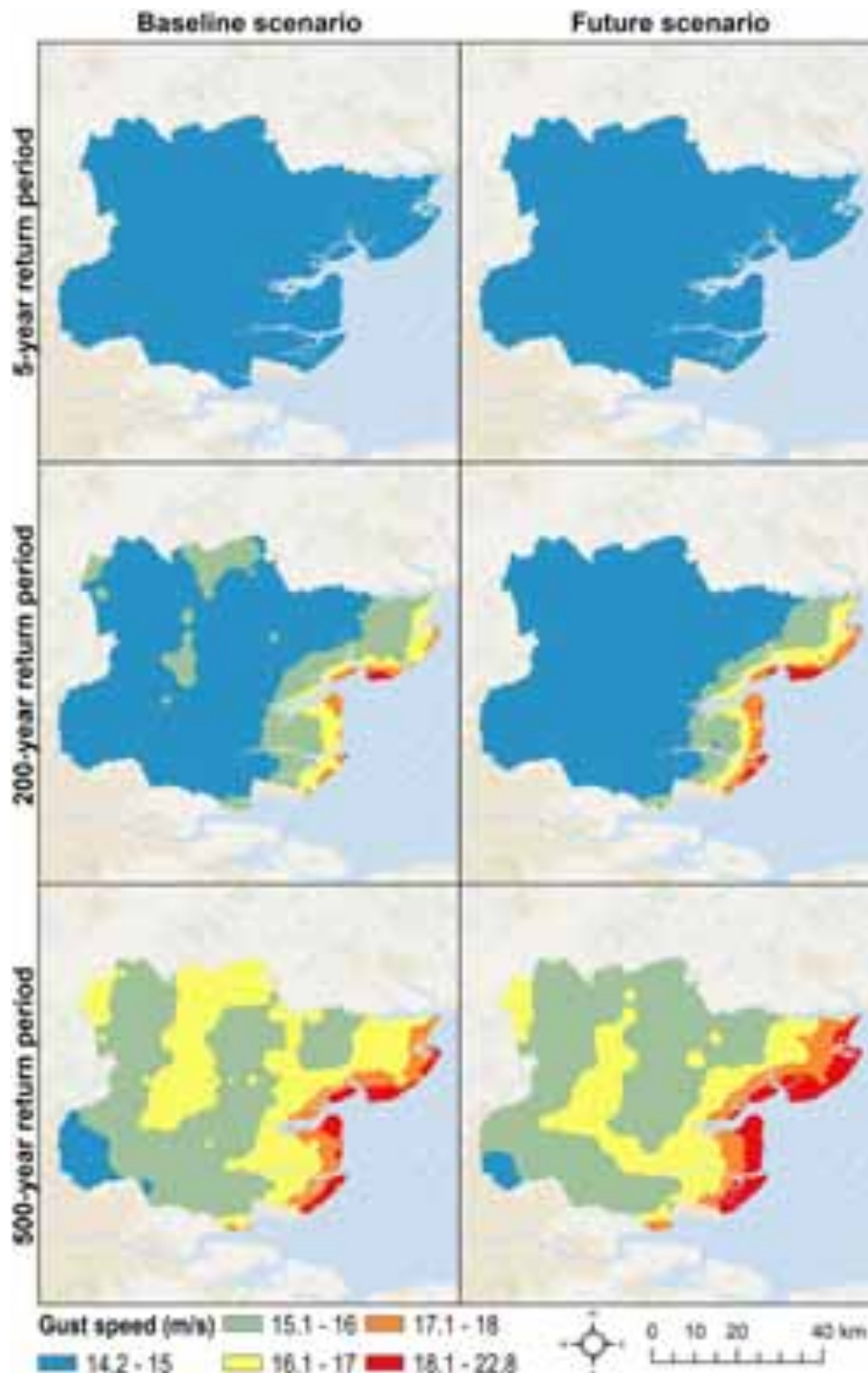
Figure 5.3.6 Spatial distribution of daily maximum wind gust speed for different return periods in Essex at baseline and future scenarios.

Figure 5.3.7 shows extreme precipitation maps for three different RPs (2-year, 200-year, and 500-year) in both baseline and future scenarios. Both the exposure and intensity of precipitation are expected to increase in the future. For a 200-year precipitation event, for instance, the maximum daily precipitation of 35.8mm across Essex County is projected to increase to 36.8mm in the future.

A larger area is likely to experience the impact of extreme precipitation in the future compared to the baseline conditions. The southwestern districts of Essex County are identified as being significantly exposed to extreme precipitation events.
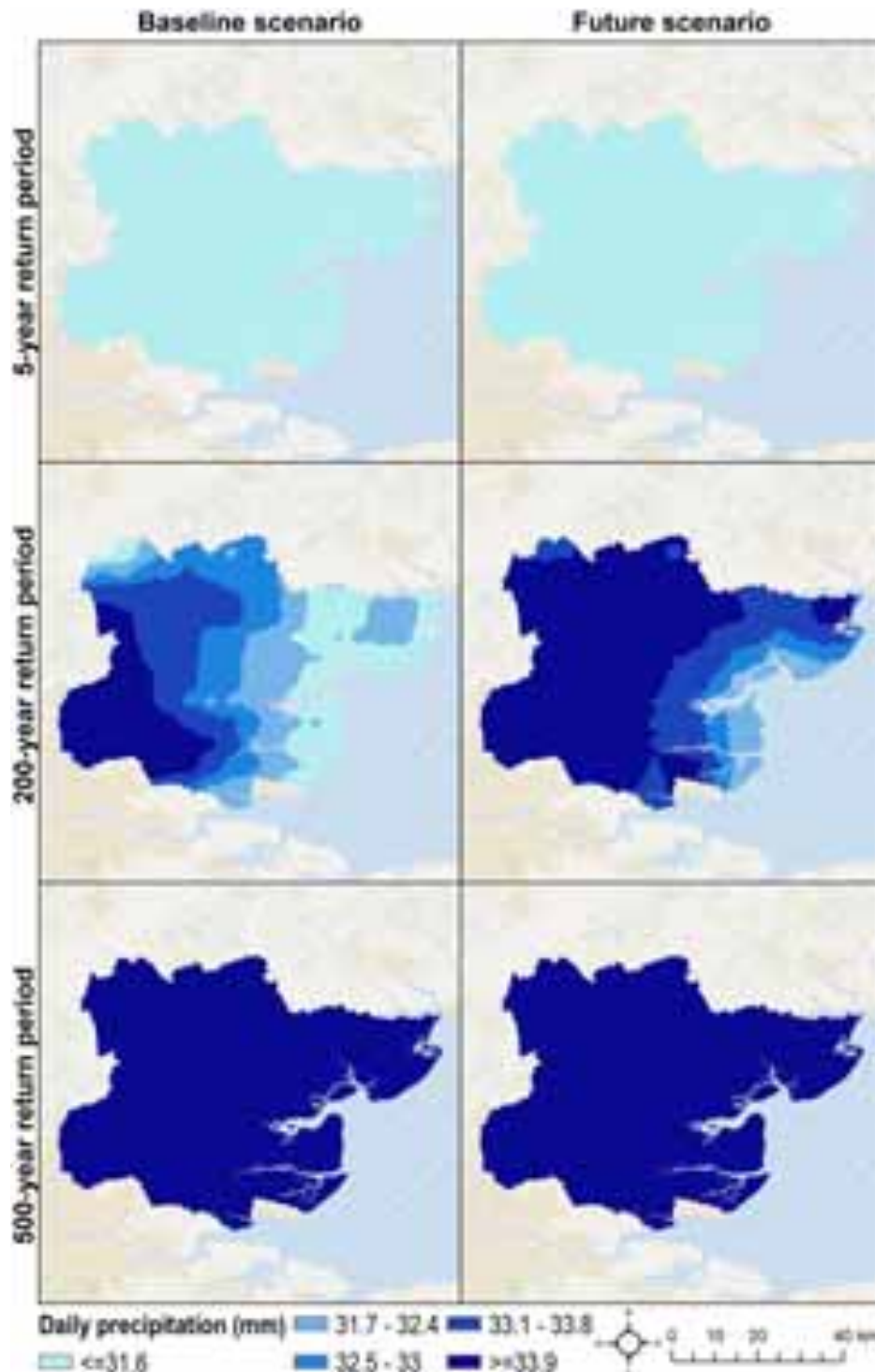

Figure 5.3.7 Spatial distribution of daily precipitation for different return periods in Essex at baseline and future scenarios.

*******************************   *******************************

5.4   Múlaþing testbed: heavy rain and landslides

The hazard pair involves analysing joint extreme rainfall and landslide events, which are defined as preconditioned and triggering events. Rolling sums of 1-day, 2-day, 3-day and 5-day rainfall (mm) in connection with extreme antecedent precipitation are selected as indicators of landslide hazard.

5.4.1. Data

The longest hourly precipitation data series for Seyðisfjörður is from the station Vestdalur, just outside Seyðisfjörður town and approximately 2.5 km from the critical hillside. The measurements date back to 1995 but gaps in the series, especially at critical times for landslide monitoring, led to the use of modelled data series. The ICRA atmospheric reanalysis project for Iceland (Nawri *et al.*, 2017) downscaled data series dates from 1979 to 2017, which also leaves out a critical period for landslide monitoring (i.e., the December 2020 event), but by using the ICRA series at least three critical events for this project are included. Massad *et al.* (2020) analysed the difference between the measured data and ICRA. They found that the correlation between measured rain and ICRA was good for Seyðisfjörður (Seyðisfjörður ICRA= 119 mm, observed =111 mm, correlation coefficient= 93%). The measured accumulated rainfall in Seyðisfjörður, during the days 14–18 December 2020, was a total of 569.9 mm, which is the highest ever recorded in Iceland (Björnsson *et al.*, 2023).

Measured daily temperature from the Dalatangi station was used to filter out snowfall. The station is located by the coast with open sea to the east and therefore would be expected to be warmer than stations in the town of Seyðisfjörður, a location in a narrow fjord. The climate data reanalysis CMIP6 (Coupled Model Intercomparison Project; Copernicus Climate Service, Eyring *et al.*, 2016) was tested for the point location of Seyðisfjörður. The models that are considered the most representative for the area had around three times too few maximum values compared to ICRA data. It was not within the scope of this project to fit the best model to the station site. Therefore, it was considered acceptable to test the tools and methodology to repeated ICRA data and add expected extreme increases to simulate future rainfall. As mentioned above, we projected rainfall data by multiplying the historical data by an estimated precipitation increase. While this method simplifies the link to the specific location, it has limitations. Notably, it artificially repeats weather patterns every 37 years with adjusted intensity, reducing natural variability and potentially creating false trends. Figure A.4.1 in Appendix A4 shows some of the effect, where the σ of the ξ1 parameter decreases. We acknowledge these limitations but given the project's focus on a single point location and constraints on in-depth climate modelling, we consider this approach acceptable.

5.4.2. Precondition

During a field trip in June 2001, in connection with landslide hazard assessment, recent surface cracks were discovered at the edge of Þófi and Neðri-Botnar (Jensen, 2001. In the autumn 2001, a 30 m long crack formed in Nautaklauf in Botnabrún during an extreme rainfall event. Movement there did not lead to large-scale landslides, but a year later, specifically in November 2002, new cracks opened in Botnabrún following a prolonged wet season, most of them in the area between Skuldarlækur and Nautaklauf. This movement led to two debris flows from the edge just west of Búðará (Figure 5.4.1). Old reports also discuss cracks forming in the year 1925 in the area. Furthermore, sediments from four large landslides were found in survey pits in Seyðisfjörður (Knudsen & Larsen, 2013). They have been dated between 4500 BP to 580 AD (Gylfadóttir *et al.*, 2019). The largest landslide events expected in Seyðisfjörður are assumed to be ~100,000 m[3] (Gylfadóttir *et al.*, 2019). In the landslide inventory the recoded events in Seyðisfjörður that occurred during the 20th and

21st century are assumed to be dated correctly, but time during the day is often not known. Table 5.4.1 lists the landslide hazard in Seyðisfjörður, based on the recent hazard assessment (Gylfadóttir *et al*., 2019).

Table 5.4.1 Definition of landslide hazards in Seyðisfjörður

Landslide return period	Type of event	Size of event	Vol. (m³)	Length (m) or area (m²)	Rainfall duration
10 yr	Debris flow	Small*	$<10^2$	100 m	24h – 72h
500–1000 yr	Debris induced landslide	Medium**	5×10^4–2.5×10^5	$2\times10^{3\text{-}4}$ m²	3-5 days
2500 yr	Debris induced landslide	Medium-large**	2.5×10^5–1×10^6	$2\times10^{4\text{-}5}$ m²	>7 days

* Jakob (2005) ** Fell (1994) in McColl & Cook (2023)

In September 1981 debris flows fell from Botnabrun and from Imslandsgil on the south side of Seyðisfjörður, while the same weather conditions also triggered a debris flow from Bjólfur mountain, situated opposite (on the northern side of the fjord). In October 2001 a series of debris flows occurred both on the south side, from Þófi all the way to Hádegisá and on the north side under the mountain Bjólfur. In total, there are eleven recorded landslides, ranging from debris to mudflows on 2 October. Road damage and road closures followed this landslide cycle. In June 2002 a mudflow fell from Bjólfur mountain and, during November of the same year, eight other debris- and mud flows were recorded. In December 2015 another landslide cycle hit the town of Seyðisfjörður, both on the south and on the north side of the fjord.

Map of landslides in Seyðisfjörður where these events are highlighted is in Figure 5.4.1. The thick red lines and dots represent events that, using the methodology applied here, would classify as possible precursors to larger events. The map also shows finer red lines where the large landslide of December 2020 occurred (slightly left of the middle on the map). The large landslide was one of the last events in that cycle, and other fine lines on the map denote smaller events.
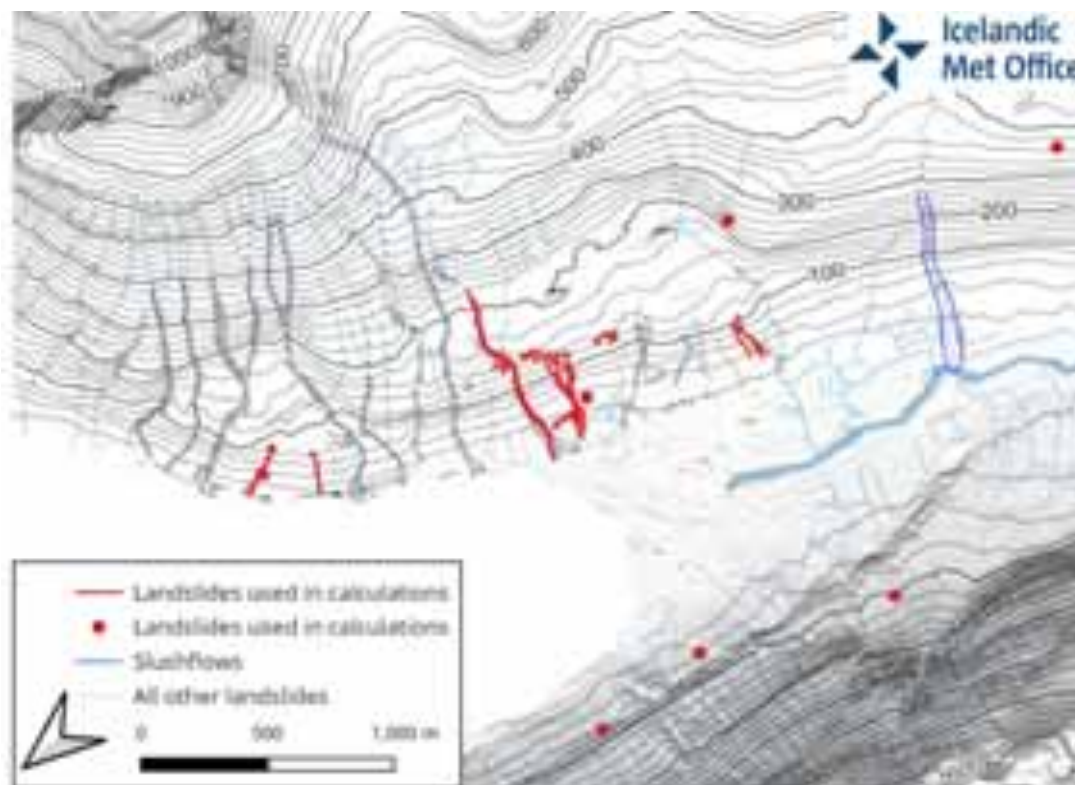
Figure 5.4.1 Map showing landslides and a slush flow in Seyðisfjörður. Thick red lines and dots represent the events used in calculations. Fine red lines are other events. The dark blue line depicts the outline of a slush flow. For joint-probability analysis, only landslide dates are used.

5.4.3. IDF calculations

IDF (intensity duration frequency) curves for filtered rain (Table 5.4.2) were calculated and RPs for different rainfall intensity durations estimated. A time window of five days was selected as the minimum time separating two values in a timeseries. It is a realistic interval due to extreme precipitation being associated with large weather systems, and thus a synoptic timescale is appropriate to ensure independent events. Furthermore, the same interval has been used for extreme analysis of winds in Iceland (Petersen, 2015). Several methods exist to determine the ideal threshold for a timeseries, but in this study, the commonly used 90th percentile is used as a threshold as for previous studies in Iceland (Massad *et al.*, 2020, 2022).

Table 5.4.2 IDF for liquid precipitation (rain) calculated for a rolling sum of different durations and frequencies.

Rainfall duration in hours	Return period (years)								
	2	5	10	25	50	100	500	1000	2000
	Rolling sum of rainfall (mm)								
3 h	10	15	19	24	27	31	40	44	47
6 h	24	33	40	51	59	68	89	99	109
12 h	50	67	80	99	114	130	170	189	208
24 h	92	121	144	179	208	239	321	361	404
48 h	147	187	219	265	303	343	446	495	548
120 h	243	299	344	407	458	511	648	712	780
168 h	302	349	384	432	467	503	585	621	657

5.4.4. Joint extreme events

The aim was to define the extreme rainfall conditions that lead to debris flows, as defined by Hungr *et al*. (2014), which is very rapid to extremely rapid surging flow of saturated debris in a steep channel. The small debris flows in Seyðisfjörður have proven to be an indicator of possible larger events, but small events triggered by intensive rainfall without high saturations of the ground are not likely to lead to larger events. Therefore, the analysis aimed at defining the situation where smaller events indicate the beginning of a larger event.

The joint extreme events analysis explained in section 3.2 (the multivariate method) was applied on a timeseries with daily values with rolling sums of 1-, 2-, 3- and 5-days rain and antecedent rainfall (Figure 5.4.2). Therefore, for each pair the selected drivers are different rainfall intensity durations and scaled normalised API (sNAPI). As discussed in section 3.1 the API is assumed to represent the state of the soil saturation and by joining it to different intensity durations, joint extreme pairs where selected using the MATLAB (MathWorks®) code discussed in section 3.2 since the rain cannot be considered to trigger the API that falls before it happens. When each pair of extreme events had been defined, the recorded landslides were linked to the sample.
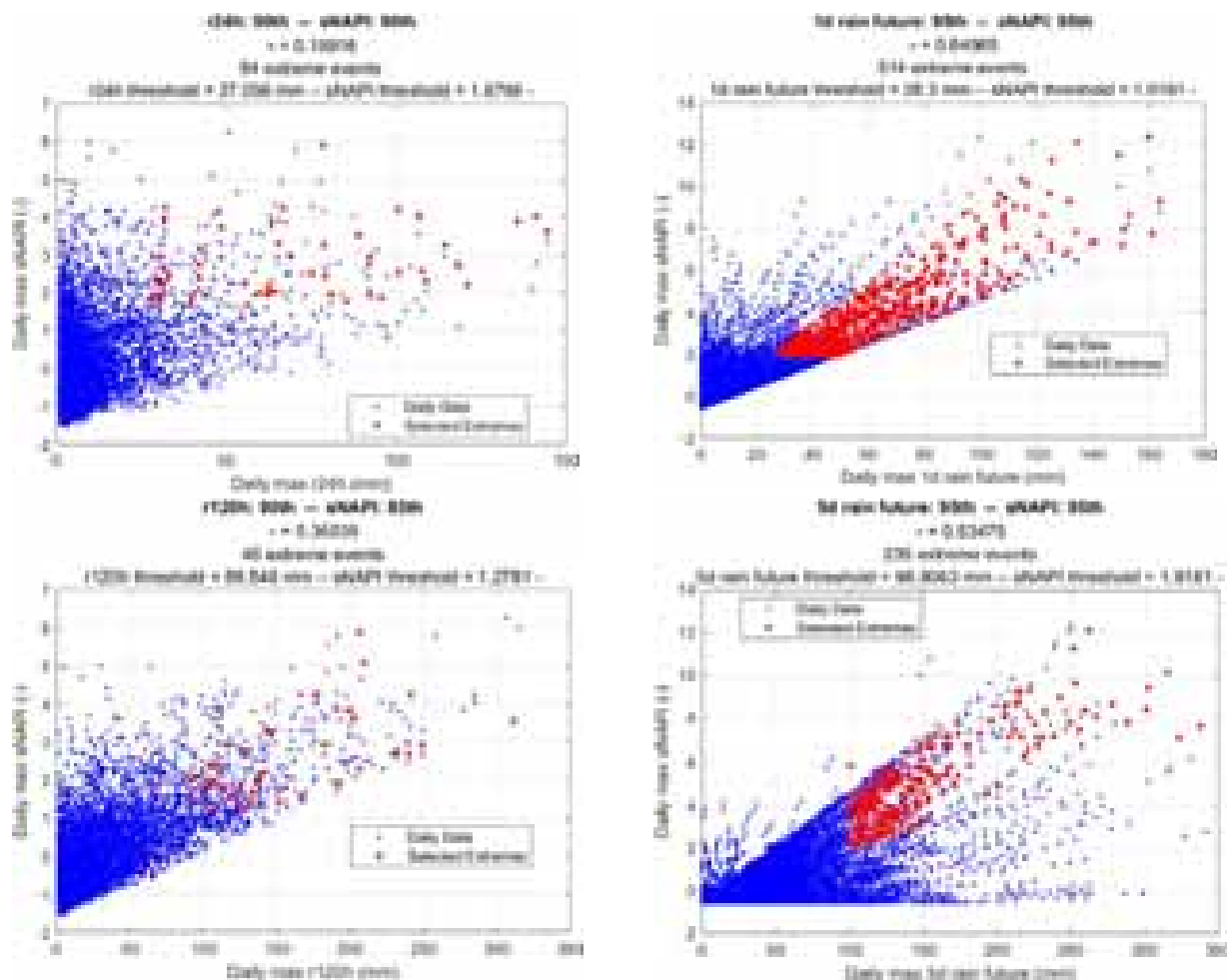

Figure 5.4.2 Joint extreme events. Scatter plot of all pairs of rainfall and sNAPI (blue) and pairs of joint extreme events (red). (a) 1-day Baseline condition; (b) 1-day Future climate change scenario (c) 5-day Baseline condition; (d) 5-day Future climate change scenario.

The method picked up several known events, which are listed in (Table 5.4.3). Several events in the inventory did not match the joint extremes of the 1-day and 5-days rainfall events. In some cases, this can be explained by the fact that the landslide inventory does not define cause correctly and intense rainfall was not the cause e.g., 21 August 2003, where recorded rainfall is 5.8 mm in 12 hours (see Table A4.1 in Appendix 4). Preconditioned circumstances must have been in favour of erosion on the hillside and extreme rainfall was not needed to trigger the landslides. In three other cases landslides occurred during extreme rainfall but low API. Since this analysis focuses on defining conditions that can accelerate to large landslides, this is considered acceptable.

Table 5.4.3 Results of the extreme event analysis for the selected debris flows. The first column shows the date (dd.mm.yyyy) of the landslide event, and the following are the dates of the extreme events for 24 h, 48 h, 72 h and 120 h precipitation when API was high, respectively.

Date landslide	Extreme date 24 h	Extreme date 48 h	Extreme date 72 h	Extreme date 120 h
25.9.1981	25.9.1981	25.9.1981	26.9.1981	
1.10.2001	1.10.2001	2.10.2001	3.10.2001	1.10.2001
2.10.2001	1.10.2001	2.10.2001	3.10.2001	1.10.2001
2.10.2001	6.10.2001			
17.6.2002	17.6.2002	18.6.2002	19.6.2002	
11.11.2002	11.11.2002	12.11.2002	12.11.2002	
24.11.2002	24.11.2002	28.11.2002		
23.11.2002	24.11.2002			
25.11.2002	24.11.2002	28.11.2002	29.11.2002	
24.11.2002	28.11.2002			
25.11.2002	28.11.2002			
28.12.2015	28.12.2015			

5.4.5. Joint probability

The results of the joint probability analysis show that of 54 joint events identified, the maximum 1-day rainfall of 144.4 mm is approximately associated with a 78-year RP. The maximum RP for antecedent rainfall (sNAPI) is estimated to be around 260 years. Notably, the JRP is approximately 134 years for the maximum rainfall. The 1-day maximum rainfall intensity is estimated to become more frequent as well as the combination of maximum 1-day rainfall and extreme antecedent rainfall with a 42-year RP. The maximum of the 46 joint extreme events the maximum 5-day rainfall of about 311 mm had a RP of about 88 years and the maximum antecedent rainfall about 70 years, whereas the JRP of the maximum rainfall was about 103 years. This combination is expected to become much more frequent with a JRP of 18 years for the maximum 5-day rainfall intensity.

Table 5.4.4 Sample scenarios for joint extreme wind and precipitation events in Múlaþing – Seyðisfjörður derived from joint probability analyses.

Scenarios	Return period of rain (year)	Return period sNAPI (year)	Joint return period (year)	
			Baseline	Future
1. Low daily rainfall and low daily sNAPI	2	2	4.4	2.8
2. High daily rainfall and low daily sNAPI	50	2	68.0	50.1
3. Low daily rainfall and high daily sNAPI	2	50	68.0	50.1
4. High daily rainfall and high daily sNAPI	50	50	206.2	72.0
5. Low 5-day rainfall and low daily sNAPI	2	2	3.2	2.7
6. High 5-day rainfall and low daily sNAPI	50	2	52.8	50.1
7. Low 5-day rainfall and high daily sNAPI	2	50	52.8	50.1
8. High 5-day rainfall and high daily sNAPI	50	50	109.2	71.5

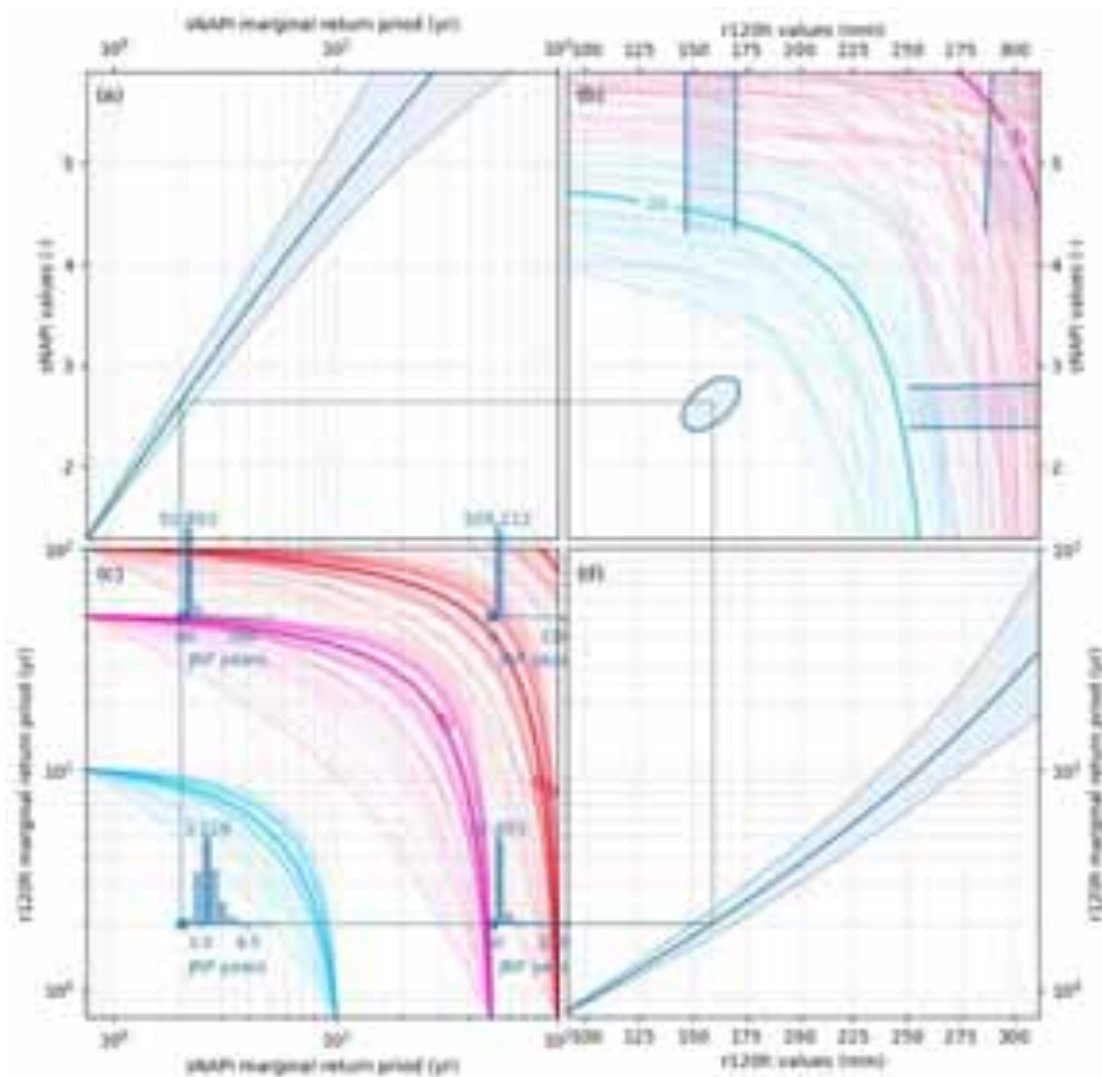Figure 5.4.3 Plots of the 20th, 50th and 80th posterior marginal probabilities across return periods for antecedent precipitation (sNAPI) (a) and 120-hour precipitation (d) under historical conditions. The distribution of Joint Return Periods (JRPs) across rain and sNAPI values is depicted in panel (b). JRPs for four random joint extreme events are displayed in panel (c). The contour lines in panels (b) and (c) represent the JRP in years. The bold lines of the contour indicate the median JRP, while the remaining lines represent random draws from the posterior distribution, providing an understanding of the variability.

The aim of Figure 5.4.3 and Figure 5.4.4 is to illustrate the relationship between JRPs specified in terms of driver values (i.e., 120 hours (5-days) rainfall and sNAPI in this case) and JRPs specified in terms of driver marginal RPs, i.e. the return period for a given rainfall value. Figure 5.4.3 represents historical data and Figure 5.4.4 is the projected future data. We start with our statistical model, which, to recap, describes the distribution of bivariate extreme values using marginal GPD linked by a Gumbel copula. This model is specified by the free parameters σ1, σ2, ξ1, ξ2 and θ, which form a five-dimensional parameter space.

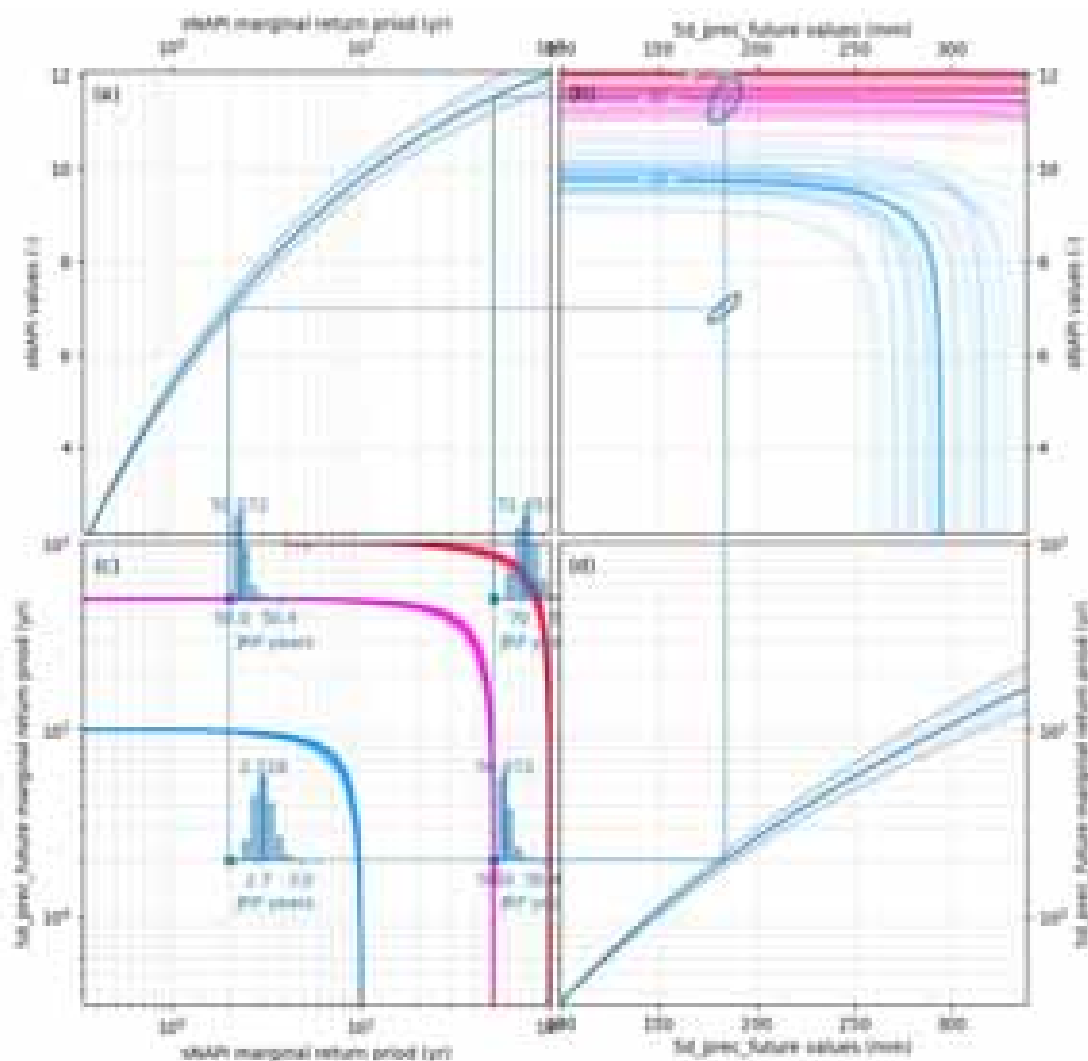Figure 5.4.4 Plots of the 20th, 50th and 80th posterior marginal probabilities across return periods for antecedent precipitation (sNAPI) (a) and 5-day precipitation (d) under future conditions. The distribution of Joint Return Periods (JRPs) across rain and sNAPI values is depicted in panel (b). JRPs for four random joint extreme events are displayed in panel (c). The contour lines in panels (b) and (c) represent the JRP in years. The bold lines of the contour indicate the median JRP, while the remaining lines represent random draws from the posterior distribution, providing an understanding of the variability.

5.4.6. Identifying causal relationships

Typically, landslides in Seyðisfjörður occur in cycles. At the same time, more than one event occurs in both surroundings, north and south hillslopes. In this case, the same weather conditions are responsible for the cycle of activity, and heavy rain is the recorded cause in the inventory database. In Seyðisfjörður, debris flows occur often at the same time. For instance, debris flows can occur from both sides of the hillslopes above the town due to prevailing weather conditions. In addition, spontaneous shallow mud or debris slides can occur, and they are not confined to a channel, making them more difficult to forecast beforehand, if not for the formation of cracks. These factors are the precondition of larger and deeper-seated landslides, as witnessed in Seyðisfjörður in December 2020. Intensity duration values from

Table 5.4.2 (above) were selected for the appropriate return period of the predefined landslide hazard in Table 5.4.5.

*********************************   *********************************

Table 5.4.5 Defined landslide events of three different sizes with rainfall IDF and joint extreme thresholds

Landslide return period	Rainfall duration	Rain return period, IDF	Joint extreme threshold	Rain return period, IDF	Joint extreme threshold
		Historical		Projected	
10 yr	24h–72h	150–300	24h ~ 27|1.7 72h ~150|1.7	180–360	1day ~ 28|1.9
500–1000 yr	3–5 days	500–600*	120h ~ 87|1.3	575–712	120h ~99|1.9
2500 yr	>7 days	>700		>800	

*14.–18. December 2020, a total of 569.9 mm was measured in Seyðisfjörður.

Gylfadóttir (2022 unpublished) calculated possible pressure (kPa) caused by modelled landslides above a critical part of the town of Seyðisfjörður with and without extended mitigation (Figure 5.4.5). The data was made available for the MEDiate project, and it defines the load that two types of landslides of different sizes, 12,000 m³ and 60,000 m³ can be expected to exert on the houses below the hillside. The return period of each landslide has been estimated (Table 5.4.5) by the landslide inventory and geological analysis in the area (Gylfadtóttir *et al.*, 2019).

A medium-sized landslide is $\geq$12,000 m^3 with a return period of 500–1,000 years.

| a) Without limited mitigation | b) With extended mitigation |
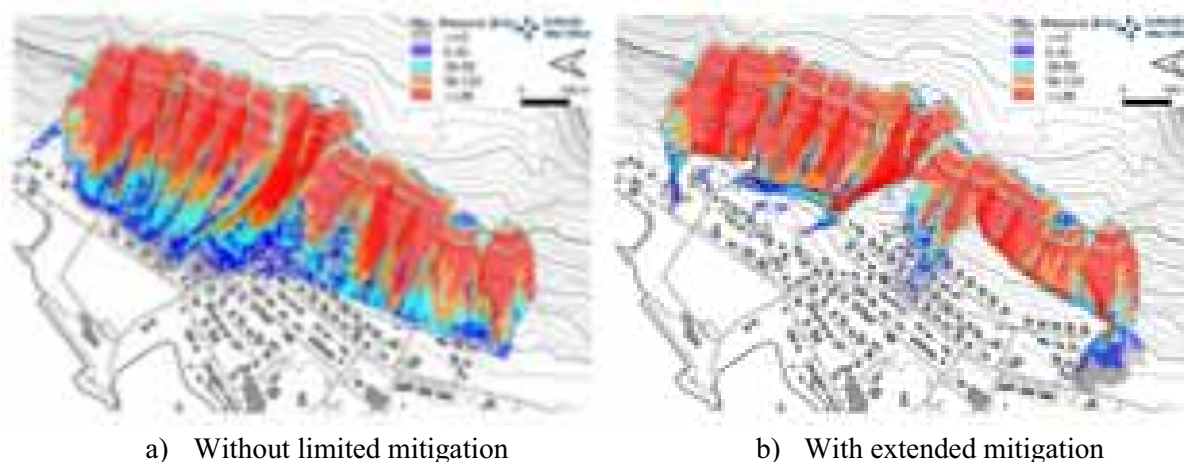
A medium- to large-sized landslide is $\geq$60,000 m^3 with a return period of 2,500 years.

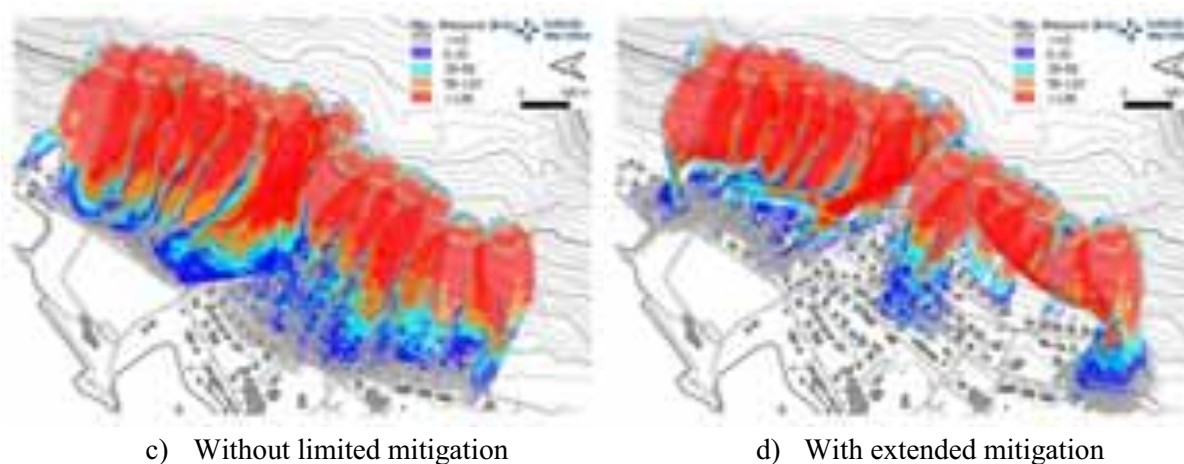| c) Without limited mitigation | d) With extended mitigation |

Figure 5.4.5 Four ensembled scenarios of landslide hazard events: (a) 12,000 m^3 medium-sized landslides with a return-period of 500–1,000 years with limited mitigation; (b) with extended mitigation; (c) 60,000 m^3 medium to large-sized landslides with a return period of 2,500 years with limited mitigation; and (d) with extensive mitigation measures.

The small events (Table 5.4.1) are those that can be seen and confirmed by the joint extreme method. The number of medium to large events is too low to confirm a direct connection between the extreme rainfall and API. However, the analysis gives an indication on what rainfall pattern can be critical and possibly lead to medium to large landslides.

The hillside above the town of Seyðisfjörður is monitored by extensive network of instruments. Adding this information to extreme rainfall patterns and correlation to antecedent rainfall could be valuable in monitoring medium to large landslides.

6   DISCUSSION AND CONCLUSIONS

This study focuses on the complex interplay of multi-hazards, revealing intricate dependencies that are crucial for understanding and managing risk. The results from the four testbeds challenge traditional natural-hazard management approaches, which often focus on single hazards, underscoring the need for integrated hazard assessment strategies. A key challenge was integrating diverse datasets from various sources. Successfully managing these challenges was pivotal in creating a comprehensive hazard assessment model. This achievement highlights the importance of advanced data analysis techniques in contemporary disaster risk

management. However, the study faced challenges in implementation, particularly in terms of data availability and the complexity of integrating different modelling approaches. These issues highlight the need for continued investment in data collection and methodological research in the field of interacting natural hazards.

The inclusion of diverse European testbeds in the study underlines the importance of regional variability in disaster risk management. Each testbed provided insights into how different geographical and climatic contexts can influence hazard interactions. This diversity of data enriches the findings and enhances their applicability across various European settings.

The study introduced innovative methodologies for assessing multi-hazard impacts, particularly in modelling interactions between different types of hazards. These methodological advancements are crucial for the ongoing evolution of risk assessment models (WP3), and they can be applied in other contexts to improve disaster preparedness and response. The methodologies and insights derived from this report are instrumental in creating sophisticated, data-driven tools for more accurate predictions and effective mitigation of multi-hazard risks (Lee *et al.*, 2024).

The project's insights into the impact of climate change on hazard timing, intensity and interactions are particularly significant. The findings align with global climate trends, showing an increase in the frequency and severity of natural hazards. This aspect of the research provides a critical foundation for developing climate-resilient disaster management strategies, as considered in WP3.

The results from the four testbeds also touch on the socio-economic implications of risks occurring due to multi-hazard interactions. Understanding the societal impact of interacting natural hazards, including economic losses and human displacement, is vital for developing holistic risk management strategies. This perspective ensures that disaster risk management is not only about predicting and mitigating hazards, but also about protecting communities and their livelihoods. Another output of this research is potential role in raising awareness and educating the public about multi-hazard risks. By disseminating the findings and insights, the project can contribute to a more informed public, better equipped to understand, and to respond to the risks associated with natural hazards.

Work-package two sets the stage for future research in several key areas. This study has significantly advanced our understanding of multi-hazard interactions, focusing on four distinct European testbeds: Oslo, Nice, Essex, and Múlaþing. Each testbed provides unique insights into the complex relationships between different natural hazards within diverse geographical and climatic conditions. These findings are imperative for developing targeted and effective disaster risk management strategies in these regions and beyond.

Oslo testbed: Compounding flooding, rainfall-triggered river floods and mass movements
Among the three pairs of multi-hazard events in Oslo, compounded coastal and riverine flood events emerge as some of the most frequently occurring hazards, resulting in detrimental effects on populations and assets. Advanced modelling within the project has revealed that the frequency and severity of such events are likely to increase in the future, underscoring the need for integrated urban planning and flood defences. Furthermore, the project identifies associations between rainfall-induced flooding and landslides/quick clay landslides. These findings suggest a necessity for robust infrastructure planning that simultaneously addresses the co-occurrence of various combinations of hazards, signifying a significant shift from traditional, singular hazard-focused strategies to multi-hazard-based approaches.

Nice testbed: Extreme heat and drought, extreme rainfall-landslides and compound flooding
The Nice testbed provided critical insights into compound heatwaves and drought (COHWD) events, a direct consequence of global warming. This region, with its Mediterranean climate and distinctive topography, is witnessing a notable increase in the frequency of extreme weather events. Projections suggest a decrease in

annual precipitation, leading to an escalation in winter drought occurrences. This study identifies anticipated changes in the spatial distribution of COHWD events, which are poised to become more frequent in the future. Furthermore, the project's analyses project an increase in the frequency and severity of compound coastal and riverine flood events, alongside landslides triggered by riverine flooding. In conclusion, the project underscores the imperative for response programs, such as the provision of water and food relief, the implementation of advanced removal of livestock from drought-affected regions, and the promotion of alternative livelihood strategies and to develop adaptive management strategies that cater to the dual threat of compound heatwaves and drought, exacerbated by climate change.

Essex Testbed: Wind, rainfall, temperature, and compounding flooding

In Essex, the project focuses on the interdependencies among various combinations of extreme winds, temperatures, heavy rainfall, and coastal processes. The findings reveal an increasing tendency for these hazards to coincide, with the frequency of spatially compounded events—extreme wind and rainfall—expected to rise in the future. Although the number of compound coastal and riverine flood, as well as, extreme heat and rainfall events may remain relatively low, projections indicate that their intensities will be substantially high. These insights are crucial for coastal management in Essex, emphasising the importance of reinforcing coastal defences and developing early warning systems for multi-hazard events stemming from different combinations of extreme wind, temperature, rainfall, river discharge, and surge.

Múlaþing Testbed: Landslides, snow avalanches and hydro-meteorological hazards

The Múlaþing region in Iceland, with its unique geological and climatic conditions, has yielded valuable data on landslide and snow avalanche hazard influenced by hydro-meteorological factors. The testbed's findings highlight the critical role of the combinations of intensity and antecedent rainfall in triggering landslides. Despite this, no association was observed between rainfall-triggered snowmelt and landslides/snow avalanches, possibly due to the scarcity of recorded events and the ambiguous nature of preconditions, particularly since slush flows are highly localized occurrences. The documented snow avalanche events were categorized as dry avalanches, with a strong correlation noted between intense snowfall and antecedent precipitation (snow). Nevertheless, the meteorological conditions identified in the analysis are anticipated to occur less frequently in the future. Given these projections, there is a pressing need for Múlaþing to enhance monitoring and forecasting efforts targeting these specific triggers and to integrate them into regional land-use planning and disaster preparedness strategies.

Wider implications and future research directions

The outcomes of deliverable 2.2 have broader implications beyond the testbed regions. They underscore the need for a paradigm shift in disaster risk management – from single hazard-specific approaches to more integrated, multi-hazard perspectives. This shift is crucial in the face of climate change, which is altering the frequency, intensity, and interdependencies of natural hazards. For future research, there is a clear need to refine the methodologies developed in the MEDiate project and extend them to other regions with different climatic and geographical characteristics. Additionally, the project sets a precedent for the development of more sophisticated, integrated decision-support systems that can predict and mitigate risks associated with multi-hazard events more effectively. In conclusion, the MEDiate project's findings from the four testbeds provide a roadmap for developing more resilient and adaptive disaster risk management strategies in diverse European contexts. These strategies must account for the complex interplay of multiple hazards and the evolving nature of these risks under the influence of climate change.

7 REFERENCES

Arnalds, Þ., Sauermoser, S., Jóhannesson, T., & Jensen, E. (2002). *Hazard zoning for Seyðisfjörður*. Icelandic Meteorological Office. http://www.vedur.is/media/vedurstofan/utgafa/greinargerdir/2002/02010.pdf

Austurbrú. (2024). *Samband sveitarfélaga á Austurlandi - SSA: Austurbrú.* https://austurbru.is/ssa/sveitarfelog-a-austurlandi/ accessed in February 2024.

Balkema, A. A., & De Haan, L. (1974). Residual life time at great age. *The Annals of probability*, 2(5), 792-804.

Bateni, M. M., Martina, M. L., & Arosio, M. (2022). Multivariate return period for different types of flooding in city of Monza, Italy. *Natural Hazards*, 114(1), 811-823.

BDMvT (2024). Mouvements de terrain. https://www.georisques.gouv.fr/donnees/bases-de-donnees/base-de-donnees-mouvements-de-terrain accessed in January 2024.

Berg, P., Bozhinova, D., & Photiadou, C. (2021). *Copernicus Climate Change Service C3S_424_SMHI_2021SC3-Climate explorer for the Water Sector*. https://cds.climate.copernicus.eu/cdsapp#!/software/app-hydrology-climate-explorer?tab=overview

Bertrand, N., Abily, M., Lambert, M., & Delestre, O. (2022). Benefit of coupling 1d-2d model over an urban area to assess runoff during a storm event. *In Advances in Hydroinformatics*: Models for Complex and Global Water Issues—Practices and Expectations (pp. 315-328). Singapore: *Springer Nature Singapore*

Bi, W., Tian, L., Li, C., & Zhang, S. (2023). Multi-hazard joint probability distribution model for wind speed, wind direction and rain intensity. Science China Technological Sciences, 66(2), 336-345.

Björnsson, H., Ólafsdóttir A. H., Sigurðsson, B. D., Katrínardóttir, B., Davíðsdóttir, B., Gunnarsdóttir G., Aðalgeirsdóttir, G. T., Sigurðsson G. M., Ögmundardóttir, H., Pétursdóttir, H., Bárðarson, H., Heiðmarsson, S., & Matthíasdóttir T. (2023). *Umfang og afleiðingar hnattrænna loftslagsbreytinga á Íslandi. Fjórða samantektarskýrsla vísindanefndar um loftslagsbreytingar*. Icelandic Meteorological Office.

BMT (2020). *Essex Pluvial Model Update Braintree*. For Essex County Council. Braintree and Witham September 2020.

Braud, I., Ayral, P. A., Bouvier, C., Branger, F., Delrieu, G., Dramais, G., ... & Vandervaere, J. P. (2016). *Advances in flash floods understanding and modelling derived from the FloodScale project in south-east France*. In 3rd European Conference on Flood Risk Management, Innovation, Implementation, Integration (FLOODrisk 2016) (Vol. 7, p. 04005).

Breiman, L. (2001). Random forests. *Machine learning*, *45*, 5-32.

Carpenter, B., Gelman, A., Hoffman, M.D., Lee, D., Goodrich, B., Betancourt, M., Brubaker, M.A., Guo, J., Li, P. and Riddell, A., 2017. Stan: A probabilistic programming language. *Journal of statistical software*, *76*.

Cohen, S., Brakenridge, G. R., Kettner, A., Bates, B., Nelson, J., McDonald, R., ... & Zhang, J. (2018). Estimating floodwater depths from flood inundation maps and topography. *JAWRA Journal of the American Water Resources Association, 54*(4), 847-858.

Coles, S. (2001). An introduction to Statistical Modeling of Extreme Values. London; *Springer*.De Angeli, Silvia, Bruce D. Malamud, Lauro Rossi, Faith E. Taylor, Eva Trasforini, Roberto Rudari (2022) A multi-hazard framework for spatial-temporal impact analysis. *International Journal of Disaster Risk Reduction*, 73, 2022, 102829, ISSN 2212-4209. https://doi.org/10.1016/j.ijdrr.2022.102829.

Copernicus (2020). Storm Alex, Copernicus. https://climate.copernicus.eu/esotc/2020/storm-alex#:~:text=Storm%20Alex%20(named%20Brigitte%20in,with%20at%20least%2015%20fatalities. Accessed March 2024.

Cordery, I. (1970). Initial loss for flood estimation and forecasting. *Journal of the Hydraulics Division*, 96(12), 2447-2466.

***************************************   ***************************************

Crozier, M. J., & Eyles, R. J. (1980). *Assessing the probability of rapid mass movement*. In Australia-New Zealand Conference on Geomechanics (3rd: 1980: Wellington, NZ) (pp. 2-47). Wellington, NZ: Institution of Professional Engineers New Zealand.

Crozier, M. J. (1986). Landslides: causes, consequences & environment. Croom Helm, London (1986), 252 pp.

Devoli, G., Bell, R., & Cepeda, J. (2019). *Susceptibility map at catchment level, to be used in landslide forecasting, Norway*. Norwegian Water Resources and Energy Directorate.

EAWS, 2022. Glossary – EAWS. The European avalanche warning services. https://www.avalanches.org/glossary/

Engen, Inger Karin, (1988). Flommen på Sør- og Østlandet i oktober 1987. NVE, V15. ISBN: 82-410-0028-6.

Eyring, V., Bony, S., Meehl, G. A., Senior, C. A., Stevens, B., Stouffer, R. J., & Taylor, K. E. (2016). Overview of the Coupled Model Intercomparison Project Phase 6 (CMIP6) experimental design and organization. *Geoscientific Model Development*, 9(5), 1937–1958. https://doi.org/10.5194/gmd-9-1937-2016.

Farahmand, A., & AghaKouchak, A. (2015). A generalized framework for deriving nonparametric standardized drought indicators. *Advances in Water Resources*, 76, 140-145.

Fell R (1994) Landslide risk assessment and acceptable risk. *Can Geotech J* 31:261–272

Fell, R., Corominas, J., Bonnard, C., Cascini, L., Leroi, E., and Savage, W. Z.: Guidelines for landslide susceptibility, hazard and risk zoning for land-use planning, *Eng. Geol.*, 102, 99–111, https://doi.org/10.1016/j.enggeo.2008.03.014, 2008a.

Fell, R., Corominas, J., Bonnard, C., Cascini, L., Leroi, E., and Savage, W. Z.: Guidelines for landslide susceptibility, hazard and risk zoning for land use planning, *Eng. Geol.*, 102, 85–98, https://doi.org/10.1016/j.enggeo.2008.03.022, 2008b.

Fischer, E. M., & Schär, C. (2010). Consistent geographical patterns of changes in high-impact European heatwaves. *Nature Geoscience*, 3(6), 398–403. https://doi.org/10.1038/ngeo866

Game, P., Wang, M., Audra, P., & Gourbesville, P. (2023). Flood modelling for a real-time decision support system of the covered Lower Paillons River, Nice, France. Journal of Hydroinformatics, 25(5), 1884-1908.

Gautam, P.; Kubota, T.; Sapkota, L.M.; Shinohara, Y. Landslide susceptibility mapping with GIS in high mountain area of Nepal:A comparison of four methods. *Environ. Earth Sci*. 2021, 80, 1–18.

Genest, C., & Rivest, L.P. (1993). Statistical Inference Procedures for Bivariate Archimedean Copulas. *Journal of the American Statistical Association,* 88(423), 1034-1043. https://doi.org/10.1080/01621459.1993.10476372

Ghanbari, M., Arabi, M., Kao, S. C., Obeysekera, J., & Sweet, W. (2021). Climate Change and Changes in Compound Coastal-Riverine Flooding Hazard Along the U.S. Coasts. *Earth's Future*, 9(5). https://doi.org/10.1029/2021EF002055

Ghanbari, M., Arabi, M., Obeysekera, J., & Sweet, W. (2019). A Coherent Statistical Model for Coastal Flood Frequency Analysis Under Nonstationary Sea Level Conditions. *Earth's Future*, 7(2), 162–177. https://doi.org/10.1029/2018EF001089

Ghosh, N. C., Jaiswal, R. K., & Ali, S. (2021). Normalized Antecedent Precipitation Index Based Model for Prediction of Runoff from Un-Gauged Catchments. *Water Resources Management*, 35(4), 1211–1230. https://doi.org/10.1007/s11269-021-02775-w

Gilleland, E., & Katz, R. W. (2016). extRemes 2.0: an extreme value analysis package in R. *Journal of Statistical Software*, 72, 1-39.Goodrich, B. (2017) https://groups.google.com/g/stan-users/c/hnUtkMYlLhQ/m/UZURBv2_AAAJ

Gori, A., Lin, N., Xi, D., & Emanuel, K. (2022). Tropical cyclone climatology change greatly exacerbates US extreme rainfall–surge hazard. *Nature Climate Change*, 12(2), 171-178.

Gringorten, I. I. (1963). A plotting rule for extreme probability paper. *Journal of Geophysical Research*, 68(3), 813-814.

Gudendorf, G., & Segers, J. (2010, May). Extreme-value copulas. In *Copula Theory and Its Applications: Proceedings of the Workshop Held in Warsaw, 25-26 September 2009* (pp. 127-145). Berlin, Heidelberg: Springer Berlin Heidelberg.

Gylfadóttir, S. (2022). *Four scenarios of landslide hazard events*. Icelandic Meteorological Office, unpublished.

Gylfadóttir, S. S., Jóhannesson, T., Helgason, Helgason, J. K., & Jónsson, M. H. (2021). *Endurskoðað hættumat fyrir svæðið frá Búðará að Skuldarlæk á Seyðisfirði* (minnisblað). Icelandic Meteorological Office.

Gylfadóttir, S. S., Helgason, J. K., Jóhannesson, T., & Hjartarson, Á. (2019). *Ofanflóðahaettumat fyrir Seyðisfjörð: Endurskoðun á hættumati fyrir byggðina sunnan Fjarðarár og svæði við Vestdalseyri. Greinargerð með hættumatskorti*. Icelandic Meteorological Office.

Hao, Z., AghaKouchak, A., Nakhjiri, N., & Farahmand, A. (2014). Global integrated drought monitoring and prediction system. *Scientific Data*, 1, 140001. https://doi.org/10.1038/sdata.2014.1

Hassoun, V., Martín, J., Migeon, S., Larroque, C., Cattaneo, A., Eriksson, M., ... & Miquel, J. C. (2014). Searching for the record of historical earthquakes, floods and anthropogenic activities in the Var Sedimentary Ridge (NW Mediterranean). *In Submarine Mass Movements and Their Consequences: 6th International Symposium* (pp. 571-581). Springer International Publishing.

Hauser, M., Gudmundsson, L., Orth, R., Jézéquel, A., Haustein, K., Vautard, R., ... & Seneviratne, S. I. (2017). Methods and model dependency of extreme event attribution: the 2015 European drought. *Earth's Future*, 5(10), 1034-1043.

Heggen, R. (2001) Normalized antecedent precipitation index. *Journal of Hydrologic Engineering* 6(5): 377-381. https://doi.org/10.1061/(ASCE)1084-0699(2001)6:5(377)

Hersbach, H., Bell, B., Berrisford, P., Biavati, G., Horányi, A., Muñoz Sabater, J., Nicolas, J., Peubey, C., Radu, R., Rozum, I., Schepers, D., Simmons, A., Soci, C., Dee, D., Thépaut, J-N. (2023): ERA5 hourly data on single levels from 1940 to present. *Copernicus Climate Change Service (C3S) Climate Data Store* (CDS), DOI: 10.24381/cds.adbb2d47

Hestnes, E., & Sandersen, F. (1998). *Slushflow hazard control. A review of mitigative measures*. NGI Publication; 203, Norwegian Geotechnical Institute. https://hdl.handle.net/11250/3082642

Huang C., Meslem A., Schweitzer J. (2023). *Adapting new concepts towards a multi-hazard platform for Oslo: Quick clay landslides in Alna case study* (Internal report). Department of Applied Seismology, NORSAR.

Hungr, O., Leroueil, S., & Picarelli, L. (2014). The Varnes classification of landslide types, an update. *Landslides*, 11, 167-194.

IPCC, 2022: Climate Change 2022: Impacts, Adaptation and Vulnerability. *Contribution of Working Group II to the Sixth Assessment Report of the Intergovernmental Panel on Climate Change* [H.-O. Pörtner, D.C. Roberts, M. Tignor, E.S. Poloczanska, K. Mintenbeck, A. Alegría, M. Craig, S. Langsdorf, S. Löschke, V. Möller, A. Okem, B. Rama (eds.)]. Cambridge University Press. Cambridge University Press, Cambridge, UK and New York, NY, USA, 3056 pp., doi:10.1017/9781009325844.

IPCC, 2013: Climate Change 2013: The Physical Science Basis. *Contribution of Working Group I to the Fifth Assessment Report of the Intergovernmental Panel on Climate Change* [Stocker, T.F., D. Qin, G.-K. Plattner, M. Tignor, S.K. Allen, J. Boschung, A. Nauels, Y. Xia, V. Bex and P.M. Midgley (eds.)]. Cambridge University Press, Cambridge, United Kingdom and New York, NY, USA, 1535 pp.

Ismail, T., Ahmed, K., Alamgir, M., Noor Kakar, M., & Fadzil, A. B. (2018). Bivariate flood frequency analysis using Gumbel copula. *Malaysian Journal of Civil Engineering*, *30*(2), 193-201.

Jakob M (2005). *A size classification for debris flows*. Eng Geol 79:151–161

Jensen, E. H., & Sönser, T. (2002). *Process Orientated Landslide Hazard Assessment for the South Side of Seyðisfjörður*. Icelandic Meteorological Office.

Jensen, E. H. (2001). *Hætta á skyndilegu jarðskriði úr brún Þófans á Seyðisfirði* (minnisbl. EHJ-2001/01). Icelandic Meteorological Office.

Kendon, M., & McCarthy, M. (2015). The UK's wet and stormy winter of 2013/2014. *Weather*, 70(2), 40-47.

Kendon, M., Eyre, J., & Penman, J. (2015). Absence of cold spells during the UK's stormy winter of 2013/2014. *Weather*, 70(2), 51-52.

Kennedy, C., Douglas, J., White, C., Roberts, M.J., Jensen, E., De Maio, F. (2023). *Multi-hazard and risk informed system for Enhanced local and regional Disaster risk management*. MEDiate D2.1

Knudsen, Ó. & Larsen, G. (2013). *Skriðuset í jarðvegi í Seyðisfjarðarkaupstað og Botnum*. Jarðfræðistofan/Jarðvísindastofnun HÍ, October 2013.

Komendantova, N., Mulder, F., Mihai, A., Danielson, M., Douglas, J., White, C., Gonzalez-Duenas, C., Cremen, G., Galasso, C., Bozzoni, F., Borzi, B., Paolo Gallorini, P., Cecile Barrere, C. (2023). *Validation of the MEDiate concept model through literature and workshops with stakeholders from testbeds*. MEDiate D1.1.

KSS. (2024, February 27). *Klimaframskrivninger - Norsk Klimaservicesenter*. https://klimaservicesenter.no/climateprojections?index=air_temperature&period=Annual&scenario=RCP85&area=C3

KSS (2022). *Klimaprofil Oslo og Akershus. Norsk klimaservicesenter*. https://klimaservicesenter.no/kss/klimaprofiler/oslo-og-akershus accessed December 2023.

Lee R., White C. J., Adnan M. S. G., Douglas J., Mahecha M. D., O'Loughlin F. E., Patelli E., Ramos A. M., Roberts M. J., Martius O., Tubaldi E., Van den Hurk B., Ward P. J., Zscheischler J. (2024). Reclassifying historical disasters: From single to multi-hazards, *Science of The Total Environment*, 912. https://doi.org/10.1016/j.scitotenv.2023.169120.

Li, X., Wei, Y., & Li, F. (2021). Optimality of antecedent precipitation index and its application. Journal of *Hydrology*, 595, 126027.

Ladson, T. (2024). *Antecedent Precipitation Index*. https://tonyladson.wordpress.com/tag/antecedent-precipitation-index/ visited March 2024.

Latif, S., & Mustafa, F. (2020). Bivariate flood distribution analysis under parametric copula framework: A case study for Kelantan River basin in Malaysia. *Acta Geophysica*, 68, 821-859.

Lindsay, R. K., Kohler, M. A. and Paulhus, J. L. H. (1975) *Hydrology for Engineers (2nd ed.)*. McGraw-Hill.

Liu, B., Siu, Y. L. & Mitchell, G. Hazard interaction analysis for multi-hazard risk assessment: A systematic classification based on hazard-forming environment. *Nat. Hazards Earth Syst*. Sci.16, 629–642 (2016). https://doi.org/10.5194/nhess-16-629-2016

loreabad6. (2019, November 25). *R, select rainfall events and calculate rainfall event total from time-series data*. Meta Stack Overflow. https://stackoverflow.com/questions/51371155/r-select-rainfall-events-and-calculate-rainfall-event-total-from-time-series-da/59031230#59031230

LUCAS (2023). *Land_use_and_land_cover_survey–Statistics explained*. https://ec.europa.eu/eurostat/statistics-explained/index.php?title=LUCAS_-_Land_use_and_land_cover_survey. Accessed in December 2023.

Ma, Q., Zavattero, E., Du, M., Vo, N. D., & Gourbesville, P. (2016). Assessment of high resolution topography impacts on deterministic distributed hydrological model in extreme rainfall-runoff simulation. *Procedia Engineering*, 154, 601-608.

Massad, A.-G. R., Björnsson, H., Petersen, G. N., & Þórarinsdóttir, T. (2023). *Influence of Iceland's changing climate on extreme precipitation and snow-fraction*. Icelandic Meteorological Office.

Massad 2022

Massad, A.-G. R., Petersen, G. N., Þórarinsdóttir, T., & Roberts, M. J. (2020). *Reassessment of precipitation return levels in Iceland*. Icelandic Meteorological Office.

McColl, S. T., & Cook, S. J. (2023). A universal size classification system for landslides. *Landslides 21, 111–120*. https://doi.org/10.1007/s10346-023-02131-6

Met Office Hadley Centre (2019): *UKCP Local Projections on a 5km grid over the UK for 1980-2080*. Centre for Environmental Data Analysis, date of citation. https://catalogue.ceda.ac.uk/uuid/e304987739e04cdc960598fa5e4439d0

Ming, X., Liang, Q., Dawson, R., Xia, X., & Hou, J. (2022). A quantitative multi-hazard risk assessment framework for compound flooding considering hazard inter-dependencies and interactions. *Journal of Hydrology, 607*. https://doi.org/10.1016/j.jhydrol.2022.127477

Muis, S., Maialen Irazoqui Apecechea, José Antonio Álvarez, Martin Verlaan, Kun Yan, Job Dullaart, Jeroen Aerts, Trang Duong, Rosh Ranasinghe, Dewi le Bars, Rein Haarsma, Malcolm Roberts, (2022): Global sea level change time series from 1950 to 2050 derived from reanalysis and high resolution CMIP6 climate projections. *Copernicus Climate Change Service (C3S) Climate Data Store (CDS)*. DOI: 10.24381/cds.a6d42d60 (Accessed in December 2023)

Nadim, F., Cepeda, J., Sandersen, F., Jaedicke, C., and Heyerdahl,H.: Prediction of rainfall-induced landslides through empiricaland numerical models. *Proceedings of the First Italian Workshop on Landslides (IWL 2009)*, Naples, Italy, 8–10 June, 206—215,2009.

Nawri, N., Pálmason, B., Petersen, G. N., Björnsson, H., & Þorsteinsson S. (2017). *The ICRA atmospheric reanalysis project for Iceland*. Icelandic Meteorological Office.

Nelsen, R. B. (2006) *An Introduction to Copulas (2nd ed.)*, Springer-Verlag, New York.

Nesheim, I., Furuseth, I. S., & Langaas, S. (2022). *Utredning: Organiseringsmodell for Alna- effektiv og langsiktig organisering for samordnet og kunnskapsbasert tiltaksarbeid i et byvassdrag*. Norsk institutt for vannforskning. https://niva.brage.unit.no/niva-xmlui/bitstream/handle/11250/2982451/7718-2022%20high.pdf?sequence=1

Ntegeka V., Salamon, P., Gomes, G., Sint, H., Lorini, V., Thielen Del Pozo, J., & Zambrano, H. (2013). *EFAS-Meteo: A European daily high-resolution gridded meteorological data set for 1990 - 2011*. Publications Office of the European Union. https://publications.jrc.ec.europa.eu/repository/handle/JRC86388

NVE (2023) - *The Norwegian Water Resources and Energy Directorate* – https://temakart.nve.no/ https://kartkatalog.nve.no/#wms accessed in October 2023.

NVE. (2024). *Kvikkleiresoner. Temakart.nve.no*. https://temakart.nve.no/tema/kvikkleire accessed in January 2024.

Park, M. H., & Kim, J. H. (2016). Estimating extreme tail risk measures with generalized Pareto distribution. *Computational Statistics & Data Analysis*, 98, 91-104.

Pickands III, J. (1975). Statistical inference using extreme order statistics. *The Annals of Statistics*, 119-131.

Petersen, G. N. (2015). *Greining á öfgaveðurhaeð frá sjálfvirkum vindmaelingum*. Icelandic Meteorological Office. Report VÍ-2015-004.

Rebetez, M., Mayer, H., Dupont, O., Schindler, D., Gartner, K., Kropp, J. P., & Menzel, A. (2006). Heat and drought 2003 in Europe: a climate synthesis. *Annals of Forest Science*, 63(6), 569-577.

Roald, L. A. (2021). *Floods in Norway* (No. 1/2021). Norges vassdrags- og energidirektorat

REMO. The Regional Climate Model REMO – RCM. https://www.remo-rcm.de/. Accessed in October 2023.

Sahal, A., & Lemahieu, A. (2011). The 1979 Nice airport tsunami: mapping of the flood in Antibes. *Natural hazards, 56*, 833-840.

Salvadori, G., Durante, F., De Michele, C., Bernardi, M., & Petrella, L. (2016). A multivariate copula-based framework for dealing with hazard scenarios and failure probabilities. *Water Resources Research*, *52*(5), 3701–3721. https://doi.org/10.1002/2015WR017225

Sklar, A. (1973). Random variables, joint distribution functions, and copulas. *Kybernetika, 9(6)*, 449-460.

**   **

Spencer, T., Brooks, S. M., Evans, B. R., Tempest, J. A., & Möller, I. (2015). Southern North Sea storm surge event of 5 December 2013: Water levels, waves and coastal impacts. *Earth-Science Reviews, 146*, 120-145

Stan Development Team (2024). Stan Modeling Language Users Guide and Reference Manual, 2.34. https://mc-stan.org

Steed, A. (2023). Reframing Development with Living Infrastructure: A Case Study of the South Essex Green and Blue Infrastructure (SEGBI) Strategy. *In Proceedings of the International Conference of Contemporary Affairs in Architecture and Urbanism-ICCAUA Vol. 6*, No. 1, pp. 373-382.

Taylor, K. E., Stouffer, R. J., & Meehl, G. A. (2012). An overview of CMIP5 and the experiment design. Bulletin of the American meteorological Society, 93(4), 485-498.

Tilloy, A., Malamud, B. D., Winter, H., & Joly-Laugel, A. (2019). A review of quantification methodologies for multi-hazard interrelationships. *Earth-Science Reviews*. https://doi.org/10.1016/j.earscirev.2019.102881

Teuling, A.J. A hot future for European droughts. *Nature Clim Change 8*, 364–365 (2018). https://doi.org/10.1038/s41558-018-0154-5

Tsunetaka, H. (2021). Comparison of the return period for landslide-triggering rainfall events in Japan based on standardization of the rainfall period. *Earth Surface Processes and Landforms*, *46*(14), 2984–2998. https://doi.org/10.1002/esp.5228

UNDRR. (2020). *Hazard definition and classification review: Technical report*. United Nations Office for Disaster Risk Reduction. https://www.undrr.org/publication/hazard-definition-and-classification-review-technical-report

Van Bebber, W.J. (1882). *Typische Witterungs-Erscheinungen*. Arch. Dtsch. Seewarte, Hamburg (1882).

Vehtari, A. (2017) *Extreme value analysis and user defined probability functions in Stan. Stan Case Studies*, Notebook Volume 4. https://mc-stan.org/users/documentation/case-studies/gpareto_functions.html

Vinet, F., Boissier, L., & Saint-Martin, C. (2016, October). Flashflood-related mortality in southern France: first results from a new database. *In 3rd European conference on flood risk management (FLOODrisk 2016)* (Vol. 7, p. 06001).

Wadey, M. P., Haigh, I. D., Nicholls, R. J., Brown, J. M., Horsburgh, K., Carroll, B., ... & Bradshaw, E. (2015). A comparison of the 31 January–1 February 1953 and 5–6 December 2013 coastal flood events around the *UK. Frontiers in Marine Science*, 2, 84.

Wanders, N., Bosmans, J. & Barbarossa, V. (2021). Futurestreams dataset. Utrecht University. https://public.yoda.uu.nl/geo/UU01/T7TVTQ.html

Ward, P. J., Winsemius, H. C., Kuzma, S., Bierkens, M. F., Bouwman, A., De Moel, H., ... & Luo, T. (2020). *Aqueduct floods methodology*. World Resources Institute, 1-28. https://www.wri.org/research/aqueduct-floods-methodology

Wu, C. Y., & Chen, S. C. (2013). Integrating spatial, temporal, and size probabilities for the annual landslide hazard maps in the Shihmen watershed, Taiwan. Natural Hazards and Earth System. *Sciences, 13(9)*, 2353-2367.

Wu, C. Y., & Yeh, Y. C. (2020). A landslide probability model based on a long-term landslide inventory and rainfall factors. *Water, 12(4),* 937.

Xi, D., Lin, N., & Gori, A. (2023). Increasing sequential tropical cyclone hazards along the US East and Gulf coasts. *Nature Climate Change*, *13*(3), 258-265.

Xie, W.-P., Yang, J.-S., 2013. Assessment of soil water content in field with antecedent precipitation index and groundwater depth in the Yangtze River Estuary. *J. Integr. Agric. 12 (4)*, 711–722. https://doi.org/10.1016/S2095-3119(13)60289-0.

Yule, E. L., Hegerl, G., Schurer, A., & Hawkins, E. (2023). Using early extremes to place the 2022 UK heat waves into historical context. *Atmospheric science letters, e1159*.

Zaiontz, C. (2020) *Real Statistics Using Excel*. www.real-statistics.com.

Zhang, S., Pecoraro, G., Jiang, Q., & Calvello, M. (2023). Definition of rainfall thresholds for landslides using unbalanced datasets: Two case studies in Shaanxi Province, China. *Water, 15(6)*, 1058.

Zhao, Y., Wei, F., Yang, H., & Jiang, Y. (2011). Discussion on using antecedent precipitation index to supplement relative soil moisture data series. *Procedia Environmental Sciences, 10*, 1489-1495.

Zheng, F., Westra, S., Leonard, M., & Sisson, S. A. (2014). Modeling dependence between extreme rainfall and storm surge to estimate coastal flooding risk. *Water Resources Research*, *50*(3), 2050–2071. https://doi.org/10.1002/2013WR014616

Zong, Y., & Tooley, M. J. (2003). A historical record of coastal floods in Britain: frequencies and associated storm tracks. *Natural hazards, 29*, 13-36.

Zscheischler, J., Martius, O., Westra, S., Bevacqua, E., Raymond, C., Horton, R. M., van den Hurk, B., AghaKouchak, A., Jézéquel, A., Mahecha, M. D., Maraun, D., Ramos, A. M., Ridder, N. N., Thiery, W., & Vignotto, E. (2020). A typology of compound weather and climate events. *Nature Reviews Earth and Environment* (Vol. 1, Issue 7, pp. 333–347). Springer Nature. https://doi.org/10.1038/s43017-020-0060-z
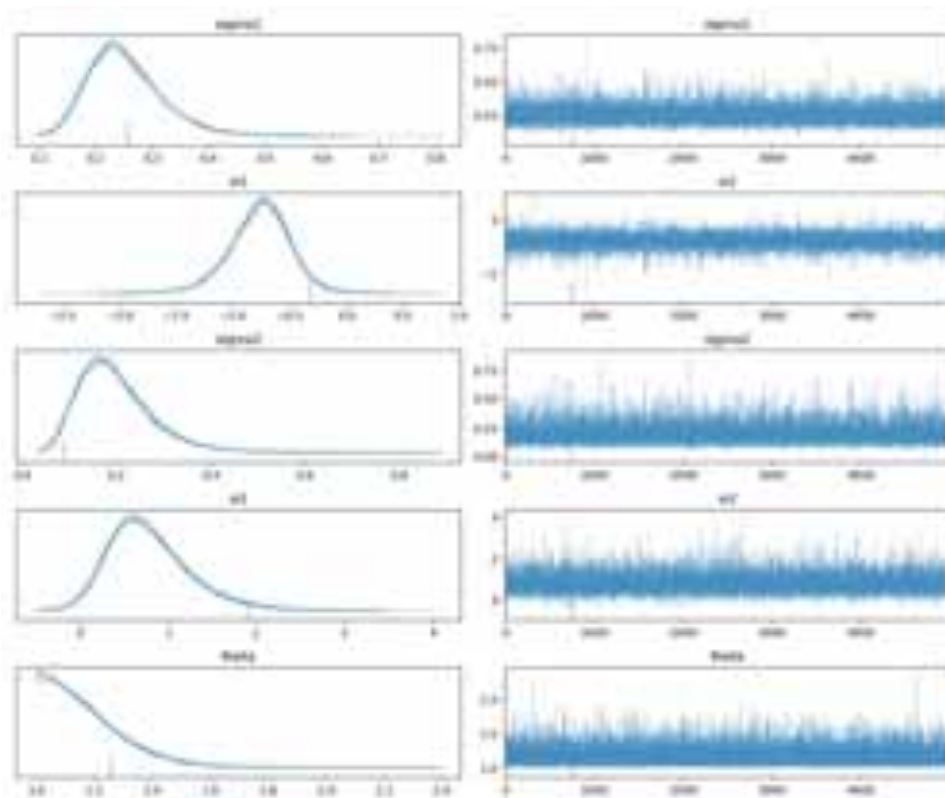
8 APPENDICES

8.1 Appendix A1: Oslo
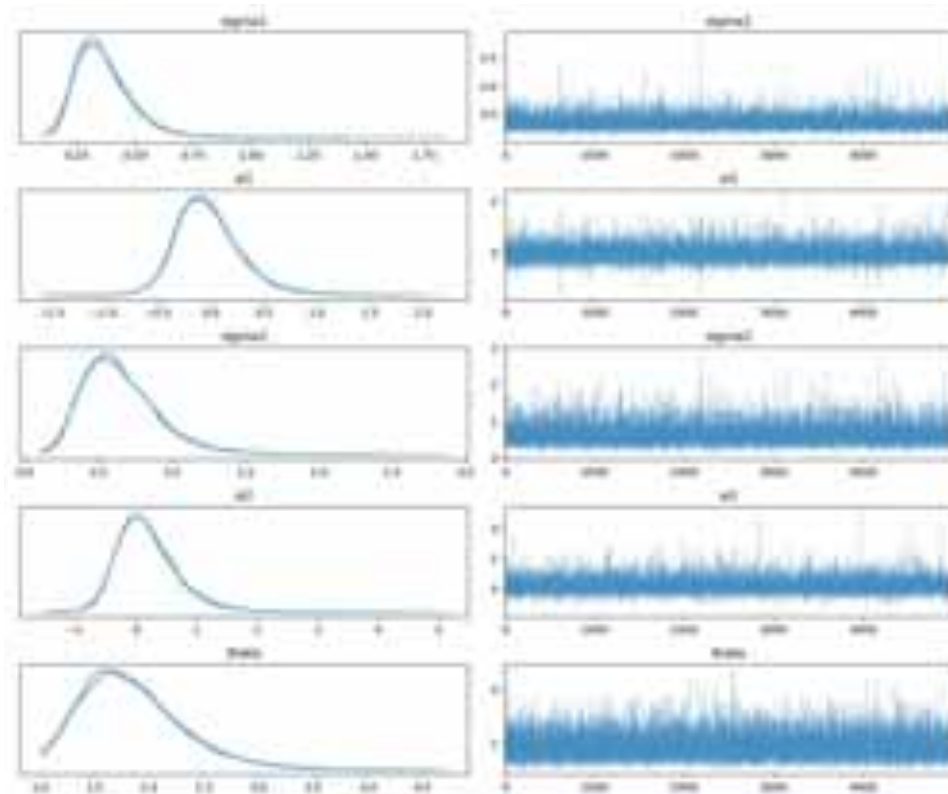
Figure A1.1. Trace plot for the five parameters of the joint distribution function used to analyse compound flood events in Oslo at baseline conditions. Here, x_{i1} and x_{i2} are the Generalised Pareto Distribution (GPD) shape parameters, and sigma1 and sigma2 are the GPD scale parameters for surge and river flow, respectively. 'Theta' is the Gumbel copula parameter.
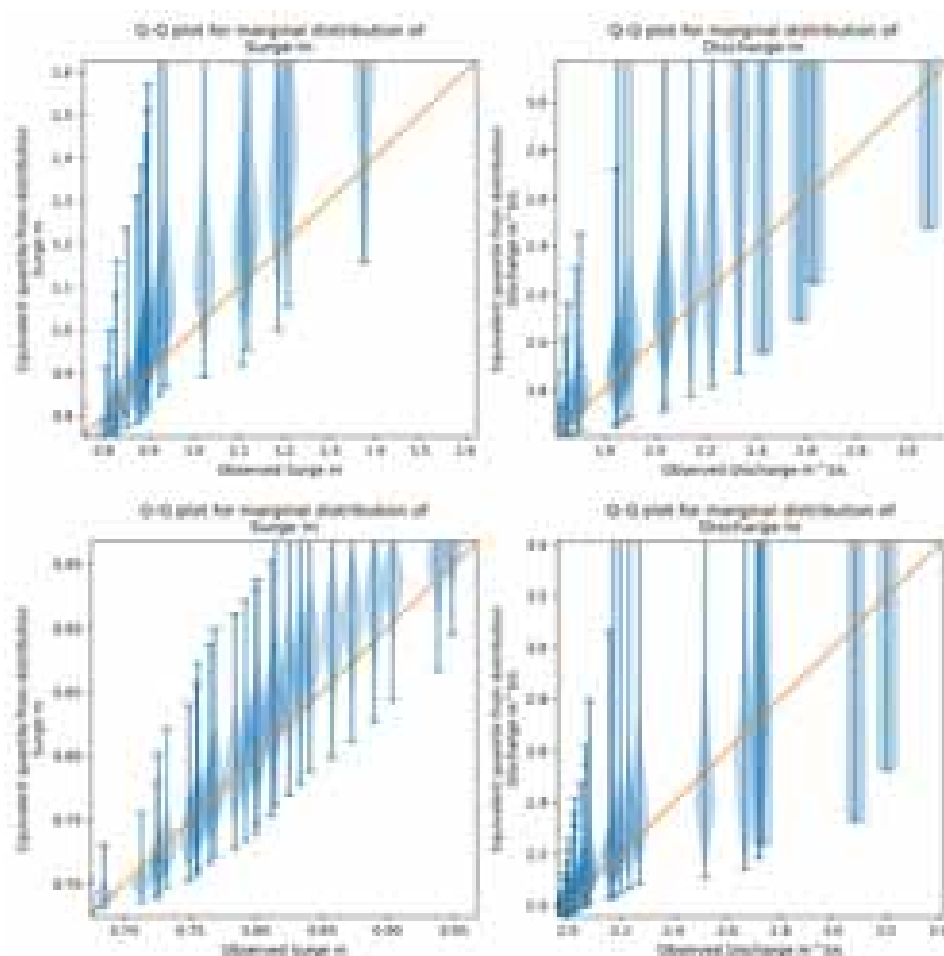
Figure A1.2. Trace plot for the five parameters of the joint distribution function used to analyse compound flood events in Oslo at future scenario. Here, x_{i1} and x_{i2} are the GPD shape parameters, and sigma1 and sigma2 are the GPD scale parameters for surge and river flow, respectively. 'Theta' is the Gumbel copula parameter.

********************************   ****************************

Figure A1.3. Model assessment results for analysing Oslo compound flood events. Bayesian Quantile-Quantile plots for the two (surge and river flow) marginal GPD, at baseline (upper) and future (lower) scenarios.

(a)

(b)
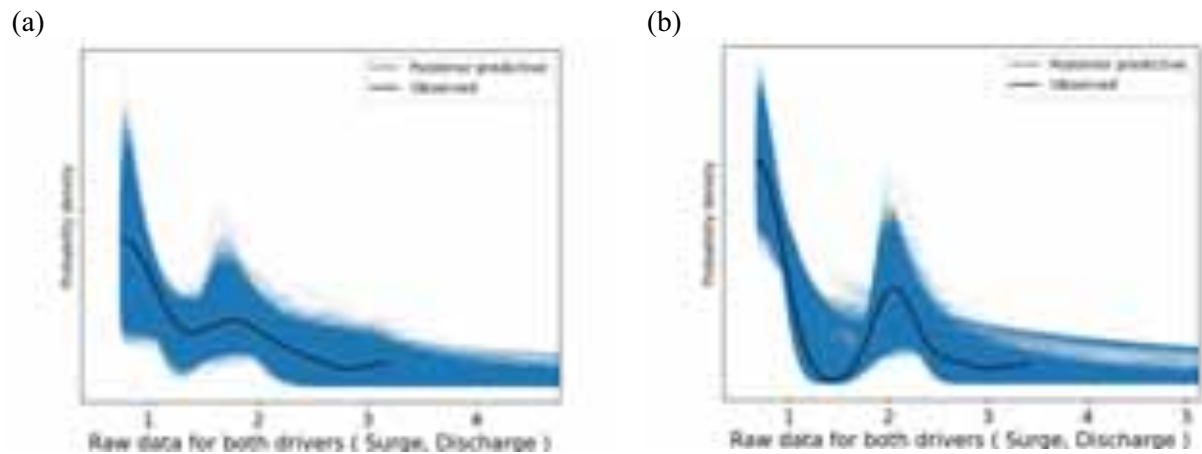
Figure A1.4. Model assessment results for analysing Oslo compound flood events. Posterior predictive checks at baseline (a) and future (b) scenarios

(a)

(b)
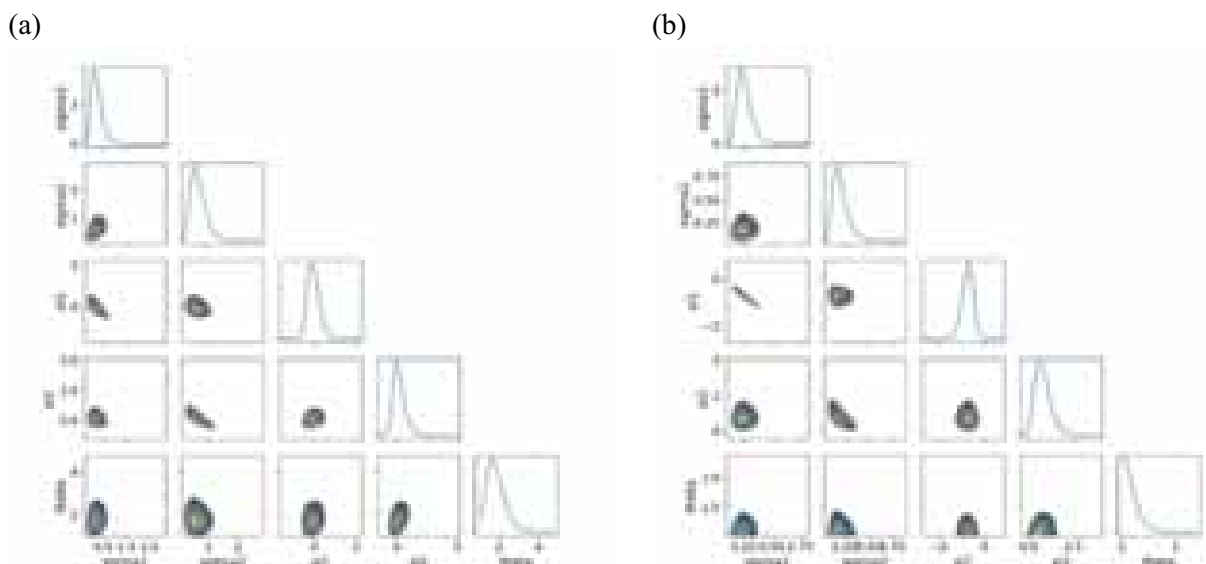
Figure A1.5. Model assessment results for analysing Oslo compound flood events. Corner plots for baseline (a) and future (b) scenarios.

******************************   ******************************

Table A1.1 Landslide events in Oslo region in the analysed period (1987-2023). Grey entries are outside the focused season.

Date	Type	Placename
26.3.1995	111	Ekeberg
29.5.1997	140	Grefsen - Kjelsås
30.7.1998	111	Grefsenkollveien
23.6.2000	142	Oslo S - Bekkelaget
23.6.2000	142	Oslo S - Bekkelaget
14.11.2000	111	Ljan - Holmlia
17.5.2001	111	Oslo S (delstr.) stasjon
2.3.2004	111	Sandermosen - Movatn
6.7.2007	111	Hagaløkkaveien
1.5.2009	111	Ljan - Holmlia
14.7.2009	111	Ljan - Holmlia
2.5.2010	111	Kjelsås - Sandermosen
7.4.2011	111	Konowsgate 5
19.11.2011	111	Bekkelaget stasjon
30.7.2014	111	(Grefsen) - (Alnabru) godsspor
1.11.2016	111	Oslo S (delstr.) stasjon
15.4.2019	111	Kjelsås - Sandermosen
6.6.2019	142	Måltrostveien
6.6.2019	142	Måltrostveien 23B
18.3.2022	111	Avkjøring Karihaugen
22.5.2023	111	Klemetsrud
8.8.2023	111	Åsland
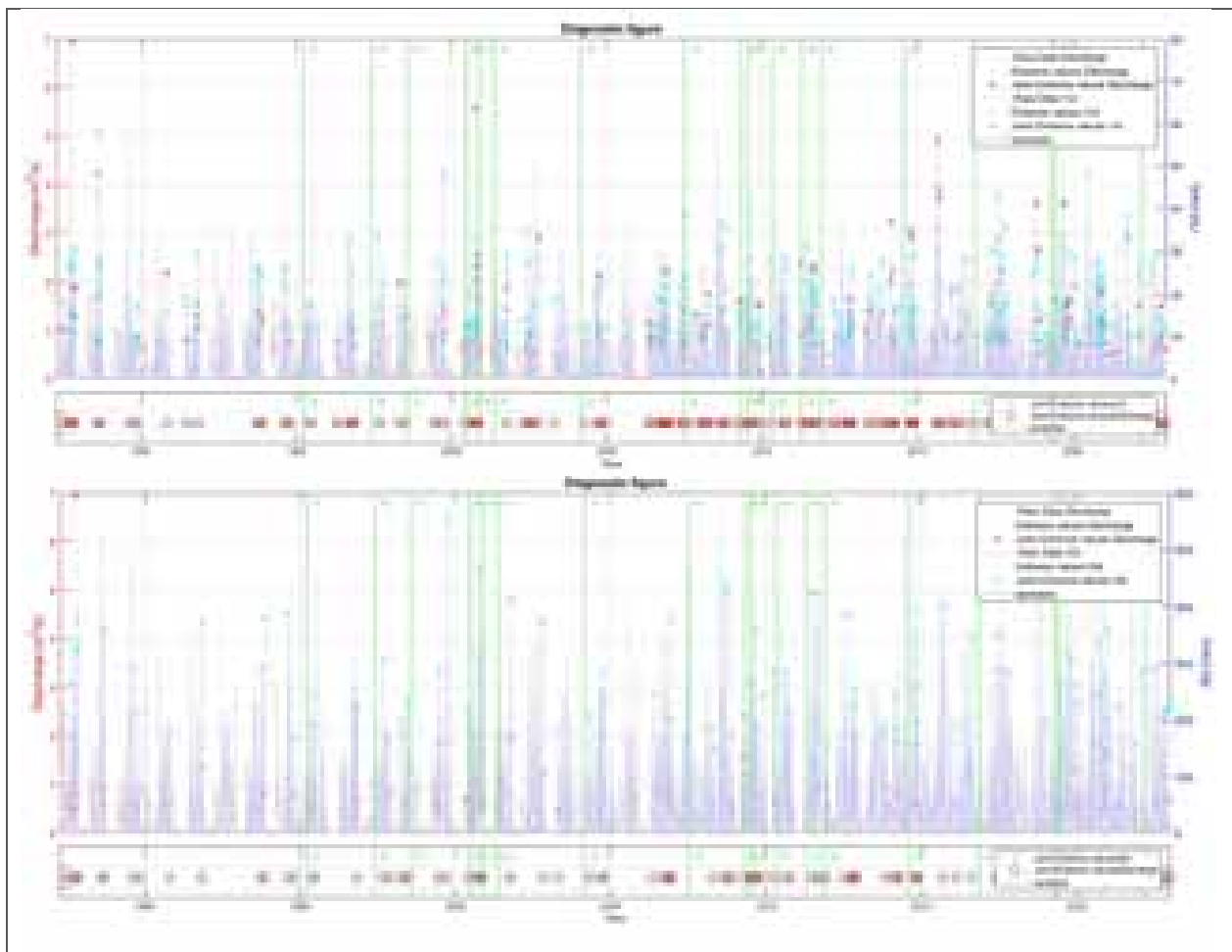
Figure A1.6 Diagnostic figures used to analyse landslide events against joint extreme events. Above 1-day rainfall duration and floods. Below 5-day rainfall duration and floods.
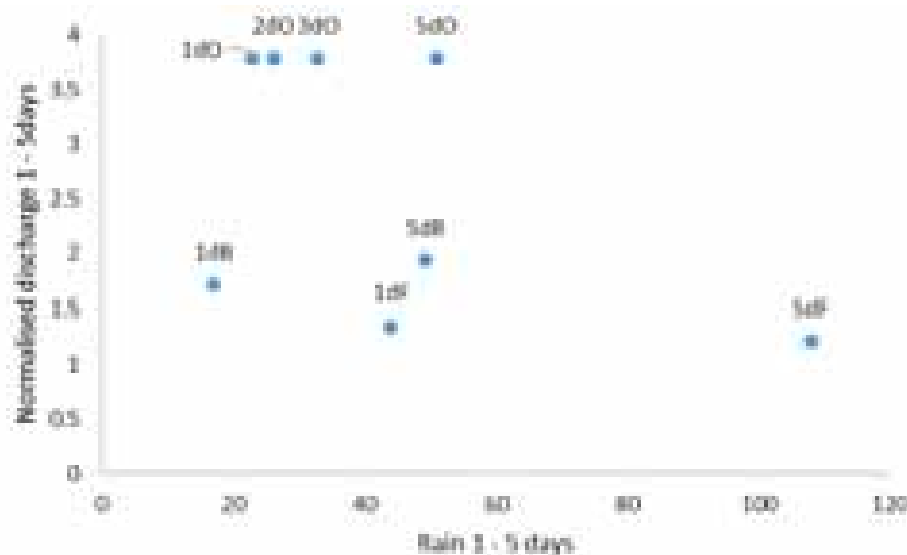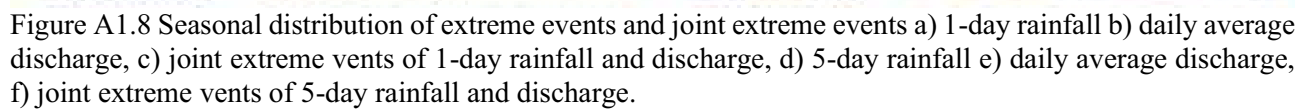

Figure A1.7 Precipitation extreme thresholds plotted against normalised extreme threshold for discharge from Gryta station and modelled data series. Labels on the points are 1-day to 5-days rain for O (observed, rain and discharge), B (observed rain and baseline for discharge) and (F) future pairs (projected rain and discharge).

*******************************   *******************************

Figure A1.8 Seasonal distribution of extreme events and joint extreme events a) 1-day rainfall b) daily average discharge, c) joint extreme vents of 1-day rainfall and discharge, d) 5-day rainfall e) daily average discharge, f) joint extreme vents of 5-day rainfall and discharge.

Figure A1.9 Diagnostic figures use to analyse landslide events against joint extreme events. Selected years with extreme summer rain, 1-day rainfall duration and floods.

A1.2 Sensitivity analysis to identify the higher Kendall's rank correlation coefficients for Oslo compound coastal and riverine flood events (baseline scenario). In red the selected combination of thresholds.

Scenario	Surge threshold (percentile)	Flow threshold (percentile)	Surge threshold (m)	Flow threshold (m3/s)	Surge-Flow τ	n° joint extreme events
Baseline	85	85	0.63	1.45	0.05	45
	85	90	0.63	1.59	0.16	32
	85	95	0.63	1.90	0.15	19
	85	97	0.63	2.09	0.10	13
	90	85	0.73	1.45	0.32	31
	90	**90**	**0.73**	**1.59**	**0.44**	**20**
	90	95	0.73	1.90	0.13	11
	90	97	0.73	2.09	0.07	8
	95	85	0.87	1.45	0.08	18
	95	90	0.87	1.59	0.21	13
	95	95	0.87	1.90	0.02	10
	95	97	0.87	2.09	0.07	8
	97	85	0.98	1.45	0.38	11
	97	90	0.98	1.59	0.14	7
	97	95	0.98	1.90	-0.20	2
	97	97	0.98	2.09	0.20	5

****************************** ******************************

A1.3 Sensitivity analysis to identify the higher Kendall's rank correlation coefficients for Oslo compound coastal and riverine flood events (future scenario). In red the selected combination of thresholds.

Scenario	Surge threshold (percentile)	Flow threshold (percentile)	Surge threshold (m)	Flow threshold (m3/s)	Surge-Flow τ	n° joint extreme events
Future	85	85	0.56	1.84	-0.21	52
	85	90	0.56	1.95	-0.15	41
	85	95	0.56	2.17	0.11	19
	85	97	0.56	2.36	0.18	12
	90	85	0.67	1.84	-0.03	37
	90	**90**	**0.67**	**1.95**	**0.02**	**27**
	90	95	0.67	2.17	0.07	10
	90	97	0.67	2.36	0.14	7
	95	85	0.81	1.84	0.09	19
	95	90	0.81	1.95	0.00	12
	95	95	0.81	2.17	-0.80	5
	95	97	0.81	2.36	-1.00	4
	97	85	0.86	1.84	-0.14	8
	97	90	0.86	1.95	-0.20	6

8.2   Appendix A2: Nice
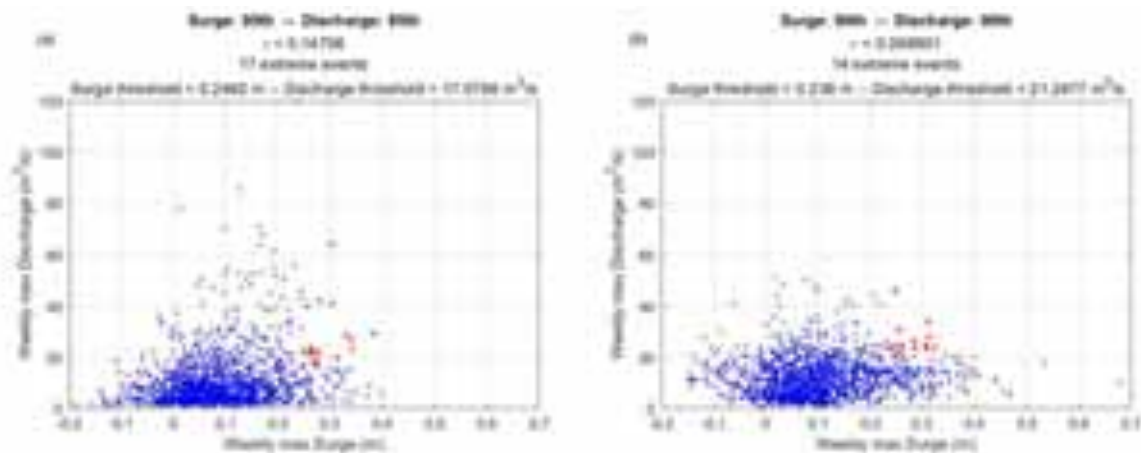
Figure A2.1. Compound flood events in Nice. Scatter plot of all pairs of weekly sea surge level and river flow (blue) and pairs of extreme compound events (red). (a) Baseline scenario; (b) Future climate change scenario.
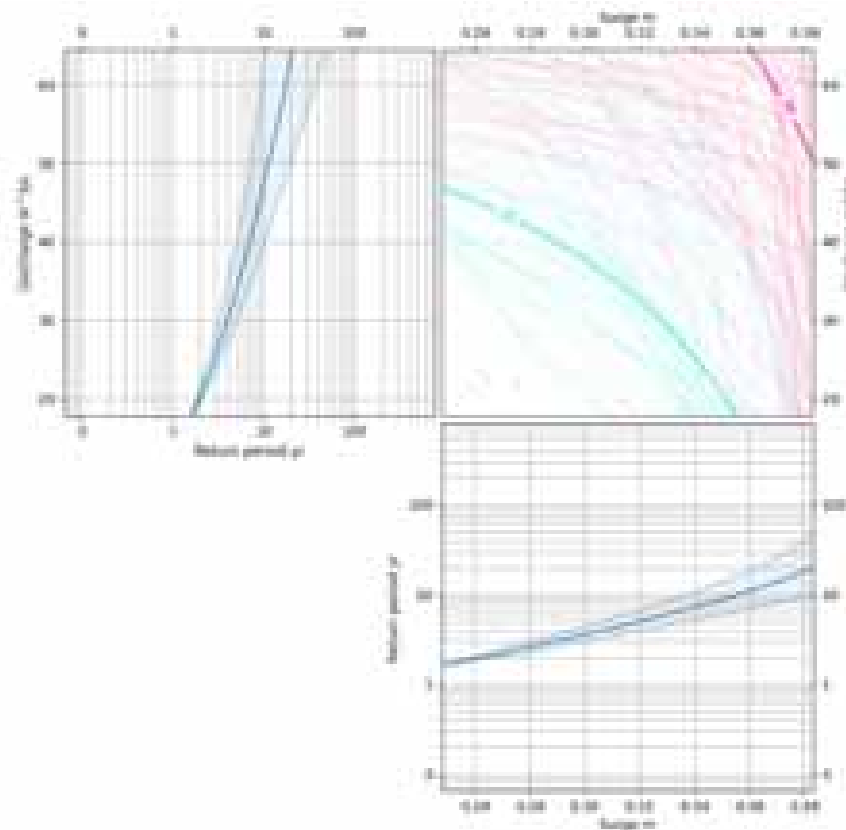
Figure A2.2. Nice compound coastal and riverine flood events at the baseline (1979-2005) scenario. The figure indicates marginal distribution based on generalized Pareto distribution (GPD) for extreme river flows (upper left), extreme surge (lower right); joint return period of extreme paired data based on the selected copula (upper right).

*****************************   *****************************
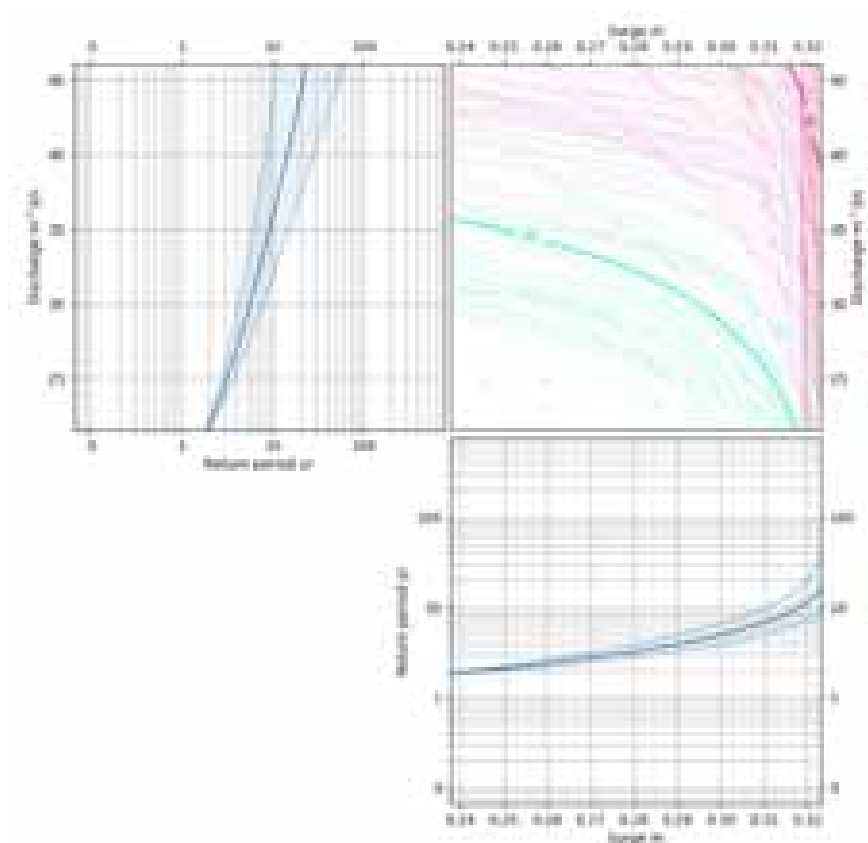
Figure A2.3. Nice compound coastal and riverine flood events at the future (2016-2050) scenario. The figure indicates marginal distribution based on generalized Pareto distribution (GPD) for extreme river flows (upper left), extreme surge (lower right); joint return period of extreme paired data based on the selected copula (upper right).
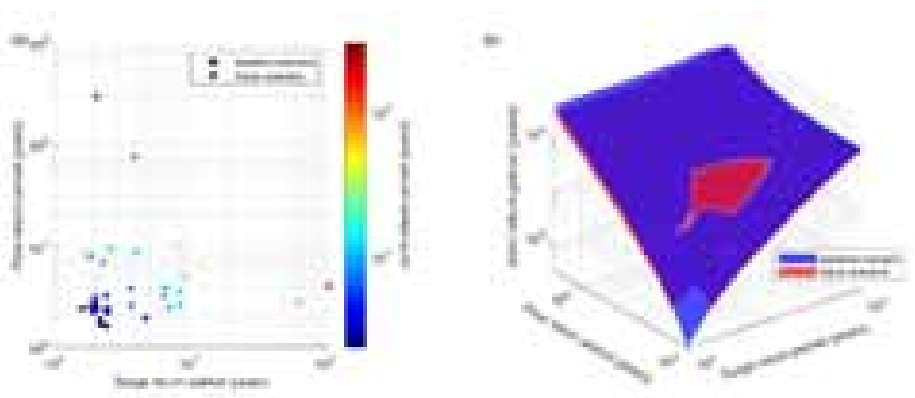
Figure A2.4. Nice compound coastal and riverine flood events. Comparison of JRPs between baseline and future climate change conditions.

8.3   Appendix A3: Essex
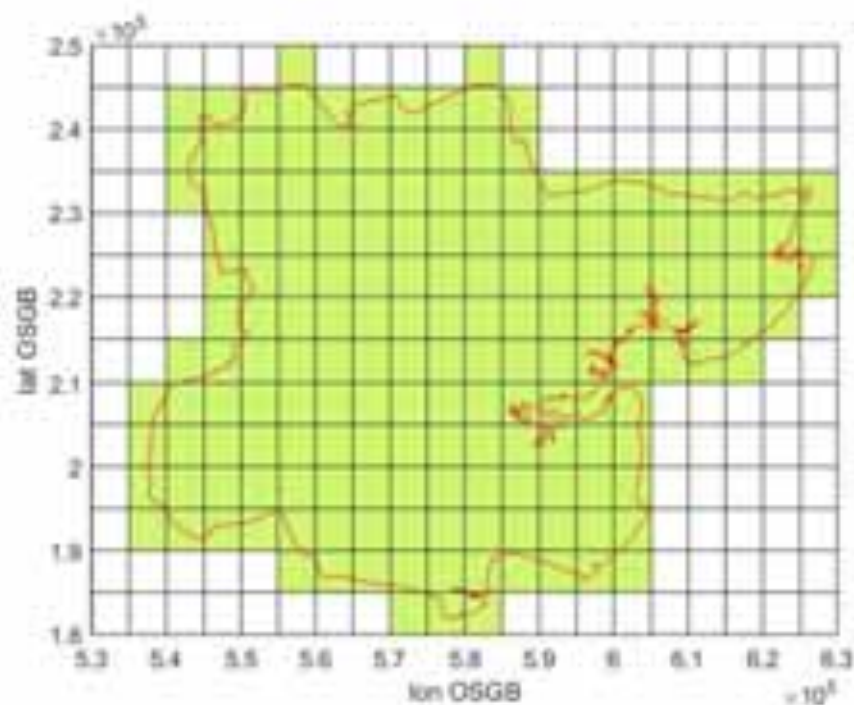
Figure A3.1. Overlapping of the 5 km grid of the UK Climate Projection 2018 datasets with Essex County boundary. The cells highlighted in green has been used for the analysis.

A3.1. Sensitivity analysis to identify the higher Kendall's rank correlation coefficients for Essex wind and rainfall events (baseline scenario). In red the selected combination of thresholds.

Scenario	Wind gust speed threshold (percentile)	Rainfall threshold (percentile)	Wind gust speed threshold (ms-1)	Rainfall threshold (mm)	Wind gust speed-rainfall τ	n° joint extreme events
Baseline	85	85	14.08	11.57	-0.40	302
	85	90	14.08	15.56	-0.03	184
	85	95	14.08	22.63	-0.05	76
	85	97	14.08	29.69	-0.05	40
	90	85	15.12	11.57	0.02	223
	90	90	15.12	15.56	0.08	132
	90	95	15.12	22.63	-0.03	49
	90	97	15.12	29.69	-0.08	24
	95	85	16.62	11.57	0.07	120
	95	90	16.62	15.56	0.13	71
	95	95	16.62	22.63	0.14	29
	95	97	16.62	29.69	-0.10	13
	97	85	17.74	11.57	0.12	76
	97	**90**	**17.74**	**15.56**	**0.19**	**46**
	97	95	17.74	22.63	0.11	20
	97	97	17.74	29.69	-0.42	10

A3.2 Sensitivity analysis to identify the higher Kendall's rank correlation coefficients for Essex wind and rainfall events (future scenario). In red the selected combination of thresholds.

Scenario	Wind gust speed threshold (percentile)	Rainfall threshold (percentile)	Wind gust speed threshold (ms^{-1})	Rainfall threshold (mm)	Wind gust speed-rainfall τ	n° joint extreme events
Future	85	85	14.08	11.46	-0.02	370
	85	90	14.08	15.73	-0.09	229
	85	95	14.08	24.56	-0.05	100
	85	97	14.08	31.06	-0.01	51
	90	85	15.23	11.46	0.04	280
	90	90	15.23	15.73	-0.07	170
	90	95	15.23	24.56	-0.08	68
	90	97	15.23	31.06	-0.22	33
	95	85	16.94	11.46	0.06	170
	95	90	16.94	15.73	-0.03	108
	95	95	16.94	24.56	-0.12	38
	95	97	16.94	31.06	0.01	19
	97	**85**	**18.07**	**11.46**	**0.09**	**115**
	97	90	18.07	15.73	-0.02	75
	97	95	18.07	24.56	0.02	23
	97	97	18.07	31.06	-0.56	9

****************************   *****************************
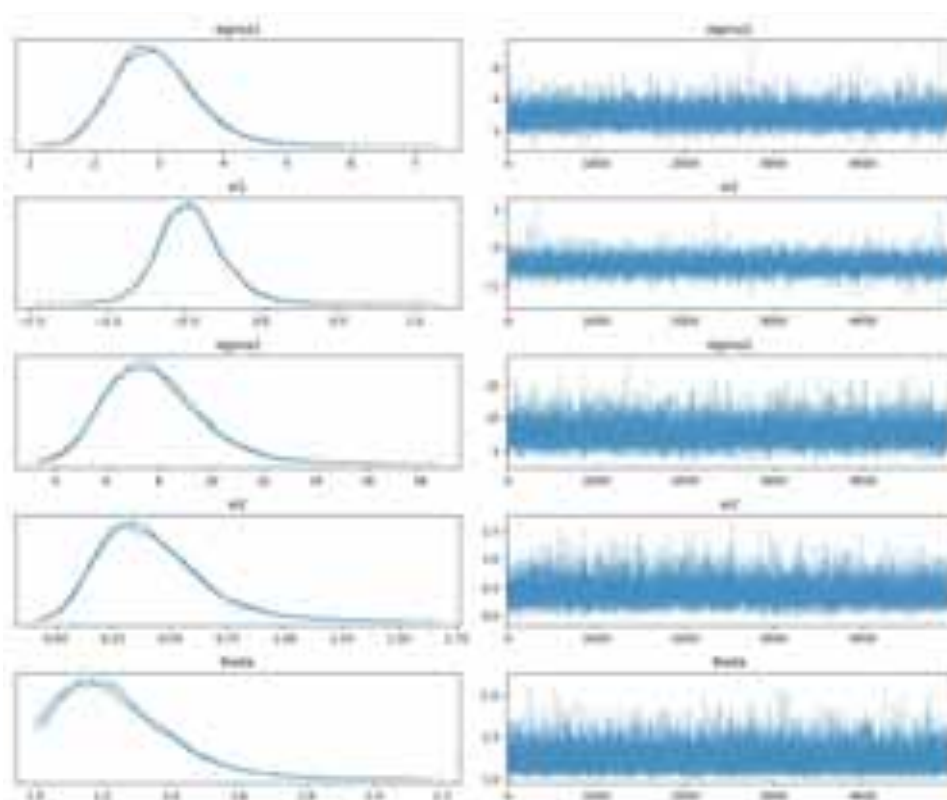
Figure A3.2. Trace plot for the five parameters of the joint distribution function used to analyse joint extreme wind and rainfall in Essex at baseline conditions. Here, xi1 and xi2 are the Generalised Pareto Distribution (GPD) shape parameters, and sigma1 and sigma2 are the GPD scale parameters for daily maximum wind gust speed and daily precipitation, respectively. 'Theta' is the Gumbel copula parameter.
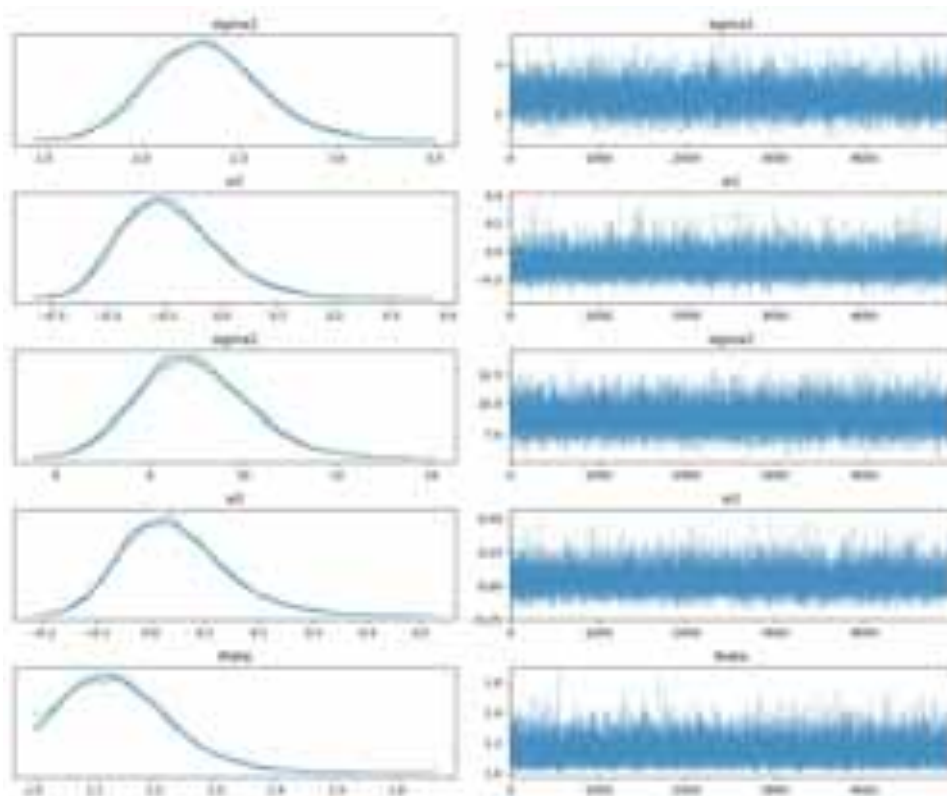
Figure A3.3. Trace plot for the five parameters of the joint distribution function used to analyse joint extreme wind and rainfall in Essex at future scenario. Here, x_{i1} and x_{i2} are the Generalised Pareto Distribution (GPD) shape parameters, and sigma1 and sigma2 are the GPD scale parameters for daily maximum wind gust speed and daily precipitation, respectively. 'Theta' is the Gumbel copula parameter.
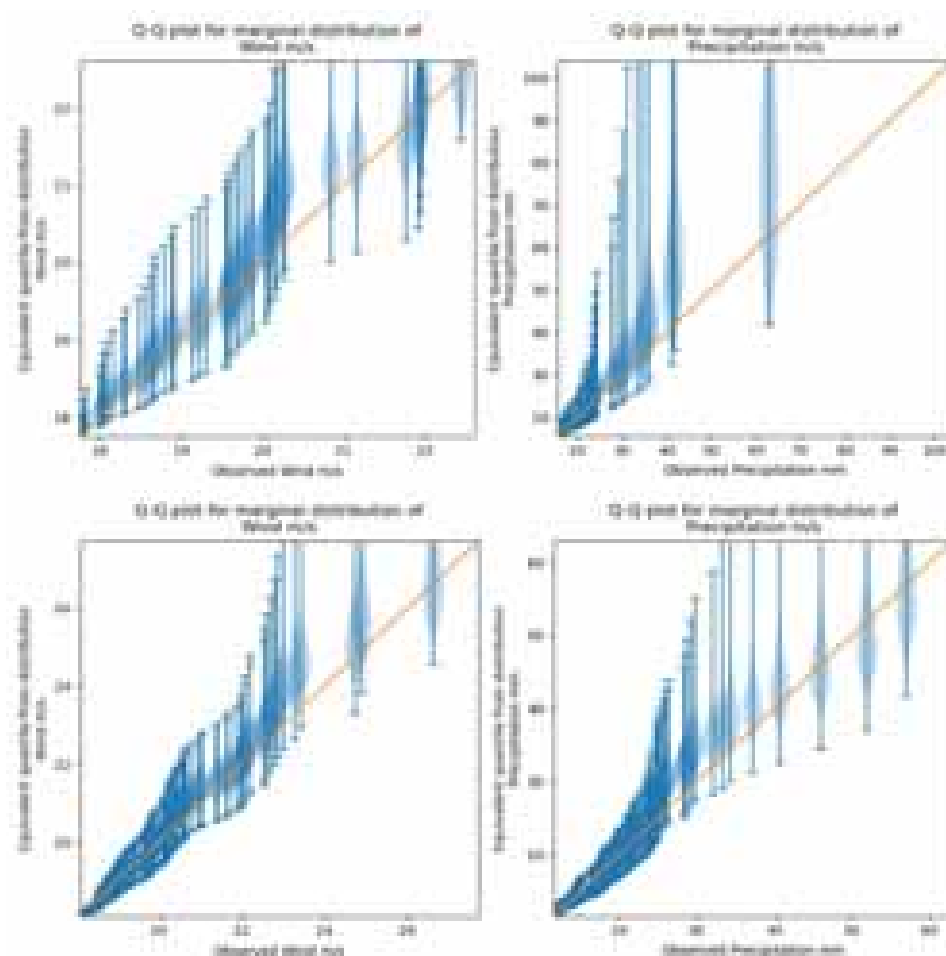
Figure A3.4. Model assessment results for analysing Essex joint extreme wind and rainfall events. Bayesian Quantile-Quantile plots for the two (gust speed and precipitation) marginal GPD, at baseline (upper) and future (lower) scenarios.

(a)
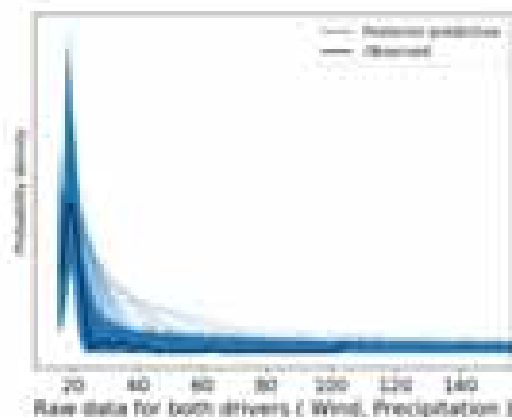
(b)
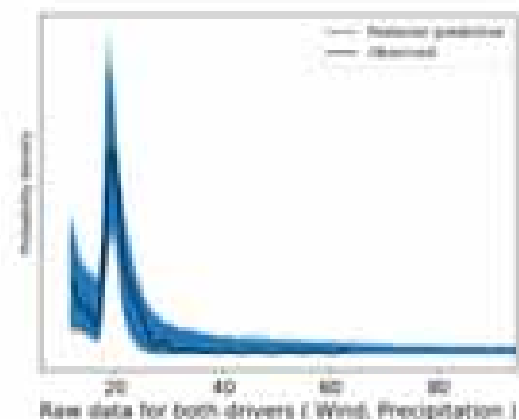
Figure A3.5. Model assessment results for analysing Essex joint extreme wind and rainfall events. Posterior predictive checks at baseline (a) and future (b) scenarios

(a)
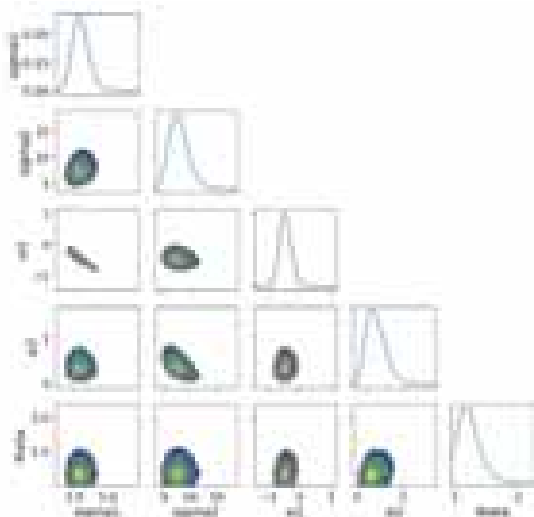
(b)
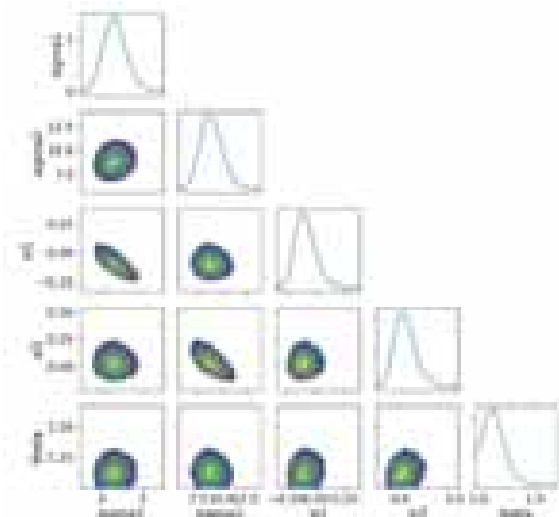
Figure A3.6. Model assessment results for analysing Essex joint extreme wind and rainfall events. Corner plots for baseline (a) and future (b) scenarios.

*****************************   *****************************
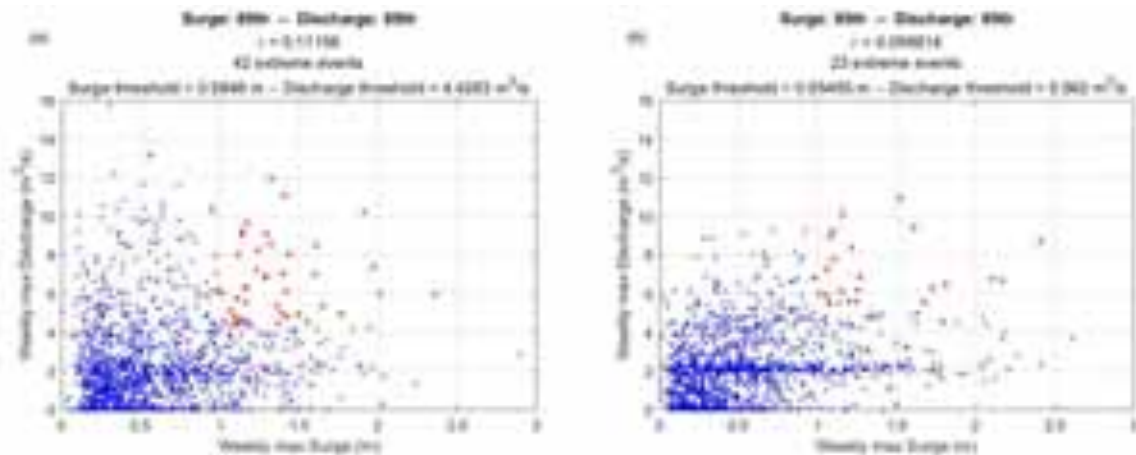
Figure A3.7. Compound flood events in Essex. Scatter plot of all pairs of weekly sea surge level and river flow (blue) and pairs of extreme compound events (red). (a) Baseline scenario; (b) Future climate change scenario.
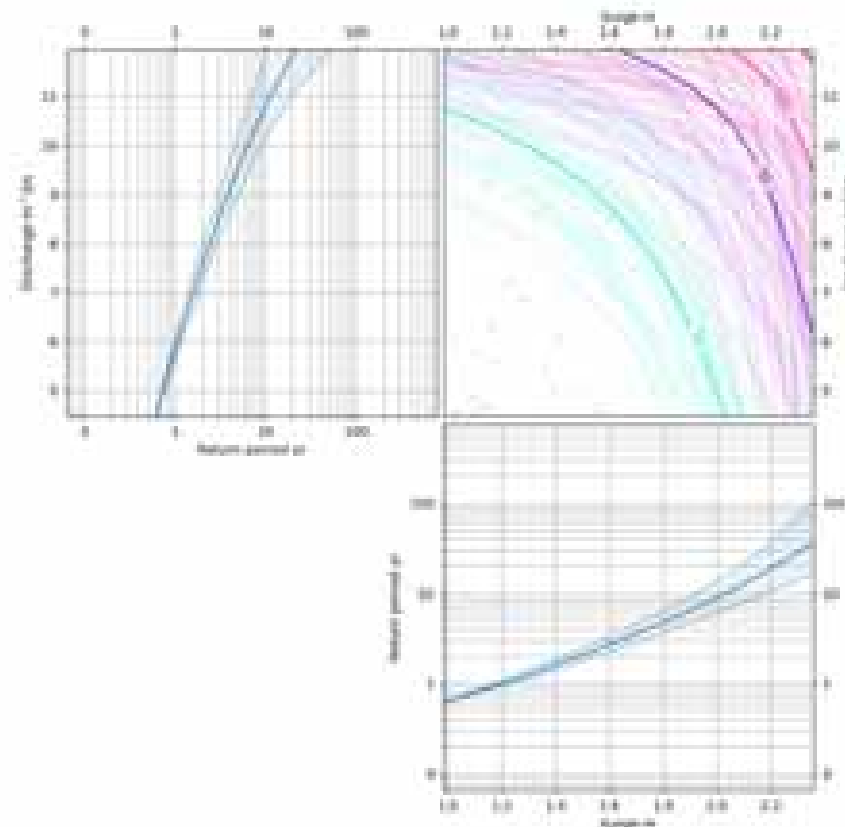
Figure A3.8. Essex compound coastal and riverine flood events at the baseline (1979-2005) scenario. The figure indicates marginal distribution based on generalized Pareto distribution (GPD) for extreme river flows (upper left), extreme surge (lower right); joint return period of extreme paired data based on the selected copula (upper right).
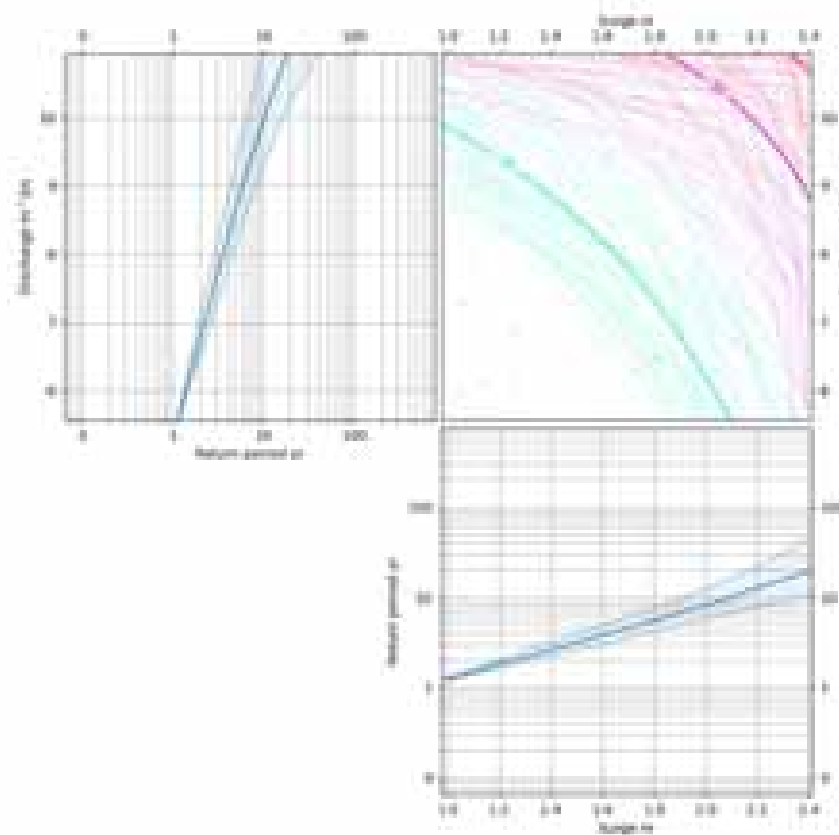
Figure A3.9. Essex compound coastal and riverine flood events at the future (2016-2050) scenario. The figure indicates marginal distribution based on generalized Pareto distribution (GPD) for extreme river flows (upper left), extreme surge (lower right); joint return period of extreme paired data based on the selected copula (upper right).
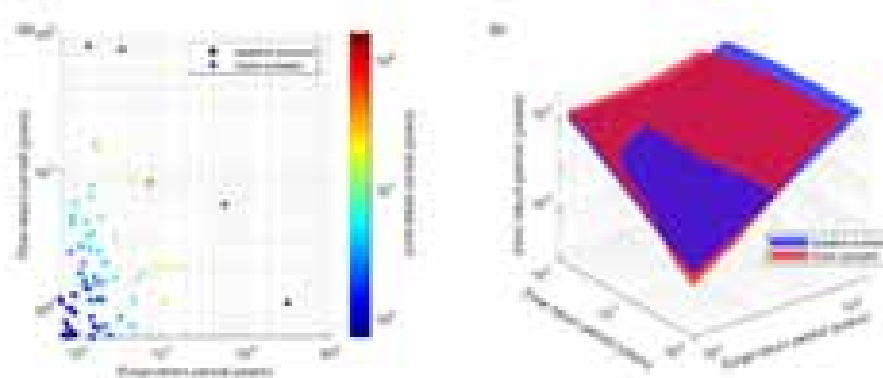
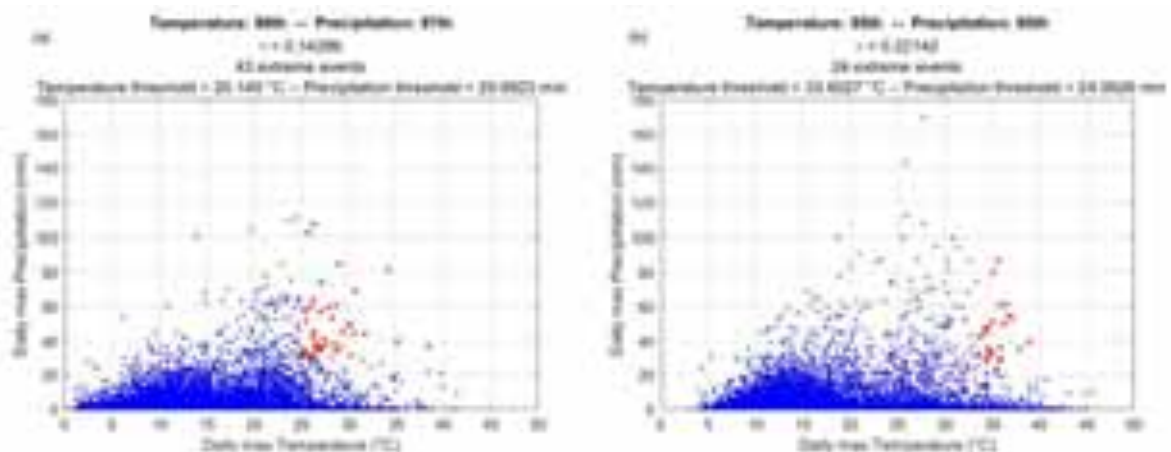Figure A3.10. Essex compound coastal and riverine flood events. Comparison of JRPs between baseline and future climate change conditions.

Figure A3.11. Joint extreme temperature and precipitation events in Essex. Scatter plot of all pairs of daily maximum temperature and daily precipitation (blue) and pairs of joint extreme events (red). (a) Baseline condition; (b) Future climate change scenario.
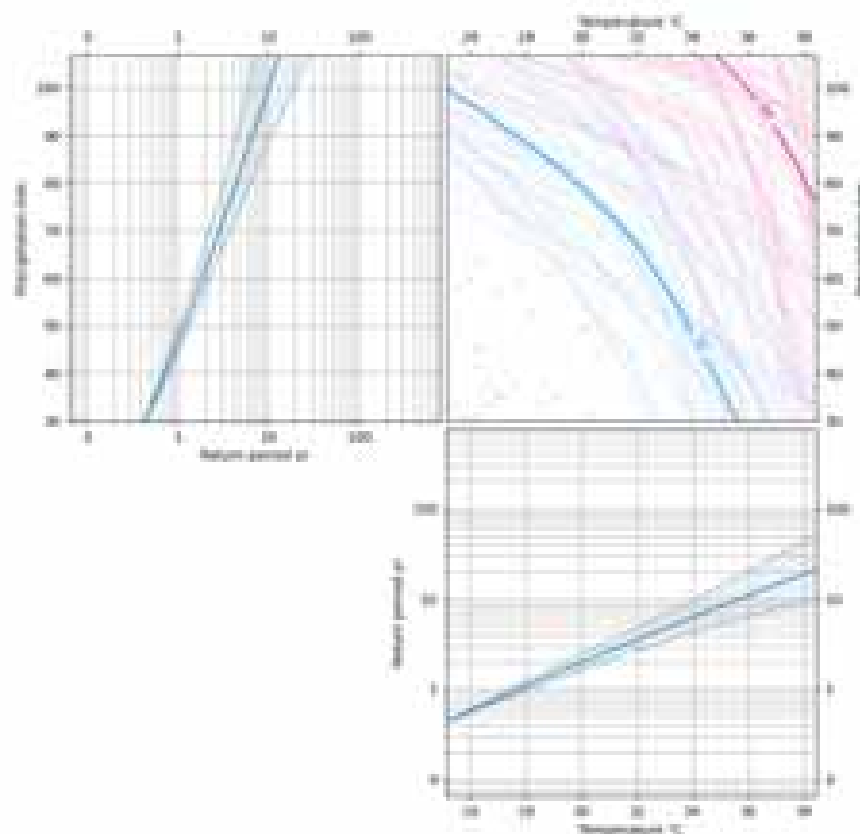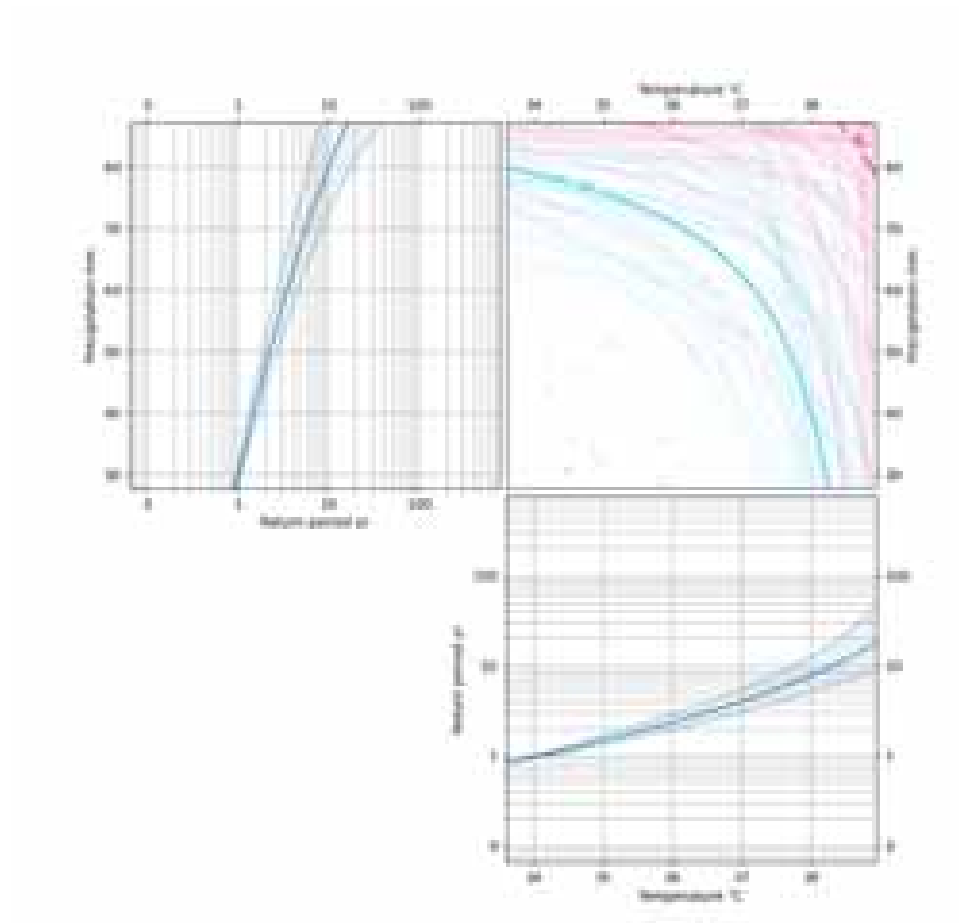

Figure A3.12. Essex joint extreme temperature and precipitation events at the baseline (1981-2000) scenario. The figure indicates marginal distribution based on generalized Pareto distribution (GPD) for extreme precipitation (upper left), extreme temperature (lower right); joint return period of extreme paired data based on the selected copula (upper right).
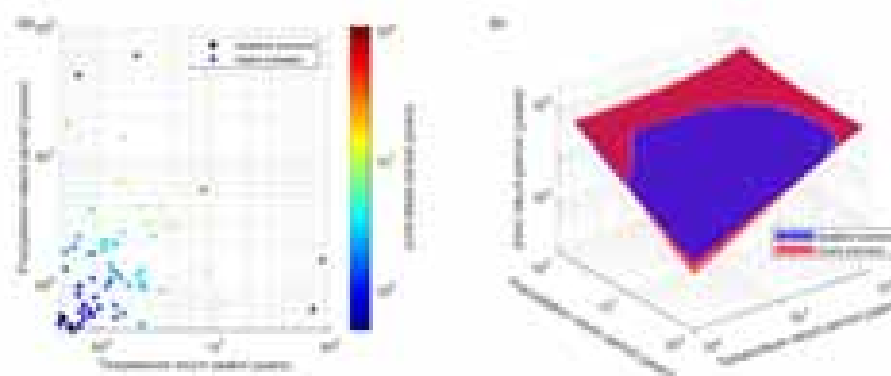
Figure A3.13. Essex joint extreme temperature and precipitation events at the future (2061-2080) scenario. The figure indicates marginal distribution based on generalized Pareto distribution (GPD) for extreme precipitation (upper left), extreme temperature (lower right); joint return period of extreme paired data based on the selected copula (upper right).

Figure A3.14. Essex extreme temperature and precipitation events. Comparison of JRPs between baseline and future climate change conditions.

8.4 Appendix A4: Múlaþing

Table A4.1 Landslide events and weather. Yellow text highlights landslides without heavy rain, brown text highlights landslides occurring during extreme rain without high API

date	R	T	TX	Land-slide events	Rain-length hours	3h	12h	24h	48h	72h	120h
25.9.1981	1.07	6.3	6.9	3	65	3.7	27.2	66.7	68.9	68.9	68.9
4.10.1985	1.4	5.4	7.7	1	16	1.9	1.9	1.9	1.9	1.9	1.9
12.8.1989	6.22	8.2	8.6	6	32	17.4	59.1	100.5	114.0	137.2	142.3
27.8.1994	4.94	8.4	9.4	1	32	14.6	63.2	101.1	101.1	101.1	101.1
9.9.1999	2.04	9.8	11.8	2	19	4.7	31.9	44.8	46.8	46.8	46.8
1.10.2001	2.69	7.8	8.5	1	81	8.5	30.3	53.9	86.6	86.6	86.6
2.10.2001	5.61	6.5	7.8	11	81	18.7	84.9	144.0	197.9	230.6	230.6
17.6.2002	0.82	6.7	8.1	1	56	1.3	1.3	1.3	1.3	1.3	1.3
11.10.2002	2.23	7.7	8.8	1	53	6.6	11.1	16.2	26.6	44.9	52.8
11.11.2002	4.4	5.3	5.7	3	62	8.4	18.9	20.2	20.2	20.2	20.2
23.11.2002	2.92	5.3	5.8	1	61	8.5	16.7	17.3	44.0	101.0	151.1
24.11.2002	2.22	5.3	6.1	1	61	5.9	17.6	31.0	48.2	74.9	178.0
25.11.2002	2.36	5.7	6.4	1	61	6.6	12.4	32.2	63.1	80.4	164.1
21.8.2003	1.77	10.9	11.3	1	14	4.6	5.8	5.8	5.8	5.8	5.8
24.8.2009	4.66	9.7	10.1	2	13	9.7	10.5	10.5	10.5	10.5	10.5
7.7.2010	2.91	8	9.4	1	17	5.5	6.9	6.9	6.9	6.9	6.9
28.5.2013	2.49	5.3	8.6	2	37	8.8	44.2	96.2	104.8	104.8	104.8
28.12.2015	4.64	7	8	5	29	12.2	23.6	23.6	23.6	23.6	23.6
24.6.2017	2.68	6.4	7.2	4	38	9.5	65.7	126.8	131.3	142.4	142.4

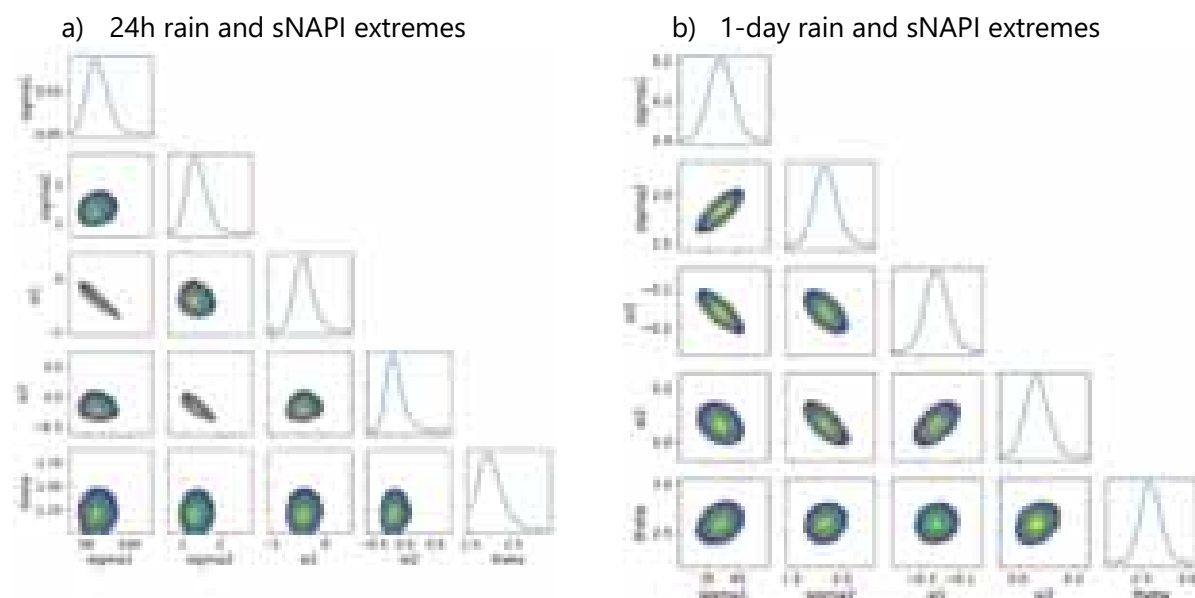a) 24h rain and sNAPI extremes   b) 1-day rain and sNAPI extremes

Figure A.4.1 Model assessment results for analysing Múlaþing joint extreme rainfall and sNAPI events. Corner plots for historical (a) and future (b) scenarios.
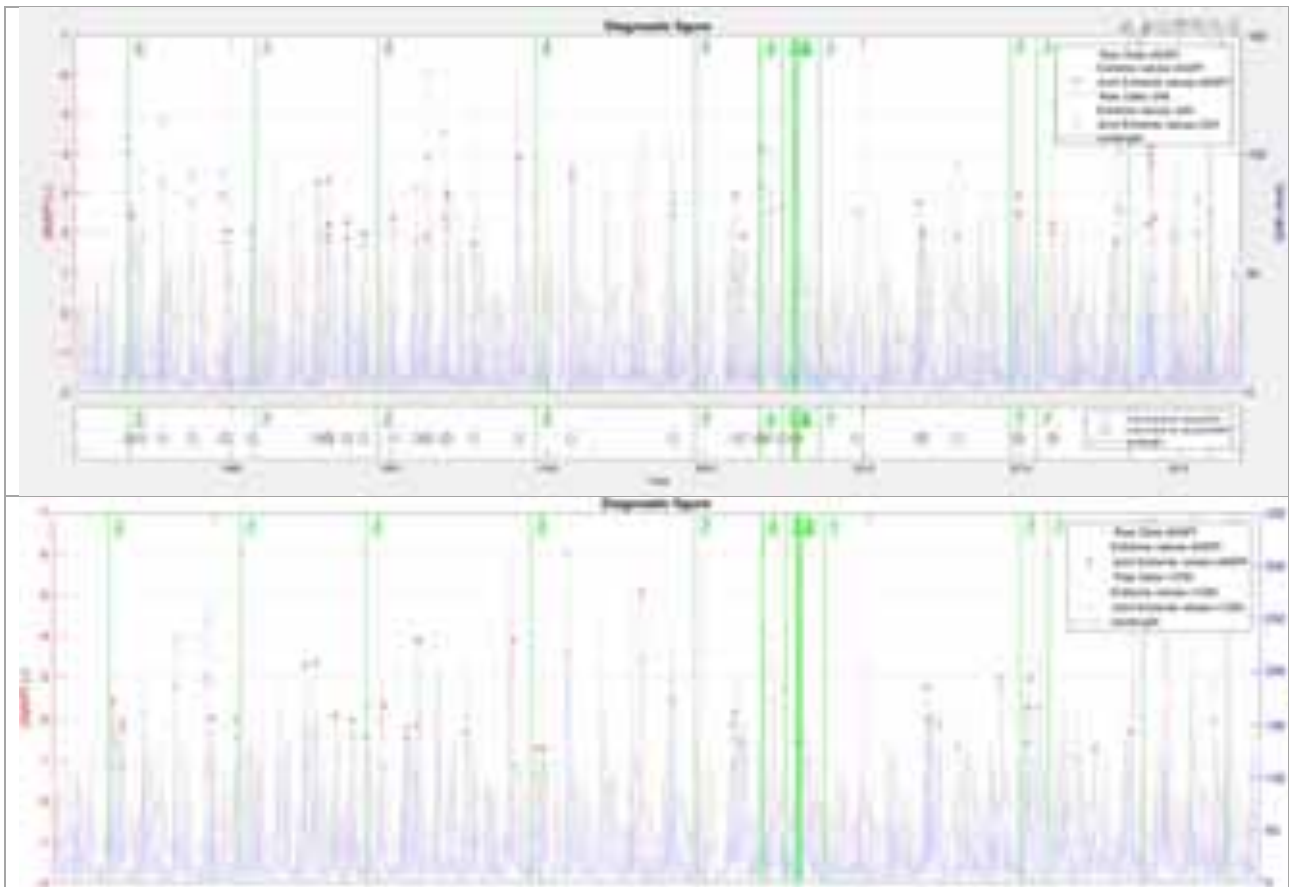
Figure A4.2 Diagnostic figures used to analyse landslide events against joint extreme events. Above 1-day rainfall duration and floods. Below 5-day rainfall duration and floods.
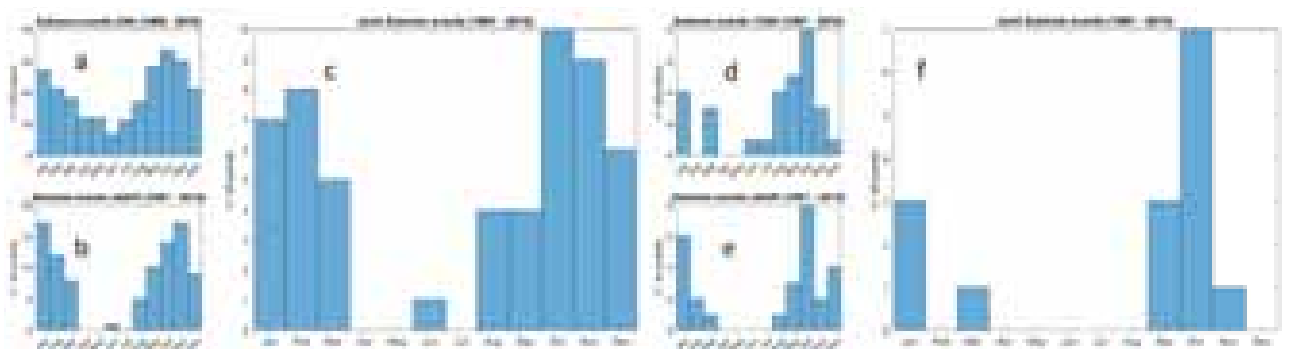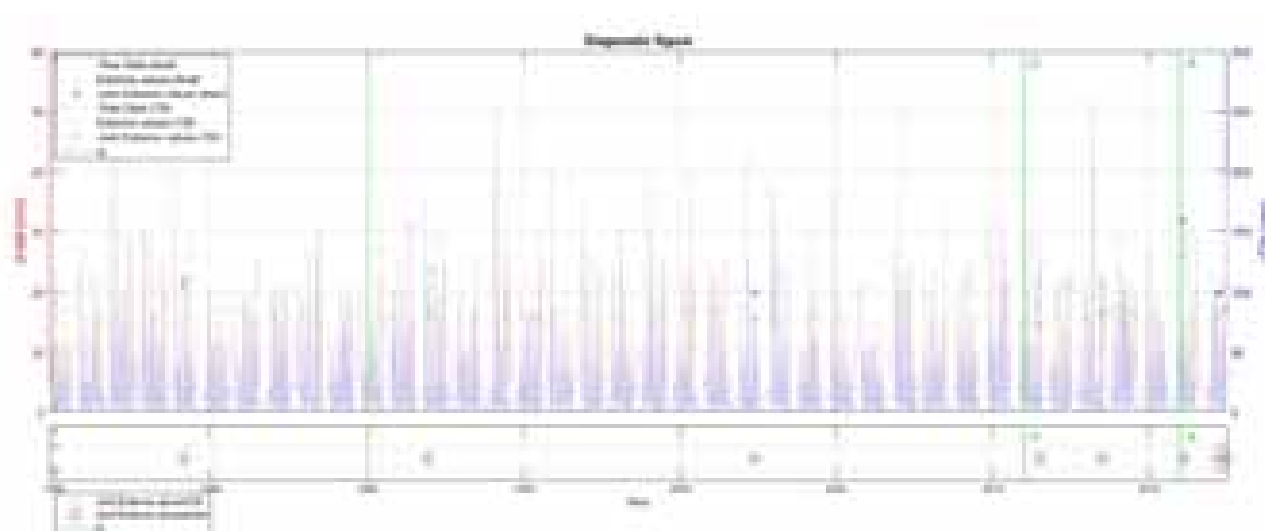

Figure A4.3 Seasonal distribution of extreme events and joint extreme events a) 1-day rainfall b) sNAPI, c) joint extreme vents of 1-day rainfall and sNAPI, d) 5-day rainfall e) sNAPI, f) joint extreme vents of 5-day rainfall and sNAPI.

Figure A4.3 Diagnostic figures used to analyse landslide events against joint extreme events. 1-day rainfall duration and snowmelt.
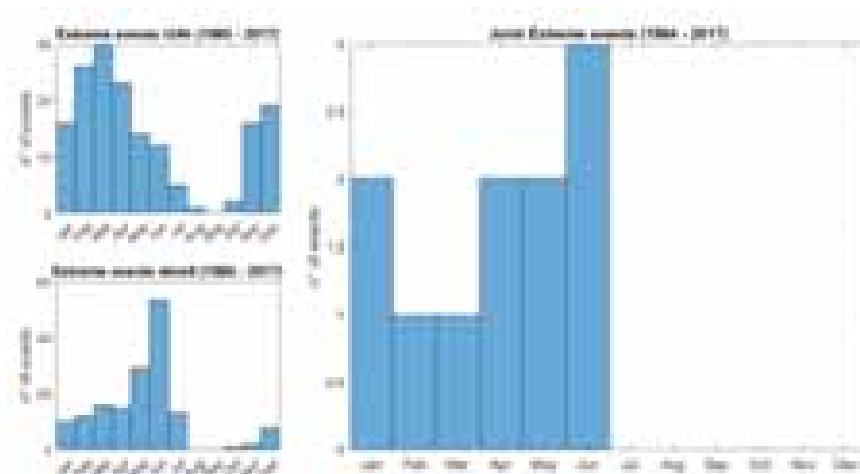

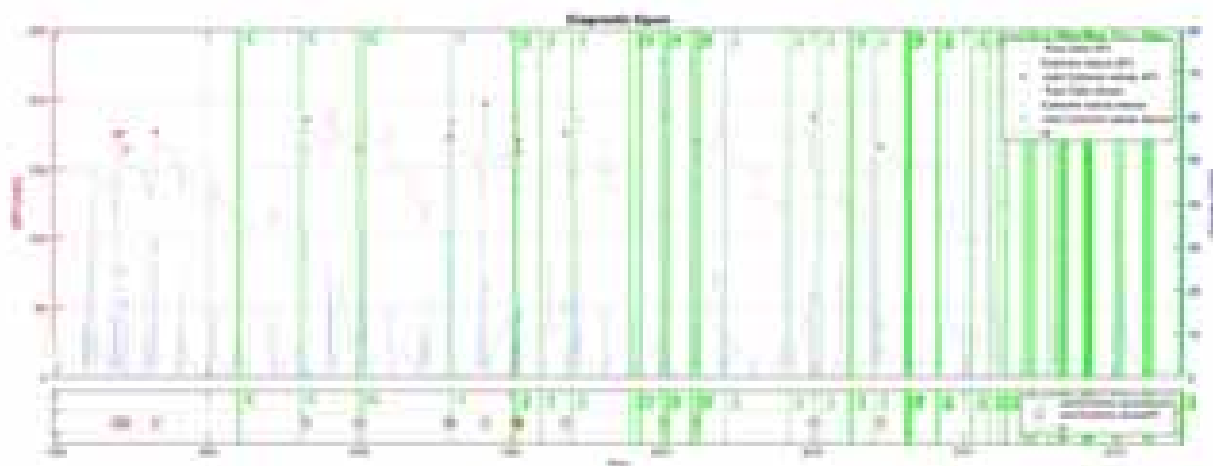Figure A4.4 Seasonal distribution of extreme rainfall and snowmelt

*******************************   *******************************

Figure A5. Diagnostic figures use to analyse landslide events against joint extreme events. 1-day rainfall duration and snowmelt.
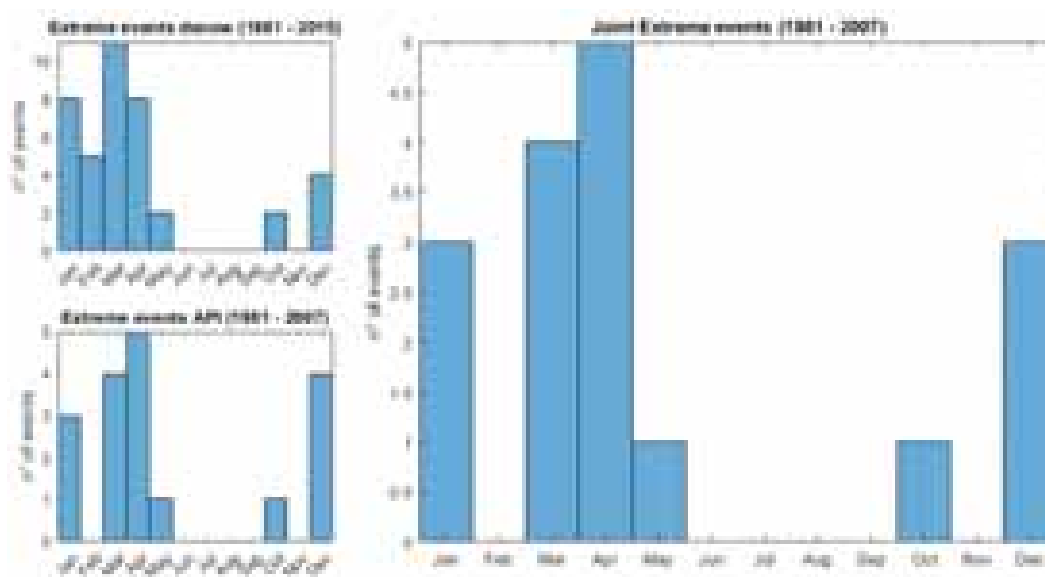

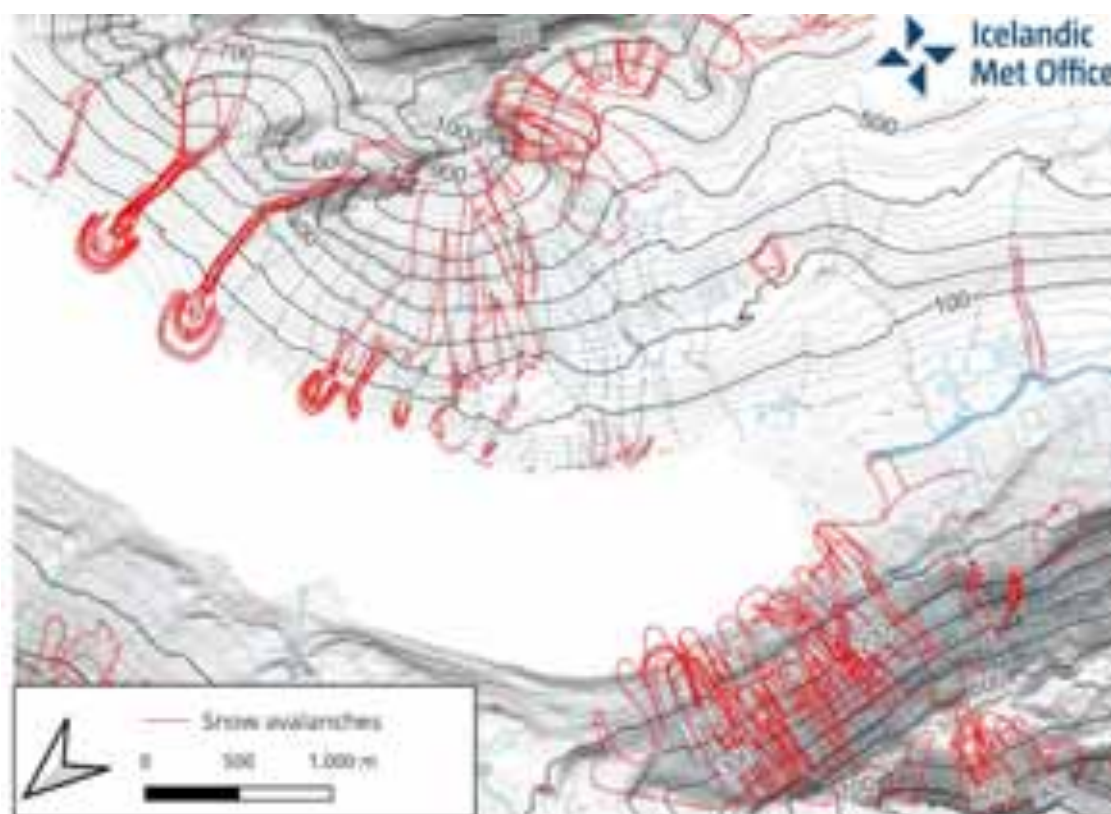Figure A4.6 Seasonal distribution of extreme rainfall and snowmelt

Figure A4.7 Map showing snow avalanche outlines in Seyðisfjörður.